Measurements of phase changes in crystals using Ptychographic X-ray imaging

Maria Civita

October 2016

Declaration

I, Maria Civita, confirm that the work presented in this Thesis is my own. Where information has been derived from other sources, I confirm that this has been indicated in the Thesis.

Abstract

In a typical X-ray diffraction experiment we are only able to directly retrieve part of the information which characterizes the propagating wave transmitted through the sample: while its intensity can be recorded with the use of appropriate detectors, the phase is lost. Because the phase term which is accumulated when an X-ray beam is transmitted through a slab of material is due to refraction [1, 2], and hence it contains relevant information about the structure of the sample, finding a solution to the "phase problem" has been a central theme over the years. Many authors successfully developed a number of techniques which were able to solve the problem in the past [3, 4, 5, 6], but the interest around this subject also continues nowadays [7, 8]. With this Thesis work, we aim to give a valid contribution to the phase problem solution by illustrating the first application of the ptychographic imaging technique [9, 10, 11, 12, 13, 14] to measure the effect of Bragg diffraction on the transmitted phase, collected in the forward direction. In particular, we will discuss the experimental methodology which allowed to detect the small phase variations in the transmitted wave when changing the X-ray's incidence angle around the Bragg condition. Furthermore, we will provide an overview of the theoretical frameworks which can allow to interpret the experimental results obtained. More specifically, we will also discuss a new *quasi-kinematic* approximation which was recently developed by Gorobtsov and Vartanyants [2] in order to highlight the potential for future applications of the methodology described in this work. In particular, this new theory, used in conjunction with the experimental technique here presented, will permit to investigate further the effects related to the phase of the transmitted beam, thus allowing to study the structure of strained crystals as well as to fully determine the phase of the structure factor.

Contents

Chapter 1

The phase problem

In 1912 Friedrich, Knipping and von Laue [15] gave evidence for both the wave nature of X-rays and the space lattice of crystals, when performing an experiment in which they used an X-ray beam to illuminate a crystalline sample. By placing a photographic plate downstream from the sample, as shown in Fig. 1.1, they were able to record the diffraction pattern resulting from the experiment and to understand that positions and intensities of the imprinted dark spots were related to the inner structure of the crystal. While giving evidence to the phenomenon of X-rays diffraction, this experiment also showed an important limit: the amplitude of the diffraction pattern was easily accessible through the experiment, but the phase information was completely lost. The main consequence related with the loss of the phase information was that measured intensities alone could not lead to a unique crystal structure [16], hence the phase problem started to be a central theme in X-ray crystallography.

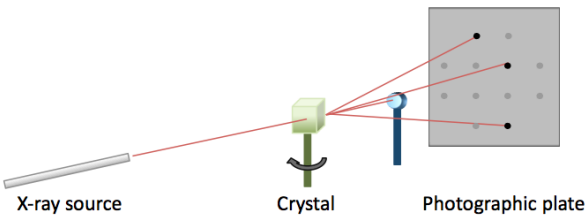

Figure 1.1: Experimental setup of Friedrich, Knipping and von Laue in 1912 as described in [16].

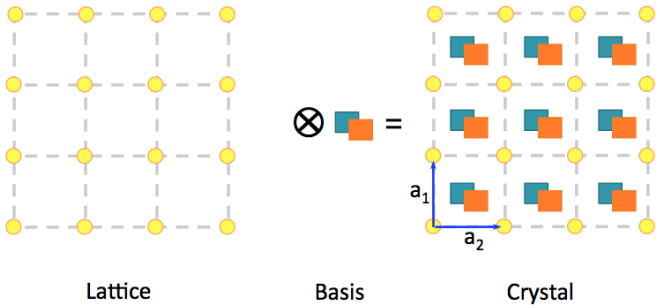

Figure 1.2: Construction of a 2D crystal structure from the convolution of a lattice and a basis as described in [1]. In this sketch we show how a crystal can be described as a regular repetition in space of a basic structural motif, which is defined as the crystal unit cell. In this figure the unit cell is described by the basis and is identified by vectors **a**1 and **a**2.

1.1 Theoretical background

In order to give more clarity around the phase problem formulation it is necessary to introduce the physical quantities involved in an X-ray scattering experiment. A more detailed description of the theoretical framework required to fully comprehend the different aspects involved in the solution of the phase problem will be provided in the following Chapters, however here we aim to present a brief qualitative introduction to this subject.

The structure of a crystal can be described as a regular repetition of basic elements in the three spatial dimensions. In this view, a crystalline structure is defined by specifying the lattice and by associating a basis, composed by either atoms or molecules, to each point in the lattice, as shown in Fig. 1.2 [1]. In a three-dimensional space the lattice is specified by a set of vectors as

$$\mathbf{R} = n_1\mathbf{a}_1 + n_2\mathbf{a}_2 + n_3\mathbf{a}_3 \tag{1.1}$$

where vectors **a**1, **a**2, **a**3 define the unit cell and n_1, n_2, n_3 are integers. In the real space, the lattice is usually defined as direct, while its Fourier transform takes the name of reciprocal lattice. The function associated to the basis, which describes the atomic structure contained in each unit cell, is the electron density $\rho(\mathbf{R})$. This quantity is a periodic function of $\mathbf{R}$ and can be represented with a triple Fourier series

$$\rho(\mathbf{R}) = \frac{\mathbf{1}}{\mathbf{V}} \sum_{\mathbf{H}} F_{\mathbf{H}} e^{(-2\pi i \mathbf{H}\cdot\mathbf{R})} \tag{1.2}$$

where V is the volume of the unit cell and $\mathbf{H}$ represents the reciprocal lattice vector [16]. The Fourier coefficient $F_{\mathbf{H}}$ represents the structure factor correspondent to the reciprocal lattice vector $\mathbf{H}$ and can be obtained by integration over the unit cell volume as

$$F_{\mathbf{H}} = \int_V \rho(\mathbf{R}) e^{(2\pi i \mathbf{H}\cdot\mathbf{R})} dV. \tag{1.3}$$

In its polar form the structure factor can be written as

$$F_{\mathbf{H}} = |\mathbf{F_H}| e^{i\beta_{\mathbf{H}}} \tag{1.4}$$

where $|F_{\mathbf{H}}|$ is its amplitude and $\beta_{\mathbf{H}}$ represents its phase. By substituting Eq. 1.4 into Eq. 1.2 we can obtain the electron density function in the form

$$\rho(\mathbf{R}) = \frac{\mathbf{1}}{\mathbf{V}} \sum_{\mathbf{H}} |F_{\mathbf{H}}| \, e^{(i\beta_{\mathbf{H}} - 2\pi i \mathbf{H}\cdot\mathbf{R})} \tag{1.5}$$

which highlights how clear knowledge of both amplitude and phase of the structure factor are necessary in order to fully determine $\rho(\mathbf{R})$.

As stated at the beginning of this Chapter, the intensities $|F_{\mathbf{H}}|$ are directly determined during a scattering experiment, in fact they correspond to the maxima of the diffraction pattern collected in the far field, downstream from the sample. We can so conclude that by knowing both the phase and the amplitude of the structure factor we can determine the electron density $\rho(\mathbf{R})$ which, used in Eq. 1.3, allows to completely determine the nature of the diffraction pattern and consequently the structure of the crystal [16]. However the nature of the experiment leads to a loss of the phase information and as a consequence one could use arbitrary phase values $\beta_{\mathbf{H}}$ and associate them with the measured intensities $|F_{\mathbf{H}}|$ so to obtain multiple density functions $\rho(\mathbf{R})$, all consistent with the collected diffraction pattern. This is what we commonly define as the “phase problem”.

In crystallography, the missing phases are usually derived by self consistency with known physical properties of the crystal, that the electron density is real and mostly confined to the cores of the atoms in the unit cell. The development of computational "direct methods" in the 1950’s led to a revolution in crystallography because it allowed direct inversion of diffraction patterns to atomic-resolution real-space images of the crystal structure [17, 18].

Over the years many authors made important contributions to the solution of the phase problem. A first attempt was made by Patterson in 1934 [19] who modified Eq. 1.5 by replacing the amplitude and the phase of the structure factors by the squared amplitudes proportional to the experimental diffracted intensities. By mapping the maxima of the Patterson function one could determine the position of the interatomic vectors in the crystal and hence determine the crystalline structure in those cases where a strong diffraction spot was present. This method helped to solve the phase problem for crystals which presented "heavy atoms" or for simple structures, but showed its limits for more complex structures [16].

After this first contribution, other methods were developed to experimentally measure the structure factor and its phase. In order to contextualize the work described in this Thesis, a section summarizing few milestones reached in solving the phase problem will be presented at the end of Chapter 3, after providing the theoretical apparatus which is needed to comprehend the physical concepts which these papers are based upon. In this context, this Thesis project presents an innovative experimental technique which uses ptychography [9, 10, 11, 12, 13, 14] to measure the effect of Bragg diffraction on the transmitted phase, collected in the forward direction.

1.1.1 A possible reformulation of the phase problem

In recent years, a series of articles by Emil Wolf presented a new theoretical approach to the solution of the phase problem. In his papers [7][8], Wolf explained that in order to measure the phase of the structure factor, and hence solve the phase problem, the problem itself needed to be reformulated following a different approach. In particular he suggested a new method which could be used to measure the correlation function of an X-ray beam, a quantity that already contains both the amplitude and phase information, provided that the beams used in the experiment are spatially coherent.

In order to approach the problem in a new way he started his analysis by considering the mutual coherence function of a fluctuating field $V(\mathbf{r}, t)$ at point P, which can be written in the form

$$\Gamma(\mathbf{r}_1, \mathbf{r}_2, \tau) = \langle V^*(\mathbf{r}_1, t) V(\mathbf{r}_2, t+\tau) \rangle \,, \tag{1.6}$$

where $\mathbf{r}$ is the position vector which identifies point P at time t. By assuming that the field is statistically stationary [20] one can calculate the Fourier transform of the mutual coherence function

as

$$W(\mathbf{r}_1, \mathbf{r}_2, \omega) = \int_{\infty} \Gamma(\mathbf{r}_1, \mathbf{r}_2, \tau) e^{i\omega\tau} d\tau, \tag{1.7}$$

which represents the cross-spectral density function of the field. This quantity can also be obtained through the frequency-dependent field

$$W(\mathbf{r}_1, \mathbf{r}_2, \omega) = \langle U^*(\mathbf{r}_1, \omega) U(\mathbf{r}_2, \omega) \rangle_{\omega} \tag{1.8}$$

where the average is calculated over the ensemble $\{U(\mathbf{r}, \omega\}$[20, 21]. The cross-spectral density function of the field $W(\mathbf{r}_1, \mathbf{r}_2, \omega)$ can at this stage be assimilated to the averaged intensity at frequency ω of the field at point $P(\mathbf{r})$ in the form

$$W(\mathbf{r}_1, \mathbf{r}_2, \omega) = I(\mathbf{r}, \omega). \tag{1.9}$$

At this stage Wolf's formulation linked the intensity to the spectral degree of coherence of the field fluctuations relative to points $P_1(\mathbf{r}_1)$ and $P_2(\mathbf{r}_2)$

$$\mu(\mathbf{r}_1, \mathbf{r}_2, \omega) = \frac{W(\mathbf{r}_1, \mathbf{r}_2, \omega)}{\sqrt{W(\mathbf{r}_1, \mathbf{r}_2, \omega) W(\mathbf{r}_1, \mathbf{r}_2, \omega)}} \tag{1.10}$$

which can be zero in case of spatial incoherence or one (in modulus) for a complete spatial coherence at frequency ω of the field at the two points $P_1(\mathbf{r}_1)$ and $P_2(\mathbf{r}_2)$. The author carried on his theory establishing a relationship between $\mu(\mathbf{r}_1, \mathbf{r}_2, \omega)$ and the phase difference of the field relative to the two points in the form

$$\mu(\mathbf{r}_1, \mathbf{r}_2, \omega) = e^{i[\phi(\mathbf{r}_2, \omega) - \phi(\mathbf{r}_1, \omega)]}. \tag{1.11}$$

In this way the coherence theory developed by Wolf [7, 8] established a link between the intensity, which can be experimentally measured, and the phase difference between the field in two points.

Wolf theoretically applied his equations to a Young's interference experimental setup, sketched in Fig. 1.3, where an opaque screen with two small openings, placed at $Q_1(\mathbf{r}_1)$ and $Q_2(\mathbf{r}_2)$, is illuminated by a quasi monochromatic beam. In this configuration the resulting interference intensity is collected on a screen B placed parallel to A so to collect the interference pattern. At this stage Wolf expressed

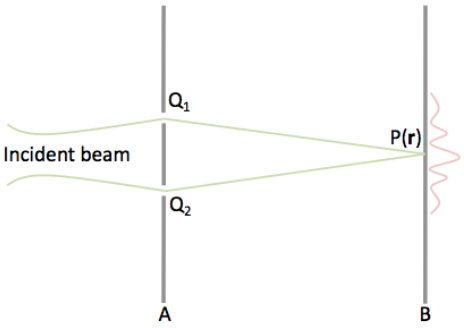

Figure 1.3: Young's interference experimental setup as described in [7].

the average intensity collected at point $P(\mathbf{r})$ on screen B as

$$I(P) = I^{(1)}(P) + I^{(2)}(P) + 2\sqrt{I^{(1)}(P)}\sqrt{I^{(2)}(P)}\,|\mu(Q_1, Q_2, \omega)| \times cos\,[\beta(Q_1, Q_2, \omega) - \delta] \tag{1.12}$$

where $\beta(Q_1, Q_2, \omega)$ is the phase of the spectral degree of coherence $\mu(\mathbf{r}_1, \mathbf{r}_2, \omega)$ and δ is the phase difference associated to the path difference between points $Q_1(\mathbf{r}_1)$ and $Q_2(\mathbf{r}_2)$ at screen A and $P(\mathbf{r})$ on screen B. He concluded that by repeating the intensity measurements for several values of δ one could use Eq. 1.12 to the retrieve the amplitude and phase of $\mu(\mathbf{r}_1, \mathbf{r}_2, \omega)$.

In his 2010 paper [8] Wolf applied this theory to solve the phase problem when performing an X-ray experiment, here described in Fig. 1.4. He considered a spatially coherent and quasi-monochromatic X-ray beam hitting a crystalline medium, with the consequent generation of the transmitted and reflected beams. Imagining to use again screen A and B as described above, he applied Eq. 1.11 so to obtain

$$\mu_{\mathbf{S_0}}(\mathbf{rs}_0, \mathbf{rs}_1, \overline{\omega}) = e^{i\phi_{\mathbf{s_0}}(\mathbf{rs}_1, \overline{\omega})} \tag{1.13}$$

where $\overline{\omega}$ is the mean frequency of the incident X-ray beam, $\mathbf{rs}_0$ and $\mathbf{rs}_1$ are the transmitted and reflected beams directions and $\phi_{\mathbf{s_0}}$ represents the phase of the forward-transmitted beam.

The author concluded stating that measurements of the phase $\phi_{\mathbf{s_0}}(\mathbf{rs}_1, \overline{\omega})$ of the spectral degree of coherence $\mu_{\mathbf{S_0}}(\mathbf{rs}_0, \mathbf{rs}_1, \overline{\omega})$ for all directions of incidence $\mathbf{s}_0$ and scattering $\mathbf{s}_1$ could be used to solve the phase problem [8].

While not providing any experimental evidence to the theory presented in his papers, Wolf's work

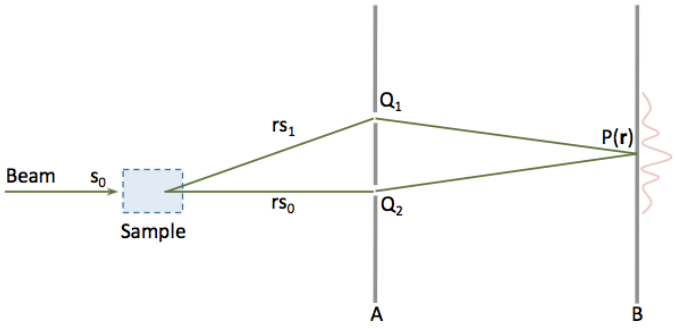

Figure 1.4: Experimental setup as described in [8]. A quasi monochromatic X-ray beam hits a crystal generating a forward-diffracted beam traveling in the $\mathbf{rs}_0$ direction and a reflected beam traveling along $\mathbf{s}_1$. In his paper Wolf described a method to determine the phase of the spectral degree of coherence $\mu_{\mathbf{S_0}}(\mathbf{rs}_0, \mathbf{rs}_1, \overline{\omega})$ at a pair of points $Q_1(r_{\mathbf{S_0}})$ and $Q_2(r_{\mathbf{1}})$.

inspired this Thesis project at a very early stage. In particular, we decided to develop an experimental technique which used the phase relationship between the reflected and transmitted beams in order to measure phase variations generated by Bragg diffraction. In fact, we based our experiments on the belief that the generation of the reflected beam has a perturbative effect on the forward transmitted wave, which in our view was another way of representing an idea close to the one described by Wolf. However, we highlight that the results presented in this Thesis cannot be discussed in relationship to that of Wolf's, given the substantially different theoretical approach that we used.

1.1.2 A new experimental technique developed with the use of ptychography

The experimental technique presented in this Thesis work was developed in order to retrieve the phase of the transmitted beam in forward diffraction. While this methodology will be fully discussed in later chapters, here we summarize the key aspects involved in the project.

In order to detect the phase changes due to Bragg diffraction effects, we used a setup which allowed to measure the forward diffracted intensity while rocking our sample at different angles on and off the Bragg condition, as described in Fig.1.5.

The main challenge in performing the experiments presented in this work was being able to finely detect the phase changes for different rocking angles, given that we were due to deal with relatively

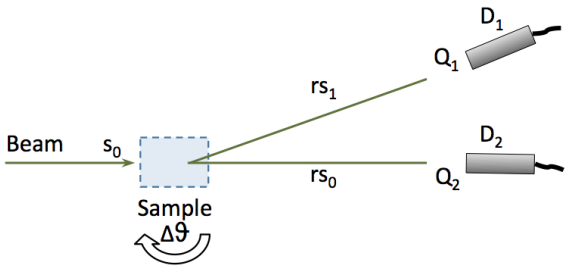

Figure 1.5: Schematic representation of the setup used for the experiments presented in this Thesis work. The sample was mounted in the Laue geometry on a 3D moving stage which allowed for it to be rocked at different angles on and off the Bragg condition. The corresponding rocking curves were measured with the use of the detector in the reflection geometry D_1. Furthermore, in order to perform ptychographic measurements, which require the collection of multiple diffraction patterns at overlapping beams positions projected on the sample, at each rocking angle the sample was also moved respect to the beam so to perform a circular scan. The forward diffracted beams intensities where then measured with detector D_2.

small quantities which could be easily affected by noise and detection errors. In order to retrieve accurate results we decided to use ptychography [13], a powerful imaging technique which proved to have a phase sensitivity as good as 0.005 rad [22]. The adoption of this method allowed to obtain curves representing the transmitted beam's phase shifts as a function of the rocking angle $\Delta\theta$.

In conjunction with this experimental technique, in the following Chapters we will also discuss the theoretical framework which would allow to relate the phase of the structure factor to the phase shift of the forward transmitted beam. While highlighting the fact that the main purpose of this Thesis is to test and develop the experimental technique which can be used to measure the transmitted beam's phase shift with the use of ptychography, we will discuss two main ways of interpreting the obtained results. The first one is an approximate interpretation of the quasi-kinematical regime[1] in which we used kinematical equations to describe the dynamical effect which originates the phase shift through the interaction between the diffracted and forward transmitted beam. We will show in later Chapters that this fitting allowed to obtain a substantially correct description of the experimental curves, but the lack of a fully developed theoretical apparatus failed to provide an equation which could be used to obtain the phase of the structure factor. For this reason, in order to verify the validity of our experimental results, we will also discuss a second method[2] developed by Shabalin, Gorobtsov and Vartanyants and which was used to fit a set of our experimental curves in the dynamical diffraction regime [23]. Finally, we will also illustrate a new *quasi-kinematical* approximation which was recently

[1]This subject is going to be discussed in Chapter 6.
[2]The dynamical fitting will be discussed in Chapter 4.

developed by Gorobtsov and Vartanyants [2] in order to provide a more customized theoretical framework to the regime in which the experiments presented in this Thesis were performed. We believe that the combined use of this innovative theoretical apparatus, together with the experimental techniques described in this Thesis, will allow further investigations in the near future with the possibility to find immediate applications in the investigation of strained crystal structures and in the complete and direct determination of structure factors.

Chapter 2

Kinematical diffraction theory

In this section a basic description of the scattering process will be provided, in a first approximation where we will neglect thermal effects and deformation factors. Starting from the most elementary scattering object, the electron, this Chapter will expand in order to illustrate the kinematical theory that applies to more complex scattering configurations. At the end of this overview, a description of the scattering geometry used in the experiments discussed in this Thesis will be provided, with the aim of giving a theoretical background to the results presented in the following Chapters.

2.1 Scattering by one electron

The scattering of an X-ray beam by a free electron is classically described by saying that the electric field of the incident wave impresses a force on the electronic charge causing its acceleration and the radiation of a scattered wave [1]. The scattering event can be either elastic or inelastic. In the former case, the wavelength λ of the scattered wave, and hence its energy, is the same as the incident one. On the other hand, in the inelastic scattering case the energy of the incoming wave can be partially transferred to the electron, so that the scattered wave is consequently characterized by a lower energy. This scenario, which is commonly described as the Compton effect, may be used to obtain unique information on the electronic structure of materials, but it is not going to be discussed in this Thesis, where we will mainly focus on the elastic scattering.

In order to describe the elastic scattering of an X-ray by a free electron, one must determine the

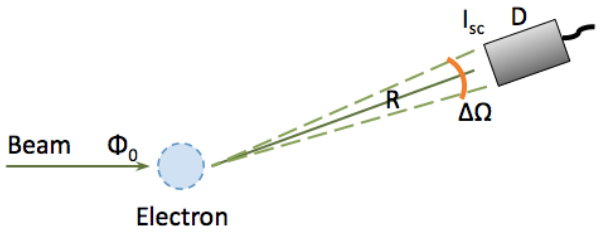

Figure 2.1: Schematic representation of an X-ray scattering experiment. The incoming beam is characterized by the flux Φ_0 which is proportional to the amplitude of the electric field $|E_{in}|^2$ and to the speed of light c. The scattered intensity is proportional to the amplitude of the scattered electric field $|E_{rad}|^2$ collected by the detector as described in [1]. Figure replicated following [1].

differential scattering cross section

$$\left(\frac{d\sigma}{d\Omega}\right) = \frac{I_{sc}}{\Phi_0 \Delta\Omega} \tag{2.1}$$

where I_{sc} is the number of scattered photons recorded in a detector in the time unit, Φ_0 is the flux of the incident beam and $\Delta\Omega$ is the solid angle covered by the detector, as shown in Fig. 2.1 [1]. This quantity is defined as a measure of the scattering event efficiency. At this stage one can rewrite the differential scattering cross section by highlighting the dependency of the flux of the incoming beam and of the number of scattered photons to the respective electric fields intensities. In particular the two terms can be developed as

$$\begin{cases} \Phi_0 \propto c \left|\mathbf{E}_{in}\right|^2 / \hbar\omega \\ I_{sc} \propto c \left(R^2 \Delta\Omega\right) \left|\mathbf{E}_{rad}\right|^2 / \hbar\omega \end{cases}, \tag{2.2}$$

where c is the velocity of light and $\hbar\omega$ represents the energy associated to the wave propagating with cyclic frequency ω [1]. By using the quantities as presented in Eq. 2.2, the differential scattering cross section becomes

$$\left(\frac{d\sigma}{d\Omega}\right) = \frac{\left|\mathbf{E}_{rad}\right|^2 R^2}{\left|\mathbf{E}_{in}\right|^2}. \tag{2.3}$$

The radiated field can be described by noting that when the electron is hit by the incoming beam, it starts vibrating becoming a source of spherical waves which are then consequently radiated in the R direction. By keeping this into account, it is possible to write that the scattered field is a function of

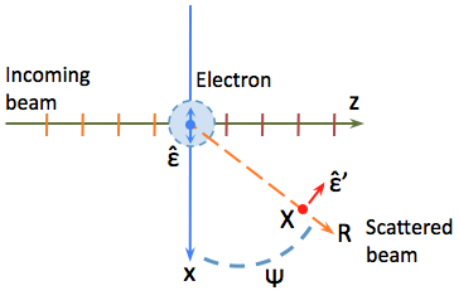

Figure 2.2: Scattering of an X-ray by an electron. In the classical description of this phenomenon, the incoming beam is a plane wave with an associated electric field which is responsible for the electron's vibration (blue arrows). The incoming beam propagates along the z direction and its electric field is polarized along the x axis ($\hat{\epsilon}$). On the other hand, the scattered wave at an observation point X is spherical with a polarization along $\hat{\epsilon}'$. From geometric considerations one can write that $\sin\Psi = -\hat{\epsilon}\cdot\hat{\epsilon}'$ where the minus sign accounts for the 180° phase shift between the incoming and scattered waves as shown in [1]. Figure replicated following [1].

the polarization $\hat{\epsilon}'$ as $\mathbf{E}_{rad} \propto \hat{\epsilon}' e^{ikR}/R$ [1], as described in Fig. 2.2.

In order to evaluate the radiated field at an observation point X, it is necessary to develop the formulation of the scattered electric field further, by also taking the observed acceleration in the electron's vibration into account. One can then write

$$E_{rad}\left(R,t\right) \propto -\frac{e}{R} a_x\left(t'\right)\sin\Psi \tag{2.4}$$

where $-\sin\Psi = (\cos 90° + \Psi) = \hat{\epsilon}\cdot\hat{\epsilon}'$ which, with its negative sign, expresses the π phase shift between the incoming and scattered beams. Term $a_x(t')$ represents the acceleration which, by referring to the classical relationship $F = ma$, can be written as the ratio between the force impressed on the electron and its mass in the form

$$a_x(t') = \frac{-eE_0 e^{-i\omega t'}}{m} = \frac{-eE_{in} e^{-i\omega_0 (R/c)}}{m} = \frac{-eE_{in} e^{-ikR}}{m}, \tag{2.5}$$

where $t' = t - R/c$ represents a time instant earlier than the observation time t and $E_{in} = E_0 e^{-i\omega t}$ is the electric field associated to the incoming beam [1].

It is now possible to write the ratio between the scattered and incoming electric fields as

$$\frac{E_{rad}(R,t)}{E_{in}} \propto \left(\frac{e^2}{m}\right)\frac{e^{ikR}}{R} sin\Psi, \tag{2.6}$$

which must result as a dimensionless quantity. In order to correct the equation in this sense, it is necessary to introduce factors which would give $\left[(e^2/m) * A\right] = [meters]$. This result can be achieved by noting that the classical electron radius, or Thomson scattering length, can be written as

$$r_e = \left(\frac{e^2}{4\pi\epsilon_0 mc^2}\right) = 2.82 * 10^{-5}\mathring{A} \tag{2.7}$$

so that Eq. 2.6 can be written as

$$\frac{E_{rad}(R,t)}{E_{in}} = -r_e\frac{e^{ikR}}{R}\left|\hat{\epsilon}\cdot\hat{\epsilon}'\right|^2 \tag{2.8}$$

which leads to

$$\left(\frac{d\sigma}{d\Omega}\right) = r_e^2\left|\hat{\epsilon}\cdot\hat{\epsilon}'\right| \tag{2.9}$$

representing the differential scattering cross section of an electromagnetic wave by a free electron [1]. Factor $\left|\hat{\epsilon}\cdot\hat{\epsilon}'\right|^2$ denotes the polarization of the X-ray source and has a primary importance when conducting a scattering experiment. According to the type of the X-ray source chosen to perform the experiment, the polarization factor P[1] can have different values

$$P = \left|\hat{\epsilon}\cdot\hat{\epsilon}'\right|^2 = \begin{cases} 1 & synchrotron-\sigma: \quad vertical \quad scattering \quad plane \\ \cos^2\Psi & synchrotron-\pi: \quad horizontal \quad scattering \quad plane \\ \frac{1}{2}\left(1+\cos^2\Psi\right) & unpolarized \quad source \end{cases} . \tag{2.10}$$

In order to calculate the total scattering cross section, one can integrate Eq. 2.9 over all possible angles. Given the rotational symmetry of the system, the average value of the polarization factor over the unit sphere results as 2/3, so that one can obtain that the total cross section is $\sigma_T = 4\pi r_e^2 \times 2/3 =$

[1]In the experiments conducted for this Thesis work a σ polarization was used, so that we assumed a polarization parameter of $P = 1$. However, it is worth mentioning that measurements were at times performed in intermediate polarization states which would have required to apply a correction factor to the polarization parameter. A complete estimate of the polarization condition would require the development of a further theoretical apparatus which, while being outside of the scope of this Thesis work, would represent a valuable next step to this research project.

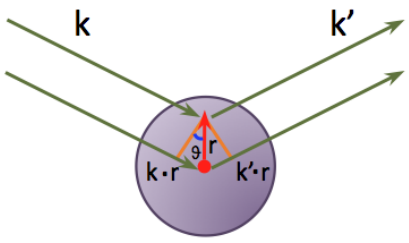

Figure 2.3: Schematic representation of the scattering from an atom as discussed in [1]. In the case of elastic scattering, one can write that $|\mathbf{k}| = |\mathbf{k}'| = 2\pi/\lambda$. Furthermore the phase difference between the two volume elements, one at the centre of the atom and one at position $\mathbf{r}$ is given by the scalar product between the wavevector $\mathbf{k}$ and $\mathbf{r}$. In addition to that, the phase difference between the two scattered waves is given by $-\mathbf{k}\cdot\mathbf{r}$. This can be explained by following what was described in the case of the single electron, where the second volume element at position $\mathbf{r}$ is located at the observation point X, so that it has a wavevector $\mathbf{k}'$ (in the plane wave approximation) and a 180° phase shift respect to the element at the centre of the atom. By combining the two phase shifts one can conclude that $\Delta\phi = (\mathbf{k} - \mathbf{k}') \cdot \mathbf{r}$. Figure replicated following [1].

$0.665 \times 10^{-24} cm^2$ which is a constant value, independent from energy [1].

2.2 Scattering by a single atom

When considering the scattering by a single atom one can think to extend what described in the previous section to a system composed by Z electrons of distribution $\rho(\mathbf{r})$. In order to derive the scattered radiation field, we can describe how the phase of the incoming beam changes while interacting with two volume elements located at the centre of the atom and at position $\mathbf{r}$, as shown in Fig. 2.3. The phase difference between the two waves scattered by the volume elements can be written as

$$\Delta\phi(\mathbf{r}) = (\mathbf{k} - \mathbf{k}') \cdot \mathbf{r} = \mathbf{Q}\cdot\mathbf{r} \tag{2.11}$$

where $\mathbf{Q} = \mathbf{k} - \mathbf{k}'$ is the scattering vector [1]. By following geometric considerations one can further expand the formulation of the scattering vector as

$$|\mathbf{Q}| = 2\,|\mathbf{k}|\sin\theta = \frac{4\pi}{\lambda}\sin\theta \tag{2.12}$$

where the elastic process is taken into account.

At this point that we can derive the total scattering length of the atom by superimposing all the contributions from the different atom's scattering elements of unit volume $d\mathbf{r}$ and position $\mathbf{r}$. By recalling that the phase factor associated to each scattering event is $e^{i\mathbf{Q}\cdot\mathbf{r}}$, one can write that

$$-r_e f^0(\mathbf{Q}) = -r_e \int \rho(\mathbf{r}) e^{i\mathbf{Q}\cdot\mathbf{r}} d\mathbf{r} \tag{2.13}$$

where $-r_e\rho(\mathbf{r})d\mathbf{r}$ is the contribution to the scattered field by each volume element and $f_0(\mathbf{Q}) = \int \rho(\mathbf{r}) e^{i\mathbf{Q}\cdot\mathbf{r}} d\mathbf{r}$ is the atomic structure factor [1]. For different values of the scattering vector $\mathbf{Q}$, the structure factor changes varying between Z and 0. In particular, in the approximation of a spherical atom where we neglect all chemical bonds, we find that $\mathbf{Q} \to 0$ so that $f^0(\mathbf{Q}=0) = Z$, while for $\mathbf{Q} \to \infty$ we get that the scattered waves coming from the different scattering volumes are out of phase, so that $f^0(\mathbf{Q} \to \infty) = 0$.

It is worth noting that the structure factor is also function of the energy of the X-ray wave hitting the atom. In fact, when the incoming beam's energy $\hbar\omega$ is much lower respect to the atomic binding energy (i.e. for electrons in the K shell), the electronic response to the external electromagnetic field is much reduced. On the other hand, when the size of the atom is bigger so that we find electron in more external shells (i.e. L, M, etc.), so that they are less tightly bound, we see that the scattering effect is more relevant. In case $\hbar\omega$ is higher respect to the atomic binding force, the electrons behave as if they were free, otherwise we expect a reduction of the scattering length which is denoted by the real factor f'. Furthermore, an additional imaginary term if'' can be introduced to complete the structure factor formulation, so to also take the dissipation of the system into account [1]

$$f(\mathbf{Q}, \hbar\omega) = f^0(\mathbf{Q}) + f'(\hbar\omega) + f''(\hbar\omega). \tag{2.14}$$

The two additional terms f' and f'' are also known as dispersion corrections to the structure factor. This structure factor formulation also applies to more complex systems, as in the case of crystal structures. To this purpose, it is worth highlighting that the weight the dispersion corrections have on the calculation of the structure factor also varies according to the geometry of the system. In particular, for centric crystals most of the reflections are not much affected by these additional factors [24].

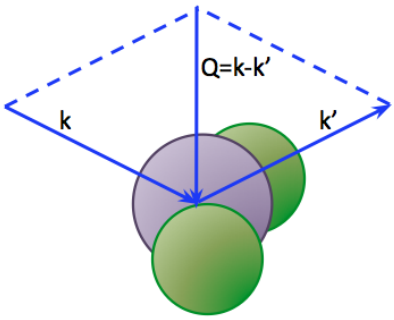

Figure 2.4: Schematic representation of the scattering by a molecule as discussed in [1]. Here the molecule is composed by three atoms and the scattering vector **Q** is described within the scattering triangle generated by the incoming and scattered beams. Figure replicated following [1].

2.3 Scattering by one molecule

In analogy with what discussed for the scattering by one atom, the effect seen when an incoming X-ray beam illuminates a molecule can be described as an extension of the simpler case, as illustrated in Fig. 2.4. In particular the molecule can be considered starting from the atoms which compose it, so that one can say that the total form factor of a molecule is given by the superimposition of the atomic form factors in the form

$$F^{mol}(\mathbf{Q}) = \sum_j f_j(\mathbf{Q}) e^{i\mathbf{Q}\cdot\mathbf{r_j}} \tag{2.15}$$

where j represents the j-th atom in the molecule [1]. Following what discussed in the previous section, the multiplicative term $-r_e$ needs to be included in the formulation when considering the intensity in absolute units.

2.4 Scattering by a crystal

Intuitively, the X-ray scattering by a crystal can be also treated in analogy with the previous sections, by saying that the total scattering amplitude is a superposition of elementary factors. Before looking into this definition more closely, it is worth discussing the nature of the crystalline structure, also highlighting the conditions upon which the X-ray diffraction can be observed.

As previously mentioned in Chapter 1, a crystal can be described by associating a basic element to a regular lattice structure. After defining the origin of the lattice, one can use vectors to define

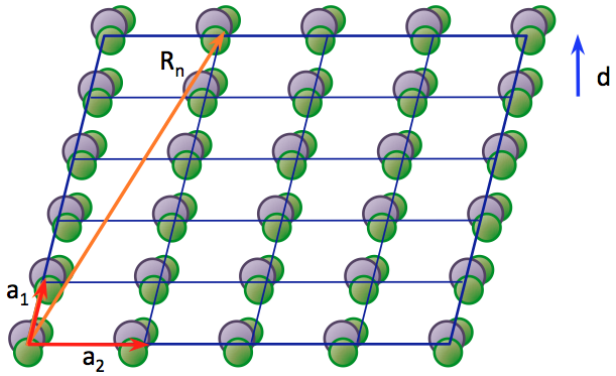

Figure 2.5: Schematic representation of a 2D molecular crystal as discussed in [1]. Here we see that at each point in the lattice corresponds a molecule. The lattice is defined by vector $\mathbf{R_n}$ and the distance between each lattice plane is given by d. In order to specify a particular family of planes, once can use the 3D Miller indices (h, k, l) which identify a set of points on the $\mathbf{a_i}$ axes defined as $(\mathbf{a}_1/h, \mathbf{a}_2/k, \mathbf{a}_3/l)$. For different families of planes, the spacing d is defined by $d = \frac{a}{\sqrt{h^2+k^2+l^2}}$, where a is the elementary lattice parameter. In this 2D figure, assuming that $|\mathbf{a}_1| = |\mathbf{a}_2| = a$, we can assume to look at the family of planes defined by the Miller couple (1,0), so that $d = a$. Figure replicated following [1].

the elementary unit of the crystal, which is commonly known as unit cell. The unit cell is defined as primitive, as shown in Fig. 2.5, when the modulus of its the defining vectors is minimum. In other cases the unit cell can be defined as non-primitive or non-conventional when it is defined by vectors with a higher modulus or different orientation. In the following discussion, a crystal defined by a primitive unit cell will be considered.

In the 3 dimensions, the lattice defining the crystalline structure can be identified by a set of vectors in the form

$$\mathbf{R_n} = n_1\mathbf{a_1} + n_2\mathbf{a_2} + n_3\mathbf{a_3}$$

where n_i are integers and $\mathbf{a}_i$ are the basis lattice vectors. We can now use this quantity to define the scattering amplitude of the crystal

$$F^{crystal} = \sum_j f_j(\mathbf{Q}) e^{i\mathbf{Q}\cdot\mathbf{r}_j} \sum_n e^{i\mathbf{Q}\cdot\mathbf{R}_n} \tag{2.16}$$

where we are neglecting the factor $-r_e$ and where the first term represents the unit cell structure factor, which in case of scattering by a molecular crystal is defined by Eq. 2.15, while the second term, known as lattice sum, represents the crystalline structure composed by N unit cells [1].

It is worth noting that the lattice sum is a superimposition of phase elements rotating in the unit circle. In case

$$\mathbf{Q} \cdot \mathbf{R_n} = 2\pi \times integer \tag{2.17}$$

each term in the sum becomes real and equal to one, so that the sum of all elements is N, the total number of unit cells in the crystal. On the contrary, when this condition is not satisfied the sum will be of order unity. At this stage, in order to understand when Eq. 2.17 is satisfied, we need to introduce the concept of reciprocal lattice, which is a geometrical construction defined as

$$\mathbf{H} = h\mathbf{a_1^*} + k\mathbf{a_2^*} + l\mathbf{a_3^*} \tag{2.18}$$

where (h, k, l) are integers and

$$\mathbf{a_1^*} = 2\pi \frac{\mathbf{a_2} \times \mathbf{a_3}}{\mathbf{a_1} \cdot (\mathbf{a_2} \times \mathbf{a_3})}, \quad \mathbf{a_2^*} = 2\pi \frac{\mathbf{a_3} \times \mathbf{a_1}}{\mathbf{a_1} \cdot (\mathbf{a_2} \times \mathbf{a_3})}, \quad \mathbf{a_3^*} = 2\pi \frac{\mathbf{a_1} \times \mathbf{a_2}}{\mathbf{a_1} \cdot (\mathbf{a_2} \times \mathbf{a_3})}, \tag{2.19}$$

where $\mathbf{v_c} = \mathbf{a_1} \cdot (\mathbf{a_2} \times \mathbf{a_3})$ is the volume of the unit cell. We can now calculate the product between the reciprocal and direct lattice vectors to obtain

$$\mathbf{H} \cdot \mathbf{R_n} = \mathbf{2}\pi(hn_1 + kn_2 + ln_3) = 2\pi \times integer, \tag{2.20}$$

which gives the same result as that of Eq. 2.17, so that one can write that the condition upon which the lattice sum equals the number of unit cells in the crystal is that

$$\mathbf{Q} = \mathbf{H}. \tag{2.21}$$

This result implies that the crystal structure factor $F^{crystal}(\mathbf{Q})$ is not vanishing only if the scattering vector $\mathbf{Q}$ coincides with a reciprocal lattice vector [1]. This equation is known as the Laue condition for the observation of X-ray diffraction and one can show its equivalence to the Bragg's Law, which states that scattering of X-rays by a crystal happens when the constructive interference of waves takes place in the form

$$m\lambda = 2dsin\theta, \tag{2.22}$$

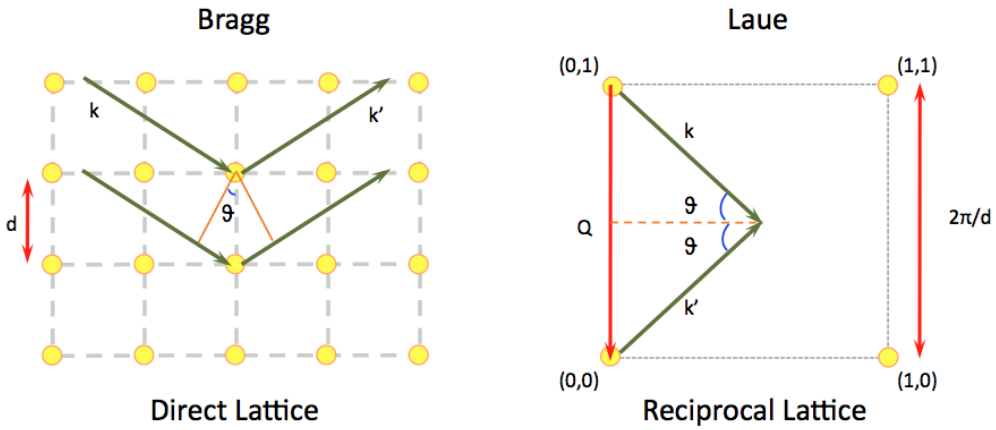

Figure 2.6: Schematic representation of the equivalence between Bragg's Law and Laue condition as discussed in [1]. The scattering by the (0,1) family of planes in the real lattice is represented in the reciprocal space, where we see that the amplitude of the scattering vector is $|\mathbf{Q}| = 2\pi/d$. Figure replicated following [1].

where m is an integer, d is the spacing between lattice planes and θ is the incidence angle.

The equivalence between the Laue condition and the Bragg's Law is also highlighted in the relationship between the direct lattice and the reciprocal one. In particular a set of crystallographic planes identified by a combination of Miller indices is represented in the reciprocal space by a point in the reciprocal space. Furthermore the reciprocal space vector $|\mathbf{H}_{hkl}|$ is perpendicular to the planes identified by (h, k, l) and its modulus is $|\mathbf{H}_{hkl}| = \frac{2\pi}{d_{hkl}}$ where $d_{hkl} = \frac{a}{\sqrt{h^2+k^2+l^2}}$ [1]. By considering the geometries described in Fig. 2.6, one can note that the Laue condition implies that $|\mathbf{Q}| = |\mathbf{H}_{hkl}| = \frac{2\pi}{d_{hkl}}$ so that we can write

$$\begin{aligned} |\mathbf{Q}| &= 2\,|\mathbf{k}| \sin\theta, \qquad real \quad space \\ |\mathbf{Q}| &= \tfrac{2\pi}{d_{hkl}}, \qquad reciprocal \quad space \end{aligned} \tag{2.23}$$

where we are assuming the case of elastic scattering so that $|\mathbf{k}| = |\mathbf{k}'| = 2\pi/\lambda$. By equating the two relationships one can then obtain

$$\lambda = 2d_{hkl} \sin\theta$$

which is the Bragg's Law for $m = 1$.

In more detail, the lattice sum can be analyzed in one dimension by developing the sum of all phase

terms as

$$\begin{array}{l} S_N(Q) = \sum_n^{N-1} e^{iQna} \\ |S_N(Q)| = \frac{\sin(NQa/2)}{\sin(Qa/2)} \end{array} , \tag{2.24}$$

where the lattice vector is defined by $R_n = na$, where n is an integer and a is the lattice constant, and where the the sum is developed in the geometrical series

$$S_N = \sum_{n=0}^{N-1} k^n = 1 + k + k^2 + ... + k^{N-1} = \frac{1 - k^N}{1 - k}. \tag{2.25}$$

The lattice sum becomes N when the Laue condition $\mathbf{Q} = \mathbf{H}$ is satisfied, while when this condition is not fully achieved one can write that

$$|S_N(Q)|^2 \to Na^* \sum_{G_h} \delta(Q - H_h) \tag{2.26}$$

where $a^* = 2\pi/a$. Similar considerations apply to the two and three dimensions cases so to obtain

$$\begin{array}{l} |S_N(\mathbf{Q})|^2 \to NA^* \sum_{\mathbf{G}} \delta(\mathbf{Q} - \mathbf{H}), \quad 2D \\ |S_N(\mathbf{Q})|^2 \to Nv_c^* \sum_{\mathbf{G}} \delta(\mathbf{Q} - \mathbf{H}), \quad 3D \end{array} \tag{2.27}$$

where A^* and v_c^* are the reciprocal space area and the volume, respectively [1].

At this stage we can develop the other element which composes the crystal scattering amplitude: the unit cell structure factor. By recalling Eq. 2.16, the unit cell structure factor can be written in the form

$$F_H^{fcc} = \sum_j f(\mathbf{H})_j e^{i\mathbf{H}\cdot\mathbf{r_j}} \tag{2.28}$$

which refers to a face centered cubic crystalline structure and where the Laue condition is taken into account. In this geometry, vectors $\mathbf{r}_j$ represent the position of the four atoms at the vertices of the cubic unit cell, while the reciprocal lattice vector is $\mathbf{H} = \left(\frac{2\pi}{a}\right)(h, k, l)$. In the case where all atoms in the unit cell are the same, the atomic scattering factor $f(\mathbf{H})$ is a constant which can be taken outside from the sum, so that one can write

$$F_H^{fcc} = f(\mathbf{H}) \sum_j e^{i\mathbf{H}\cdot\mathbf{r_j}} = f(\mathbf{H}) \left(1 + e^{i\pi(h+k)} + e^{i\pi(k+l)} + e^{i\pi(l+h)}\right) \tag{2.29}$$

which gives

$$F_H^{fcc} = f(\mathbf{H}) \times \begin{cases} 4 & h,k,l \quad all \quad even \quad or \quad all \quad odd \\ 0 & otherwise \end{cases} . \tag{2.30}$$

The result shows that for a fcc structure the {100} reflection is forbidden because it would lead to a vanishing structure factor, while reflections {111} and {200} are allowed [1].

At this stage we can summarize the presented results by saying that when a 3D crystalline sample is fully illuminated by an X-ray beam, the differential cross-section, defined as the ratio between the number of X-rays scattered in the time unit into the solid angle $d\Omega$ and the incident flux per solid angle unit, can be written as

$$\left(\frac{d\sigma}{d\Omega}\right) = r_e^2 P \left|F(\mathbf{Q}\right|^2 N v_c^* \delta(\mathbf{Q} - \mathbf{H}). \tag{2.31}$$

By integrating the cross-section over angle θ and by multiplying the incident flux ϕ_0, one can obtain the integrated scattered intensity as

$$I_{sc} = \phi_0 r_e^2 P \left|F(\mathbf{Q}\right|^2 N \frac{\lambda^3}{v_c} \frac{1}{sin2\theta} \tag{2.32}$$

where $v_c = a^3$ is the volume of the unit cell in the real space and $1/sin2\theta$ is known as the Lorentz factor [1].

2.5 X-ray reflection and transmission by one atomic layer

When an X-ray beam hits a layer of unit cells, a reflected and a diffracted waves are generated. As a first step in describing the quantities needed to define the resulting waves, one need to start considering that for X-rays the refractive index is written in the form

$$n = 1 - \delta + i\beta \tag{2.33}$$

where we see that its real part is less than unity, which implies that the phase velocity of the wave traveling in the material c/n is larger than the speed of light c[2] [1]. The imaginary part of the refractive index β is associated to the absorption taking place in the material and is usually much smaller than δ, which usually is of order 10^{-5} in solid materials. If we consider that the electromagnetic field associated to a traveling wave in air can be written, for the one dimension approximation, in the form

$$\psi(z,t) = \psi_0 e^{i(kz-\omega t)}, \tag{2.34}$$

when we consider the presence of a medium we can write

$$\begin{aligned} \psi(z,t) &= \psi_0 e^{i(k(1-\delta+i\beta)z-\omega t)} \\ \psi(z,t) &= \psi_0 e^{i(kz-\omega t)} e^{-ik\delta z} e^{-k\beta z} \end{aligned} \tag{2.35}$$

which shows that δ is related to the phase shift of the wave transmitted through the material, while β has the effect of modulating the field's amplitude.

We can now write the equation for the transmitted wave in the case of an X-ray beam hitting a thin layer of unit cells in the form

$$T = A(1 - ig_0) \approx e^{-ig_0} \tag{2.36}$$

where we are assuming that there is no absorption and where A is the incoming X-ray beam and

$$g_0 = \frac{\lambda \rho_{at} f^0(0) r_e d}{sin\theta}, \tag{2.37}$$

which depends on d, the thickness of the medium, on ρ_{at}, the atomic number density, and on the unit cell structure factor in the forward direction $\mathbf{Q} = 0$ [1]. A sketch representing this diffraction geometry is presented in Fig. 2.7. It is worth noting that factor $\sin\theta$ was introduced to take the change in the medium thickness into account when modifying the incidence angle and that in this configuration δ can be defined as

$$\delta = \frac{2\pi \rho_{at} f^0(0) r_e}{k^2}, \tag{2.38}$$

where $k = 2\pi/\lambda$.

[2]This statement does not violate the law of relativity because the phase velocity does not carry any information. It can be shown that the group velocity of the wave traveling inside the material is indeed less than c [1].

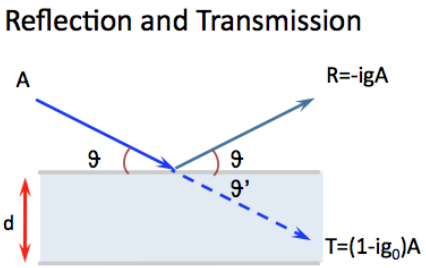

Figure 2.7: Schematic representation of an X-ray beam A incident on a layer of unit cells, as formulated in [1]. The scheme shows that the transmitted wave T travels along the incoming beam's direction, while being affected by a phase shift. The reflected wave R is obtained by considering the complex reflectivity factor $-ig$, where $g = \frac{\lambda \rho r_e d}{\sin\theta}$ as also discussed in the text. Figure replicated following [1].

The reflected beam can be calculated by imposing continuity between the incoming beam and the two generated waves. In particular one can write the three waves in the form

$$\begin{cases} A = a_I e^{i\mathbf{k_I}\cdot\mathbf{r}} \\ R = a_R e^{i\mathbf{k_R}\cdot\mathbf{r}} \\ T = a_T e^{i\mathbf{k_T}\cdot\mathbf{r}} \end{cases}, \tag{2.39}$$

so that the continuity boundary conditions translate to

$$\begin{aligned} a_I + a_R &= a_T \\ a_I\mathbf{k}_I + a_R\mathbf{k}_R &= a_T\mathbf{k}_T \end{aligned}. \tag{2.40}$$

By noting that the wavenumber in vacuum is $k = |\mathbf{k_I}| = |\mathbf{k_R}|$ while in the medium it is $nk = |\mathbf{k_T}|$, one can develop the boundary conditions equations taking the $\mathbf{k}$ parallel and perpendicular components so to obtain

$$\begin{aligned} a_I k\cos\theta + a_R k\cos\theta &= a_T nk\cos\theta' \\ -(a_I - a_R)k\sin\theta &= -nk\sin\theta' \end{aligned}. \tag{2.41}$$

From the two equations one can derive the Snell's law[3]

$$\cos\theta = n\cos\theta' \tag{2.42}$$

[3]When $\theta' = 0$, Snell's law leads to the definition of the critical angle $\theta_c = \sqrt{2\delta}$ which gives the limit for which we observe total external reflection, under the condition $\theta < \theta_c$.

and the Fresnel equations

$$\begin{aligned} r &\equiv \frac{a_R}{a_I} = \frac{\theta-\theta'}{\theta+\theta'} \\ t &\equiv \frac{a_T}{a_I} = \frac{2\theta}{\theta+\theta'} \end{aligned} \tag{2.43}$$

which define the amplitude reflectivity and transmittivity factors [1]. The reflectivity factor r can be further developed by noting that the wavevector $Q = 2k\sin\theta \cong 2k\theta$ and that $Q_c = 2k\sin\theta_c \cong 2k\theta_c$. In this way one can write that

$$r(q) = \frac{q - q'}{q + q'} \tag{2.44}$$

where we consider

$$q = \frac{Q}{Q_c} \cong \left(\frac{2k}{Q_c}\right)\theta \quad , \quad q' = \frac{Q'}{Q_c} \cong \left(\frac{2k}{Q_c}\right)\theta' \tag{2.45}$$

and where

$$q^2 = q'^2 + 1 - 2ib_\mu \tag{2.46}$$

which also takes the absorption term $b_\mu = \left(\frac{2k}{Q_c}\right)^2 \beta$ into account [1].

In the case that refraction effects can be neglected and that the diffracting layer is thin ($Qd \ll 1$) [1] one obtains

$$r \cong -i\frac{4\pi\rho r_e d}{Q} = -i\frac{\lambda\rho r_e d}{\sin\theta} \tag{2.47}$$

which is the factor shown in Fig.2.7 as $r = -ig$ with $g = \frac{\lambda\rho r_e d}{\sin\theta}$. By recalling Eq. 2.37 we can note that

$$g_0 = \frac{|F_0|}{|F_H|}g \tag{2.48}$$

where F_0 and F are the unit cell structure factors in the forward and reflected directions, respectively.

In the end, it is worth mentioning that diffraction experiments can be performed in different geometries. In particular, Fig. 2.8 illustrate the symmetric Bragg and Laue reflection geometries.

2.6 Reflection from a set of atomic layers

The total reflected wave from a crystal can be described by considering the effect given by a number of atomic layers. In particular, here we show that the total reflected wave can be obtained as a superposition of the waves reflected by each plane. If we consider that the reflectivity for each layer is given by g, we can calculate the total contribution given by N layers in case where $Ng \ll 1$ by adding

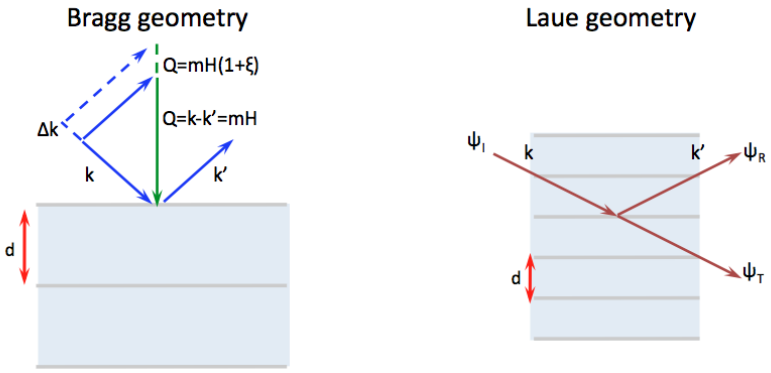

Figure 2.8: Schematic representation of the symmetric Bragg and Laue reflection geometries as discussed in [1], where the angle formed between the exit beams and the crystallographic planes is the same as the incident one. Here we consider a parallel and white incident beam which is reflected by a perfect crystal with a relative wavelength band $\xi = (\Delta\lambda/\lambda)$. This effect can be explained by noting that even a perfect crystal, free from the presence of defects, does not reflect a collimated beam perfectly, with an infinitely sharp response, but it introduces an intrinsic width ξ. As a result of this effect, we have a variation of the scattering vector, so that $\mathbf{Q} = m\mathbf{H}(1+\xi)$. In the Laue reflection geometry, we see that both the reflected and transmitted waves exit the crystal from the same surface. The experiments that will be discussed in the following Chapters were realized using this geometry. Figure replicated following [1].

all the reflected amplitudes and by considering the phase factor introduced by each j-th layer e^{iQd_j} as

$$r_N(Q) = -ig \sum_{j=0}^{N-1} e^{i(Qd-2g_0)j}, \tag{2.49}$$

where d is the distance between planes and where term $2g_0$ refers to the fact that each layer is traversed twice in the T and R direction [1]. By noting that a stack of layers in the direct space is equivalent to a line of points in the reciprocal space at multiples of H so that $Q{=}mH = m2\pi/d$, we can calculate the reflectivity factor for a small deviation of the scattering vector, so that

$$Q{=}mH(1+\xi) \tag{2.50}$$

where

$$\xi = \frac{\Delta Q}{Q} = \frac{\Delta k}{k} = \frac{\Delta\lambda}{\lambda}. \tag{2.51}$$

The sum of the phase factors introduced by the reflection from N layers can be now written as

$$\sum_{j=0}^{N-1} e^{i(Qd-2g_0)j} = \sum_{j=0}^{N-1} e^{i2\pi(m\xi-g_0/\pi)j} \tag{2.52}$$

which is a geometrical series that can be summed as

$$\sum_{j=0}^{N-1} e^{i2\pi(m\xi-g_0/\pi)j} = \frac{1-e^{i2\pi N(m\xi-g_0/\pi)}}{1-e^{i2\pi(m\xi-g_0/\pi)}} \tag{2.53}$$

so that we can obtain

$$r_N(\xi) = -ig\frac{\sin\left(\pi N\left[m\xi-g_0/\pi\right]\right)}{\sin\left(\pi\left[m\xi-g_0/\pi\right]\right)}e^{i(N-1)\pi(m\xi-g_0/\pi)} \tag{2.54}$$

where the reflectivity amplitude is

$$|r_N(\xi)| = g\left|\frac{\sin\left(\pi N\left[m\xi-g_0/\pi\right]\right)}{\sin\left(\pi\left[m\xi-g_0/\pi\right]\right)}\right| \tag{2.55}$$

as discussed in [1]. It is worth highlighting that this equation will be used in this Thesis to provide an approximation for the experimental results fittings.

The kinematical theory discussed so far was developed under the assumption of a perfect and thin crystal, where multiple scattering events between the transmitted and reflected waves are neglected. This approximation can be acceptable if the thickness of the crystal is small enough so that the reflected and diffracted beams exit the sample before multiple scattering events can take place. However, in order to establish the limits of this approximation, we also need to develop the dynamical theory of X-ray diffraction which describes in more detail what are the effects caused my multiple scattering. This subject will be discussed in the following Chapter.

Chapter 3

Dynamical theory of X-ray diffraction

The theory developed in the previous Chapter was based on the underlying assumption that each individual diffraction event inside the crystal acts independently. Away from this approximation, one can show that many complications can occur. For this reason, in order to give a more complete description of X-ray scattering by perfect crystals, we need to discuss the dynamical theory of X-ray diffraction. In this Chapter an overview of the main topics covered by this theoretical approach will be provided, so to give a more detailed description of the physical effects involved in the experiments presented in the following Chapters. Once again, we will neglect the effects of thermal and deformation factors.

3.1 Dynamical diffraction regime

In order to describe the dynamical diffraction regime we can analyze what happens when an X-ray beam is used to illuminate a perfect crystal of a given thickness Nd. By recalling what was previously discussed in Chapter 2, we know that when an X-ray beam is incident at an angle θ that satisfies Bragg's Law, it will be reflected at the same angle θ as shown in Fig. 3.1.a. Because the angular direction is maintained, the diffracted ray will continue to satisfy Bragg's Law and therefore will diffract a second time (blue point in Fig. 3.1.a) inside the crystal. In the end, the reflected beam will also travel in the direction of the original incident beam, so similarly it will generate other diffraction events. Under this

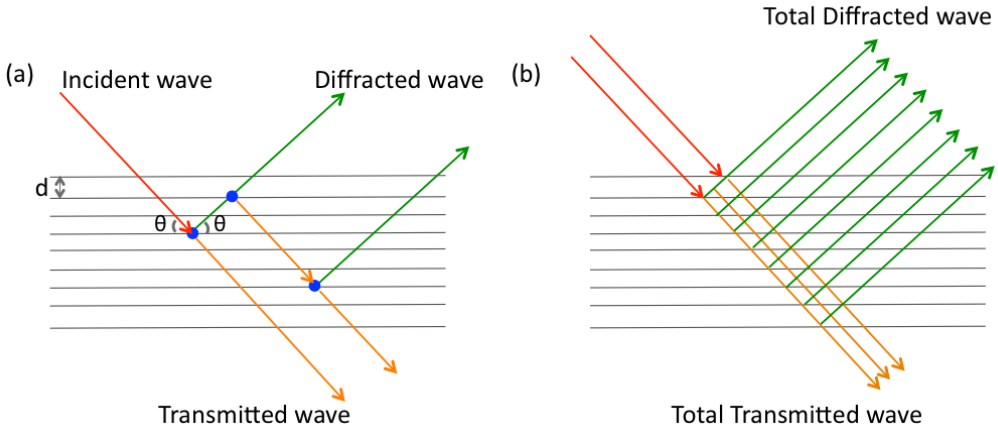

Figure 3.1: Dynamical diffraction schematic representation. (a) The incident beam interacts with the specimen at different crystallographic planes. The diffracted beam is composed by waves diffracted from different loci inside the crystal. (b) Schematic representation of the diffracted beam obtained when scattering from all planes is taken into account.

condition, we can suppose that if the whole crystal is perfect and is illuminated with an X-ray beam, multiple diffraction events will take place throughout the crystal. As a result, we can assume that all the generated waves will interfere with each other so to originate a total diffracted wave, as shown in Fig. 3.1.b. This process was described by Ewald during the early part of the 20th century [25]. This theory, in which the diffraction is so strong that it affects the intensity of the primary beam, is referred to as dynamical regime. At this stage, we can acknowledge that, in a first approximation, the assumptions made to develop the kinematical model can only be applicable if the diffracting crystal is so thin that dynamical effects do not have enough space to occur.

An effect related to dynamical diffraction is the Borrmann effect or *anomalous transmission* [26], for which the intensities of transmitted beams are different when considering thin and thick crystals. In particular, for thin crystals we note that when varying the X-ray beam's incidence angle, a drop in the transmitted beam can be observed in correspondence of the Bragg angle, as shown below in Fig. 3.2.c. This can be explained by noting that the conservation of energy implies that the generation of a diffracted beam at the Bragg condition affects the transmitted wave by lowering its intensity. The Borrmann effect can be observed when repeating the same experiment for thick crystals. In this case when meeting the Bragg condition, the transmitted intensity shows a peak which apparently violates the conservation of energy. In a very first attempt to explain this effect, one can say that part of

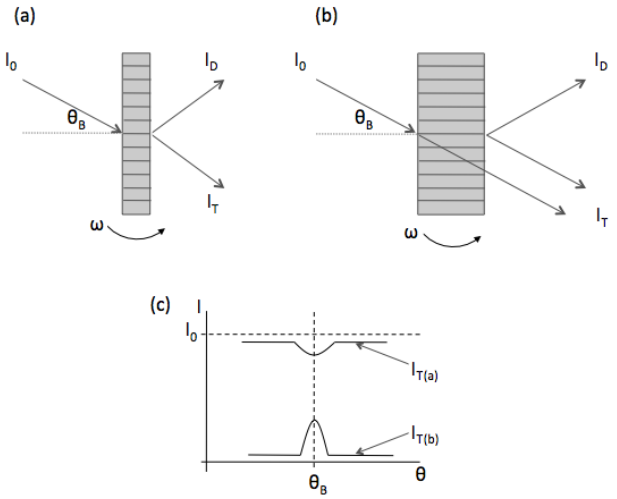

Figure 3.2: Anomalous transmission schematic. A thin (a) and a thick (b) crystals are illuminated in the Laue geometry. (c) Transmitted intensity for the thin and thick crystals versus the rocking angle. When the Bragg condition is met we observe a drop in the transmitted beam for the thin crystal and a peak for the thick one. It is worth noticing that in both cases the intensity of the transmitted wave is lower than the incoming one. This is can be explained by taking photoelectric absorption into account and remembering that $I_t = I_0 e^{-\mu_0 t}$ where μ_0 is the absorption coefficient an t is the thickness of the crystal. We can assume that in case (a) $\mu_0 t \ll 1$, while in case (b) $\mu_0 t > 10$. Figure replicated following [26].

the incoming beam travels inside the crystal along the crystallographic planes and emerges on the exit surface. On the other hand, a more detailed description of the Borrmann effect was given by Batterman and Cole, who explained that the *forward diffracted* beam is generated by the presence of a standing wave pattern whose nodes coincide with the atomic sheets, thus prevent for photoelectric absorption to take place within thick crystals [26].

3.1.1 Theoretical background

In order to give a more formal description to the Borrmann effect and more in general to dynamical diffraction effects, we need to develop some preliminary notions which are going to be useful in understanding the following sections.

The first aspect that it is worth highlighting is how a crystal can be described as a periodic dielectric constant. This can be done by including this information in the definition of the structure factor.

By recalling what stated in the previous Chapter, we can write the structure factor for the (hkl) reflection, given the reciprocal lattice vector $\mathbf{H} = h\mathbf{a_1^*} + k\mathbf{a_2^*} + l\mathbf{a_3^*}$ as

$$F_H = \int_V \rho\left(\mathbf{r}\right) e^{(i2\pi\mathbf{H}\cdot\mathbf{r})} dv$$

where V is the volume of the unit cell. If we assume that there are n atoms in one unit cell and that each one of them can be considered as a rigid sphere, F_H can be obtained by the sum of discrete quantities in the form

$$F_H = \sum_n f_n e^{(i2\pi\mathbf{H}\cdot\mathbf{r_n})} \tag{3.1}$$

where f_n is the atomic scattering factor of the nth atom.

The electric field $\mathbf{E}$ in a dielectric material causes the bound charges (atomic nuclei and their electrons) to separate thus inducing a local electric dipole moment. The electric displacement field $\mathbf{D}$ can be defined as

$$\mathbf{D} = \epsilon_0\mathbf{E} + \mathbf{P} \tag{3.2}$$

where ϵ_0 is the vacuum permittivity and $\mathbf{P}$ is the polarization factor. In a linear, homogeneous and isotropic dielectric $\mathbf{P}$ depends linearly on $\mathbf{E}$ so that we can write

$$\mathbf{P} = \epsilon_0\chi\mathbf{E} \tag{3.3}$$

where χ is the electric susceptibility of the material[1]. At this point the electric displacement field becomes

$$\mathbf{D} = \epsilon_0\mathbf{E} + \mathbf{P} = \epsilon_0\kappa\mathbf{E} \tag{3.4}$$

[1]The electric susceptibility is related to the electron density ρ and to the electron radius r_e by the equation $\chi = -r_e\lambda^2\rho/\pi$ [1, 2].

where $\kappa = 1 + \chi$ is the dielectric constant, which can also written in the form

$$\kappa = 1 + \frac{\mathbf{P}}{\epsilon_0 \mathbf{E}}. \tag{3.5}$$

At this stage we want to relate the dielectric constant, which is a function of polarization and electric field, to the structure factor so to really provide a complete description of the crystal. This step can be done by first relating it to the electron density $\rho(\mathbf{r})$ in the form

$$\kappa(\mathbf{r}) = 1 - r_e \frac{\lambda^2}{\pi} \rho(\mathbf{r}) \tag{3.6}$$

where r_e is the electron radius[2]. After introducing the symbol Γ

$$\Gamma = \frac{r_e \lambda^2}{\pi V},$$

we can rewrite the dielectric constant as a Fourier series in the form

$$\kappa(\mathbf{r}) = 1 - \Gamma \sum_H F_H e^{(-i2\pi \mathbf{H}\cdot\mathbf{r})}. \tag{3.7}$$

It is now worth recalling that the atomic scattering factor is also a complex quantity in the form

$$F_H = \sum_n \left(f + \Delta f^{'} + i\Delta f^{''} \right)_n e^{(i2\pi \mathbf{H}\cdot\mathbf{r})} = \sum_n \left(F_H^{'} + iF_H^{''} \right)_n e^{(i2\pi \mathbf{H}\cdot\mathbf{r})} \tag{3.8}$$

where $\Delta f^{'}$ and $\Delta f^{''}$ are the dispersion correction corrections that also take resonance and absorption into account, as discussed in the previous Chapter and as recalled by Batterman and Cole [26], who noted that the importance of this two additional factor resides in the fact that for the case of $hkl = 000$ the dielectric constant is still complex in the form

$$\kappa_0 = 1 - \Gamma \left[F_0^{'} + iF_0^{''} \right] \tag{3.9}$$

where $F_0^{'}$ and $F_0^{''}$ are real quantities. It is worth noticing that the linear absorption coefficient is

[2]This equation can be derived after considering $\mathbf{P} = \rho(\mathbf{r})\, ex$ where e is the electron charge and x is the amplitude electron motion induced by a sinusoidal electric field $\mathbf{E}$ [26].

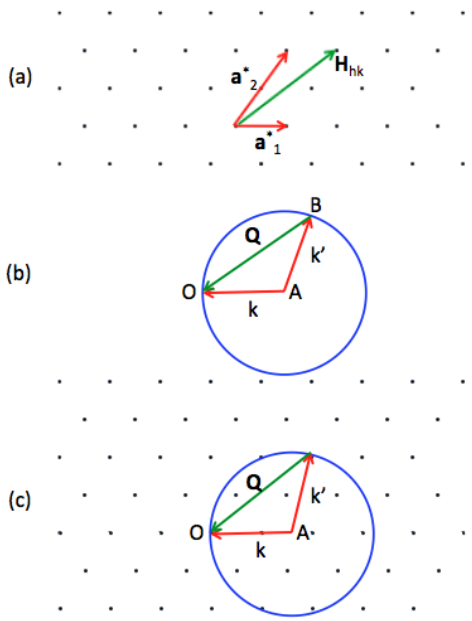

Figure 3.3: Construction of the 2D Ewald circle as discussed in [1]. (a) A reciprocal lattice is shown for points given by $\mathbf{H} = h\mathbf{a}_1^* + k\mathbf{a}_2^*$, with $h = 1$ and $k = 2$. (b) We define a circle of radius k=AO where $\mathbf{k}$ represents the incoming wave vector. The scattered wave is also represented by vector $\mathbf{k}'$ which in this case has equal modulus of $\mathbf{k}$. The scattering vector $\mathbf{q}$ is once again given by $\mathbf{q} = \mathbf{k} - \mathbf{k}'$ and is represented by a chord in the circle. (c) By superimposing (a) and (b) we obtain the Ewald circle, where point O is the reciprocal lattice origin. Figure replicated following [1].

related to the imaginary part of the average dielectric constant

$$\mu_0 = \frac{2\pi}{\lambda}\Gamma F_0'' . \tag{3.10}$$

Before developing further the theory which is going to be used in the following sections, it is worth introducing a useful graphical tool which is going to be helpful in describing the effects related to dynamical diffraction: the Ewald circle [1].

Let us consider the 2D case where the lattice points are given by $\mathbf{H} = h\mathbf{a}_1^* + k\mathbf{a}_2^*$ and where, in the case $h = 1$ and $k = 2$, the resulting $\mathbf{H}_{hk}$ vector is the one shown in Fig. 3.3.a. We can now define a circle where a monochromatic incident radiation $\mathbf{k} = AO$ can be scattered to any wave vector $\mathbf{k}' = AB$ terminating on the circle of radius k, as presented in Fig. 3.3.b. The Ewald circle is obtained in Fig. 3.3.c, where vector $\mathbf{k}$ is on the origin of the reciprocal lattice O. It is worth noticing that the scattering vector $\mathbf{Q}$ is a chord in the Ewald circle and that, as previously mentioned, it is obtained from the

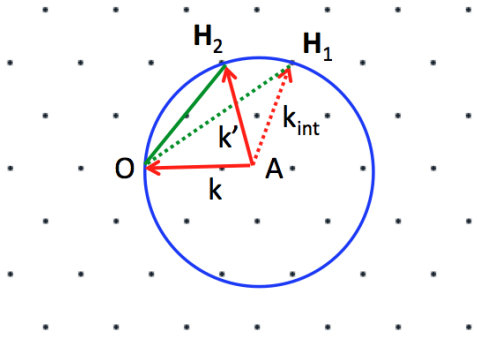

Figure 3.4: Multiple scattering in the Ewald circle as discussed in [1]. Figure replicated following [1].

incident and scattered wave vectors. We can furthermore note that the Laue condition, $\mathbf{Q} = \mathbf{H}$, is fulfilled for all reciprocal lattice points falling on the circle and that by positioning a detector in the direction of the corresponding $\mathbf{k}'$ vector, we can observe a diffraction peak.

If two or more reciprocal lattice points fall on the Ewald circle we have the condition of multiple scattering, as shown in Fig. 3.4. In this case, in order to consider the $\mathbf{H}_2$ reflection, we can rotate the crystal and the detector so to maximize the corresponding peak along the $\mathbf{k}'$ direction. However, even in this configuration we will have additional contributions given by $\mathbf{H}_1$. In fact, because $\mathbf{H}_1$ is on the circle, the incident beam will also be scattered to $\mathrm{k_{int}}$. This means that inside the crystal $\mathbf{k}_{int}$ is scattered to $\mathbf{k}'$ by the reflection $\mathbf{H}_2 - \mathbf{H}_1$, so that an additional intensity may appear along the $\mathbf{k}'$ direction.

It is worth noticing that the thickness of the Ewald circle is related to the bandwidth of the incident radiation Δk. In the case of a white beam, all reflections will be observed within the circles of radius equal to the maximum and minimum $\mathbf{k}$ vector in the beam, as shown in Fig. 3.5. Furthermore, we can note that all the reciprocal lattice points in the white area enclosed by the bigger circle will reflect simultaneously [1].

Similar results can be obtained when considering the three dimensional case, which leads to the construction of the Ewald sphere.

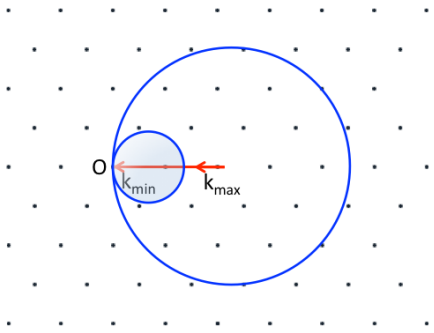

Figure 3.5: Ewald circle for a beam containing wave vectors from k_{min} to k_{max} as discussed in [1]. Figure replicated following [1].

3.1.2 Dynamical diffraction in the Laue geometry

The quantities introduced so far are now going to be used in order to describe the main aspects involved in the dynamical theory of X-ray diffraction. We can start noting that under the assumptions that the electric and magnetic fields can be expressed as sums of plane waves, that the crystal's magnetic behavior is similar to that of empty space and that the conductivity σ is zero at X-ray frequencies, we can write Maxwell's equations in the form

$$\begin{aligned} (a) \qquad & \nabla \times \mathbf{E} = -\mu_0 \frac{\partial \mathbf{H}}{\partial t} \\ (b) \quad & \nabla \times \mathbf{H} = \frac{\partial \mathbf{D}}{\partial t} = \epsilon_0 \frac{\partial (\kappa \mathbf{E})}{\partial t}. \end{aligned} \tag{3.11}$$

where $\mathbf{D} = \epsilon_0 \kappa \mathbf{E}$ is the electric displacement field [26]. If we now consider that an incoming beam of wave vector $\mathbf{K}_0$ interacts with the crystal so that a scattered wave is generated by the Fourier components of charge density described by the reciprocal lattice vector $\mathbf{H}$ ($|\mathbf{H}| = 1/d$ where d is the spacing between crystallographic planes), then we can write the scattered wave vector as

$$\mathbf{K}_H = \mathbf{K}_0 + \mathbf{H} \tag{3.12}$$

which is equivalent as to say that the momentum is conserved after the scattering event. It is worth noticing that the wave vector $\mathbf{K}$ is complex so that it can be written as

$$\mathbf{K} = \mathbf{K}^{'} - i\mathbf{K}^{''} \tag{3.13}$$

where the imaginary part describes absorption [26].

At this point one can use the plane wave approximation for both magnetic and electric fields, apply it in equations 3.11 a and b, and together with the expression provided for the dielectric constant in Eq. 3.7, it is now possible to come to a solution. The fundamental set of equations describing the field inside the crystal can be reduced to a set of two when considering the case of only one active reflection inside the crystal. They can be written in the form

$$\begin{aligned} \left[k^2\left(1-\Gamma F_0\right)-\left(\mathbf{K}_0\cdot\mathbf{K}_0\right)\right]E_0 - k^2P\Gamma\bar{F}_H E_H = 0, \\ -k^2P\Gamma F_H E_0 + \left[k^2\left(1-\Gamma F_0\right)-\left(\mathbf{K}_H\cdot\mathbf{K}_H\right)\right]E_H = 0 \end{aligned} \tag{3.14}$$

where P is the polarization factor ($P = 1$ for the σ polarization and $P = cos2\theta$ for the π one) and k is the vacuum value of the wave vector [26]. In order to solve this set of two equations it is possible to study the determinant of the associated matrix and set it to zero in order to avoid trivial solutions:

$$\begin{vmatrix} k^2\left(1-\Gamma F_0\right)-\left(\mathbf{K}_0\cdot\mathbf{K}_0\right) & -k^2P\Gamma\bar{F}_H E_H \\ -k^2P\Gamma F_H E_0 & k^2\left(1-\Gamma F_0\right)-\left(\mathbf{K}_H\cdot\mathbf{K}_H\right) \end{vmatrix} = 0 \tag{3.15}$$

where F_i are the structure factors of the corresponding reflections. It is worth noticing that the terms on the principal diagonal of matrix 3.15 represents the difference between the square of the wave vectors $\mathbf{K}_i$ inside the crystal and the square of the vacuum value k^2 corrected by the factor $(1-\Gamma F_0)$ [26]. If this difference is zero, there is no unique solution for the set of equations. For this reason, it is now possible to say that this difference is the most important parameter in this problem. In order

to better understand these terms it is possible to define two new parameters[3]

$$\begin{aligned} (a) \quad & \xi_0 = (\mathbf{K}_0 \cdot \mathbf{K}_0)^{1/2} - k\left(1 - \tfrac{1}{2}\Gamma F_0\right) \\ (b) \quad & \xi_H = (\mathbf{K}_H \cdot \mathbf{K}_H)^{1/2} - k\left(1 - \tfrac{1}{2}\Gamma F_0\right), \end{aligned} \tag{3.16}$$

where ξ_0 represents the difference between the wave vector inside the crystal $\mathbf{K}_0$ and the vacuum value corrected by the average index of refraction[4][26]. If we now rewrite Eq. 3.15 introducing these new parameters, we find

$$\xi_0 \xi_H = \frac{1}{4} k^2 P^2 \Gamma^2 F_H F_{\overline{H}} \tag{3.17}$$

which is commonly known as *dispersion surface* and where term $F_{\overline{H}}$ is the structure factor for the $\left\{\overline{hkl}\right\}$ reflection[5]. At this stage we can say that all the solution of Maxwell's equations will need to exist within this surface.

The important role of these new elements becomes clearer when considering the Ewald's sphere construction. The main difference with what described in the previous sections is that we need to take the wave vector correction into account. If in the normal case the centre of Ewald's sphere is given by the Laue point, whose distance from the origin of the reciprocal lattice is k, now we need to change the radius of our sphere so that it becomes $k - \left(1 - \frac{1}{2}\Gamma F_0\right)$ as shown in Fig. 3.6.a. This translates in a change of the sphere's centre which moves to point Q. In order to find the dispersion surface we need to draw two spheres of radius $k - \left(1 - \frac{1}{2}\Gamma F_0\right)$ centered around points H and O, as illustrated in Fig. 3.6.b, which respectively represent the {hkl} reflection and the origin of the reciprocal lattice. As expected these two spheres will meet at point Q. If we now draw the two vectors $\mathbf{K}_0$ and $\mathbf{K}_H$ departing from points O and H respectively, we can observe that they will meet the two spheres in two distinct points as shown in Fig. 3.6.b. The two points represent the difference between the wave vectors $\mathbf{K}_0$ and $\mathbf{K}_H$ and the $k - \left(1 - \frac{1}{2}\Gamma F_0\right)$ term; in other words they represent ξ_0 and ξ_H. It is now easier to visualize the dispersion surfaces as the hyperbolic sheets drawn in Fig. 3.6.c. Point A showed in Fig. 3.6.b lays on one of the hyperbolic sheets and so it is a possible solution of our problem.

[3] It is possible to write for each equation $2k\xi \equiv (\mathbf{K} \cdot \mathbf{K}) - k^2(1 - \Gamma F_0)$ and by writing the righthand side term as the product of the sum and difference one can obtain $2k\xi = 2k\left[(\mathbf{K}_0 \cdot \mathbf{K}_0)^{1/2} - k\left(1 - \frac{1}{2}\Gamma F_0\right)\right]$.

[4] This can be observed by recalling that the index of refraction is $n = \sqrt{\kappa}$.

[5] Even though we assumed that only the {hkl} reflection was operative, the presence of this structure factor is reasonable since in our system we assume that the wave with wave vector $\mathbf{K}_H$ is scattered by the backside of the atomic planes back into the $\mathbf{K}_0$ direction.

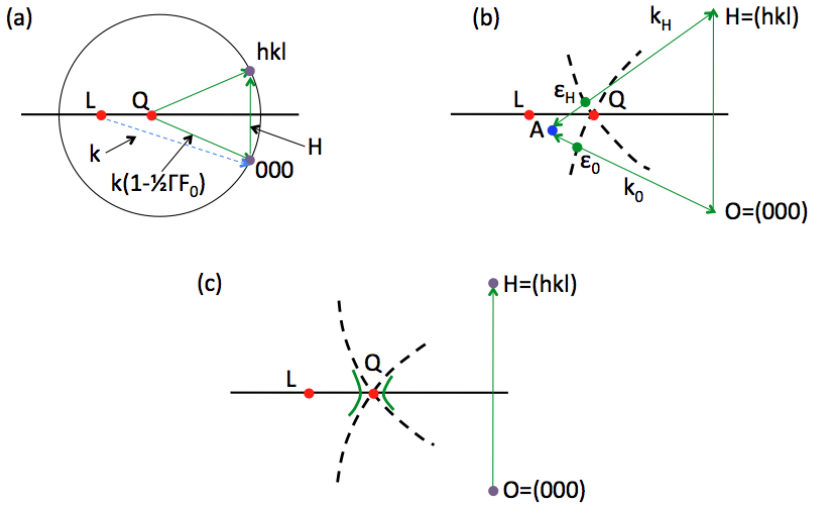

Figure 3.6: Construction of Ewald's sphere and dispersion surface retrieval. (a) If compared with the vacuum case, the Ewald's sphere has a shorter radius which takes the correction factor $\left(1-\frac{1}{2}\Gamma F_0\right)$ into account. Point O represents the origin of the reciprocal lattice, while point H is the {hkl} reflection. (b) In order to find the two factors ξ_0 and ξ_H we need to graphically apply equation 3.16 which corresponds to subtracting quantity $k\left(1-\frac{1}{2}\Gamma F_0\right)$ from vectors $\mathbf{K}_0$ and $\mathbf{K}_H$. Point A is a valid tie point from which wave vectors can be drawn to O and H to represent permitted solutions of Maxwell's equations. (c) The dispersion surfaces are hyperbolic sheets and can be defined as the locus of tie points. We can identify two branches: the one closer to the Laue point, L, is commonly called α branch, while the other one is the β branch. It is worth noticing that the polarization parameter P affects the definition of the dispersion surfaces, so that we will have a set of two branches for the σ polarization and another set for the π polarization ($P = 1$ for the σ polarization and $P = cos2\theta$ for the π one). Figure replicated following [26].

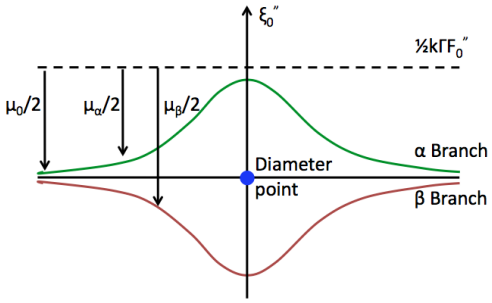

Figure 3.7: Absorption associated with each tie point. The two curves relative to the α and β branches are shown for different tie points and are derived as a difference from the upper curve set to the value $\xi_0^{''} = \frac{1}{2}k\Gamma F_0^{''}$. If confronting with equation 3.18 one can observe that the different behavior is contained within term $-K_0^{''}\cos\beta$ where $K_{0\alpha}^{''} \neq K_{0\beta}^{''}$. The diameter points are tie points that are in the Bragg condition configuration; this will be explained later in the text. Figure replicated following [26].

There are few considerations that need to be done at this point. The first is related to the geometry of the problem under examination which is in the Laue case, as shown in Fig. 3.2. The Bragg geometry will be treated later in this Chapter, however we can already anticipate that similar considerations to the ones done so far can also apply to this new case. In particular the dispersion surfaces will be oriented in a different way so to account for the fact that in this geometry the diffracted beams exits from the same face that the incident beam enters.

Another aspect worth highlighting is that the dispersion surface is a complex quantity and this can be explained by remembering that the wave vectors are also complex. For this reason one can derive the real and imaginary parts of ξ_0 in the form

$$\begin{aligned} (a) \quad & \xi_0^{'} \cong K_0^{'} - k\left(1 - \tfrac{1}{2}\Gamma F_0^{'}\right) \\ (b) \quad & \xi_0^{''} \cong -K_0^{''}\cos\beta + \tfrac{1}{2}k\Gamma F_0^{''}, \end{aligned} \tag{3.18}$$

where β is the angle between $\mathbf{K}^{'}{}_0$ and $\mathbf{K}^{''}{}_0$ [26]. This result shows us that the real and imaginary parts of ξ_0 are closely related to those of $\mathbf{K}_0$. For this reason one can conclude that the absorption process is strictly related to $\xi_0^{''}$ and that it is function of the excited tie point as shown in Fig. 3.7.

In order to better understand the meaning of tie points it is necessary to investigate what happens

when an incoming beam hits the entrance surface of an extended crystal in the Laue geometry. To start, we need to set boundary conditions for both wave vectors and fields. One can easily write the boundary conditions for the amplitudes of incident and diffracted fields as

$$\begin{aligned} (a) \quad & \mathbf{E}_0^i = \mathbf{E}_{0\alpha} + \mathbf{E}_{0\beta} \\ (b) \quad & 0 = \mathbf{E}_{H\alpha} + \mathbf{E}_{H\beta}, \end{aligned} \tag{3.19}$$

where the conservation of energy is imposed. When considering wave vectors, geometrical considerations need to be done. In the reciprocal space that we have described so far, we can imagine the incident wave vector $\mathbf{k}_0^i$ as entering the Ewald sphere somewhere, point P, and ending at the origin O of the reciprocal lattice as shown in Fig. 3.8.a. The direction followed by $\mathbf{k}_0^i$ is perpendicular to the physical entrance surface of the crystal, line SS. If point P coincides with the Laue point L it means that the incidence angle is the Bragg one, but in the case they are different it is possible to estimate the deviation from the correct Bragg angle as $\Delta\theta = LP/k$ where, as previously mentioned, k is the LO distance. It is now possible to see that when the incoming wave enters through point P, it crosses the dispersion surface in two points, A and B in the figure; these are the tie points relative to the entrance point P at the α and β branches, respectively. Starting from these tie points, we can finally draw the two vectors $\mathbf{K}_{0\alpha}$ and $\mathbf{K}_{\mathbf{0}\beta}$ which satisfy the boundary condition at the entrance surface

$$\begin{aligned} (a) \quad & \mathbf{K}_{0\alpha} = \mathbf{k}_0^i - \mathbf{PA} \\ (b) \quad & \mathbf{K}_{0\beta} = \mathbf{k}_0^i - \mathbf{PB}. \end{aligned} \tag{3.20}$$

If for simplicity we now consider the case where the perpendicular to the entrance surface SS is parallel to the line LQ, we find a difference configuration that is shown in Fig. 3.8.b. In the case the tie points on the hyperbolas are also lying on LQ, this meaning that the incident angle is exactly the Bragg angle, we find that the distance between these two points is the minimum distance between the two branches. This distance is known as diameter D of the hyperbola and for this reason the two tie points are named diameter points. An expression for D can be written in the form [26]

$$D = k\Gamma \left|P\right| \left|F_H\right| \sec\theta_B. \tag{3.21}$$

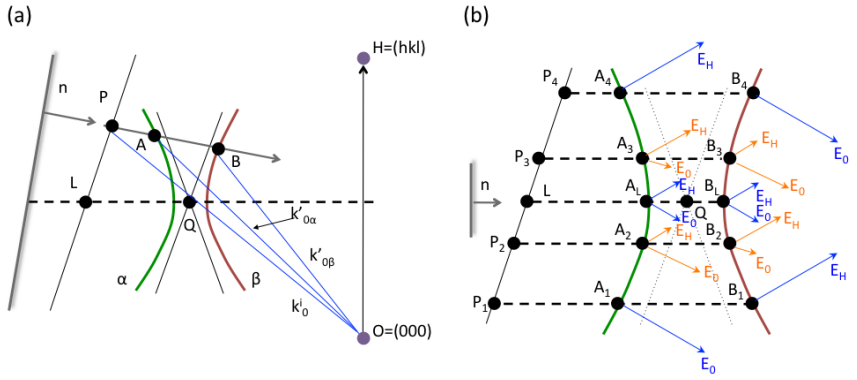

Figure 3.8: Tie points in dispersion surfaces. (a) Schematic representation of how to select a couple of tie points by using the entrance point P. Vector **PO** represents the outside incident wave vector, while **AO** and **BO** are the inside incident wave vectors. (b) Tie points for the case where the normal vector to the entrance surface SS is parallel to LQ. If the entrance point corresponds with L the Bragg condition is fully satisfied. Points $A_L$and $B_L$are called diameter points. Figure replicated following [26].

It is worth noticing that Fig. 3.8.b also shows how different tie points on the dispersion surface characterize the ratio of the field amplitudes. Following Batterman and Cole's analysis [26] one can write

$$\frac{E_0}{E_H} = -\frac{2\xi_0}{kP\Gamma F_{\overline{H}}} = -\frac{kP\Gamma F_H}{2\xi_H}, \tag{3.22}$$

which represents the ratio of the field amplitudes for each tie point. For points well off the Bragg condition, such as P_1or P_4, we see that one of the two components vanishes and this can be explained by saying that either ξ_0 or ξ_H goes to zero. In the case of diameter points the ratio of the field amplitudes is equal to one.

Another important phenomenon that takes place is the Pendellösung that is one of the consequences of the gap between the two branches of a dispersion surface. The waves emerging from each tie point travel inside the crystal with slightly different wave vectors. Thus, at some locations within the crystal they can superpose constructively or destructively. The oscillation between the two conditions is known with the name of Pendellösung effect for crystals (Pendellösung from German means solution of the pendulum). This effect can also be seen if one calculates the time average of the Poynting vector $\langle \mathbf{P} \rangle = \frac{1}{2}\mathscr{R}\left[\mathbf{E} \times \mathbf{H}\right]$ that shows how the flux of energy changes when two tie points are considered. The solution obtained by [26] is

$$\mathbf{S}_T = \mathbf{S}_\alpha + \mathbf{S}_\beta + \mathbf{S}_{\alpha\beta}, \tag{3.23}$$

where $\mathbf{S}_\alpha$ and $\mathbf{S}_\beta$ are the effective energy flows associated with a tie point on the α and β branches

and are independent from the depth inside the crystal, while $\mathbf{S}_{\alpha\beta}$ is an oscillating term that has a sinusoidal dependence. Its value is related to the difference $(\mathbf{K}_{0\alpha} - \mathbf{K}_{0\beta})$ and by looking at the geometrical construction of Fig. 3.8.a, this quantity is the distance between the coupled tie points and lays on the normal direction to the surface SS. The Pendellösung period can be written in the form

$$\mathcal{P} = \frac{1}{(\mathbf{K}_{0\alpha} - \mathbf{K}_{0\beta})} \tag{3.24}$$

and in the case of the symmetric Laue case at the Bragg angle, $1/\mathcal{P}$ is simply the diameter of the hyperbola of the dispersion surface of Eq. 3.21 [26, 27]. Following the geometrical construction of Fig. 3.9, one can notice that $\mathbf{S}_\alpha$ and $\mathbf{S}_\beta$ are perpendicular to the hyperbola at the tie points A and B. The different directions of the two vectors show that the two energy flows are directed above and below the atomic planes. In the case when L is the incidence point, the two vectors lay on line LQ this meaning that the energy flows along the atomic planes. The coupling vector $\mathbf{S}_{\alpha\beta}$ orientation changes as a function of the depth so that it cancels the two $\mathbf{S}_\alpha$ and $\mathbf{S}_\beta$ contributions in the primary beam direction $\mathbf{s}_0$ or in the diffracted beam direction $\mathbf{s}_H$ with a period $\mathcal{P}$ [6]. For this reason, if the crystal is very thin with respect to a Pendellösung period there is no diffracted beam and hence we do not observe multiple scattering effects. When the thickness of the crystal reaches one-half of P, we have that at the Bragg angle all the energy flows in the diffracted beam direction. If we move from the Bragg condition this energy gets smaller so that we can understand that with respect to the varying θ angle around the Bragg, we can find a changing integrated intensity for the diffracted beam. When the crystal gets as thick as the Pendellösung period, there is again no diffracted beam.

After multiple interactions within the crystal, the generated waves reach the exit surface. In this case we can write the boundary conditions for the fields intensities in the $\mathbf{s}_0$ and $\mathbf{s}_H$ directions

$$\begin{aligned} (a) \quad & |\mathbf{E}_H^e|^2 = |\mathbf{E}_{H\alpha}|^2 + |\mathbf{E}_{H\beta}|^2 \\ (b) \quad & |\mathbf{E}_0^e|^2 = |\mathbf{E}_{0\alpha}|^2 + |\mathbf{E}_{0\beta}|^2 , \end{aligned} \tag{3.25}$$

which mean that the fields just inside the boundary equals the fields just outside. For what concerns the boundary condition on the wave vectors, it is possible to easily conclude that in the case of Laue

[6] $\mathbf{s}_i$ are unit vectors defining the incoming and diffracted beams directions.

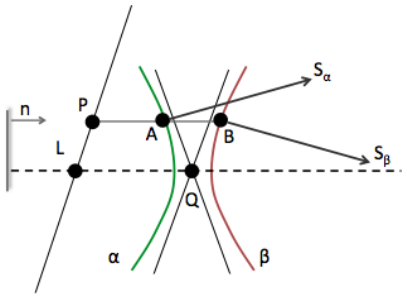

Figure 3.9: Here we show the averaged energy flow associated with tie points A and B. Pointing's vectors $\mathbf{S}_\alpha$ and $\mathbf{S}_\beta$ for the flow of each point are perpendicular to the real part of the dispersion curve at that tie point [26]. Figure replicated following [26].

diffraction where the exit surface is parallel to the entrance surface, $\mathbf{k}_0^e$ of the exit wave is the same as $\mathbf{k}_0^i$ at the entrance.

It is now possible to understand what happens in terms of diffracted and forward diffracted intensities. For the diffracted intensity given by either the α or β branches, it is common use to derive the rocking curve that can be written as a function of θ as [26]

$$\frac{I_H}{I_0} = \frac{1}{4}\frac{1}{1+\eta^2} e^{-\frac{\mu_0 t}{cos\gamma}\left(1 \mp \frac{|P|}{\sqrt{1+\eta^2}}\right)}, \tag{3.26}$$

where $\eta = (\Delta\theta sin2\theta) / |P| \Gamma \left|F_H^{'}\right|$, t is the thickness of the crystal, γ is the angle between the surface and the incoming beam, and P is the polarization state as defined above. For a given polarization state (σ or π) the shape of the rocking curve can be retrieved for different crystal thicknesses, as shown in Fig. 3.10. In the case of a thin crystal the factor $\mu_0 t$ tends to zero so that the exponential part disappears from Eq. 3.26

$$\frac{I_H}{I_0} = \frac{1}{2}\frac{1}{1+\eta^2}, \tag{3.27}$$

where we are considering the two α and β contributions together (this explains why we see $1/2$ instead of $1/4$) [26]. Similar considerations can be done for the thick crystal which corresponds to condition $\mu_0 t > 10$ where the corresponding peak will result less tall. It is worth noticing that these different behaviors for thin and thick crystals are in accordance with what predicted by considering the Pendellösung effect.

The forward diffracted or transmitted beam is of great interest since it shows the effect of the

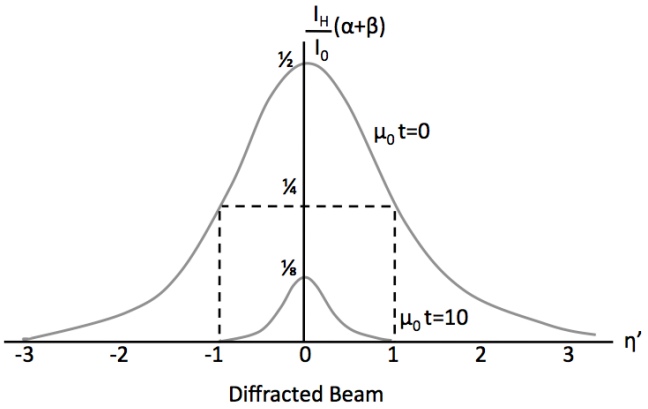

Figure 3.10: Rocking curves for crystals in the Laue geometry. The taller curve is relative to a thin crystal while the lower one describes the case of a thick crystal. Figure replicated following [26].

anomalous transmission, if the proper conditions are met. In this case we can define the intensity ratio between the exit wave in the $\mathbf{s}_0$ direction and the incoming beam as [26]

$$\frac{I_0^e}{I_0} = \frac{1}{4}\left(1 \mp \frac{\eta}{\sqrt{1+\eta^2}}\right)^2 e^{-\frac{\mu_0 t}{cos\gamma}\left(1 \mp \frac{|P|}{\sqrt{1+\eta^2}}\right)}, \tag{3.28}$$

where if we consider the thin crystal case $\mu_0 t \to 0$ we get for each polarization state

$$\frac{I_0^e}{I_0} = \frac{1}{4}\left(1 - \frac{\eta}{\sqrt{1+\eta^2}}\right)^2 + \frac{1}{4}\left(1 + \frac{\eta}{\sqrt{1+\eta^2}}\right)^2. \tag{3.29}$$

The first term represents the α branch while the other term represents the β branch. The two curves can be graphically composed as shown in Fig. 3.11.a. As expected, in the case of thin crystals the transmitted intensity has a dip for a range of angles around the Bragg angle. If we now study the case of a thick crystal we will get a different curve that shows the anomalous transmission peak as in Fig. 3.11.b.

3.1.3 Dynamical diffraction in the Bragg geometry

The dynamical diffraction regime in the Bragg case can be readily described starting from what was already discussed for the Laue geometry. In particular, the change in geometry applies to the way tie

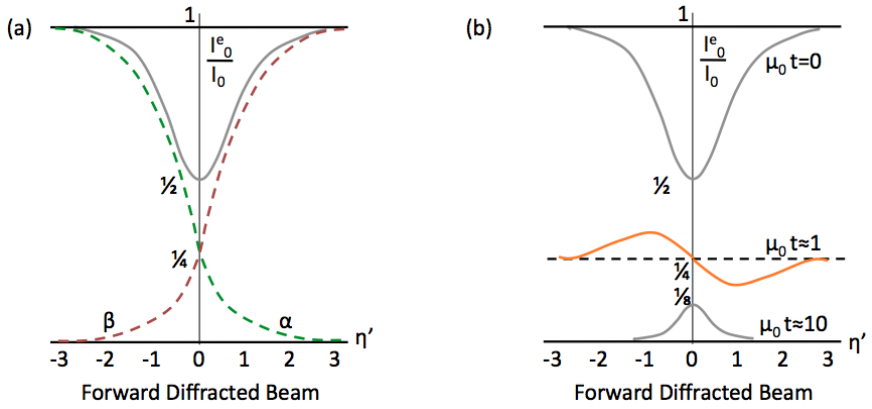

Figure 3.11: Forward diffracted beam representation. (a) The two components of the α and β branches are used to derive the forward diffracted beam integrated intensity for the case of a think crystal. (b) Curves are shown for different thicknesses. A peak results for the thick crystal, this accounting for the case of anomalous transmission. Figure replicated following [26].

points are located on the dispersion surfaces and this implies a change in the way the diffracted waves can be calculated.

In order to describe how the Laue geometry differs from the Bragg case, we can start referring to Fig. 3.12 and note that the former is described by the vertical surface, from which we see the entry point P_1. As previously discussed, the vector entering the surface from point P_1 meets the dispersion surfaces in two tie points, namely A_1 and B_1 in the figure. If we now imagine to rotate the entry surface away from the Laue geometry towards the Bragg one, we can see that the entry point will also move accordingly. In particular point P_1 will translate to P_2 which represents the boundary condition between the Laue and Bragg geometry for which we have that P_2A_2 is perpendicular to $\mathbf{k}_H$ [26]. If we now imagine to rotate the surface more so to reach the symmetric Bragg geometry, we get to point P_3, which gives as a result two tie points A_1 and B_2 on the same branch of the hyperbola. This represents a major difference between the two geometries, give that in the Laue case, tie points were always placed on both branches. Furthermore, we can note that over the angular range between the two positions P_2 and P_3 we do not have intersections with the dispersion surface, thus implying the non existence of propagating solutions. This configuration represents the "total reflection" region [26].

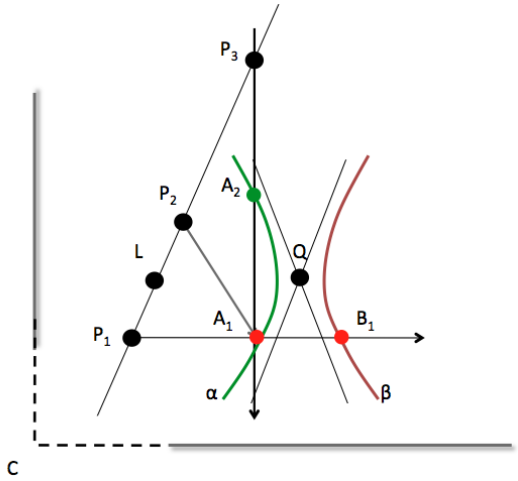

Figure 3.12: Schematic representation of the transition between the Laue and Bragg geometries as described in [26]. The left perpendicular surface represents the Laue geometry, while the Bragg case is represented by the horizontal one. The figure shows how the consequence of illuminating the crystal in the Bragg geometry is that the two tie points lie on the same branch of the dispersion surface (green and red points on the vector originating from point P_3). More details can be found in the text. Figure replicated following [26].

We can now look more closely to what happens in the Bragg case by referring to Fig. 3.13. Here we show the incident vector $\mathbf{k}_0^i$ and the diffracted exit vector $\mathbf{k}_H^e$ relative to the Bragg configuration associated to entry point P_1. As previously discussed, the two resulting tie points T_1 and T_2 lie on the α branch of the dispersion surface and here we see that both of them have an associated energy flow vector ($\mathbf{S}_1$ and $\mathbf{S}_2$). It is worth noticing that in this geometry the exit vector $\mathbf{k}_H^e$ crosses both the entry and exit surfaces and that the energy vector $\mathbf{S}_2$, associated to tie point T_2, also flows outward across the exit plane [26]. The meaning of this effect is that the flux associated to vector $\mathbf{S}_2$ does not contribute to the generation of the diffracted beam, so that tie point T_2 is not excited. This result, also discussed by Authier [27], can be summarized by saying that in the Bragg geometry case, only one tie point gives a physically meaningful contribution.

In order to retrieve the field amplitudes associated to each tie point, we can note that in this geometry we have

$$\mathbf{E_0^i} = \mathbf{E_{0j}}, \quad \mathbf{E}_H^e = \mathbf{E}_{Hj} \tag{3.30}$$

where both terms are associated to the only one excited tie point j. By referring to Eq. 3.16 and 3.22,

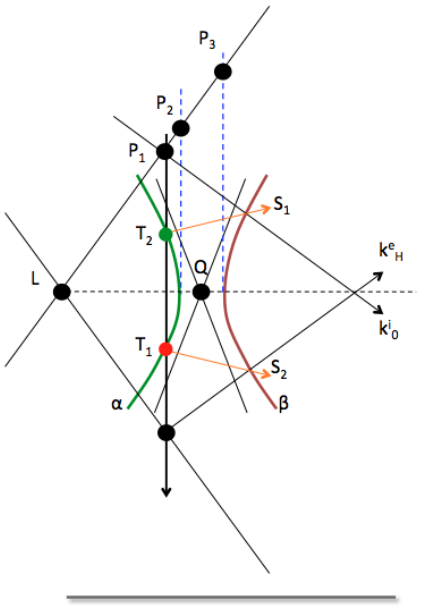

Figure 3.13: Tie points in the Bragg geometry as presented in [26]. Here we see that tie point T_2, in green, does not provide a meaningful contribution to the generation of the diffracted wave, because its associated energy flow vector $\mathbf{S}_2$ flows across the crystal's exit surface. In the region delimited between points P_2 and P_3 we do not have any vector intersecting the dispersion surfaces: under this condition we have the "total reflection" region. Figure replicated following [26].

one determine the reflection coefficient as

$$\left(\frac{\mathbf{E_H}}{\mathbf{E_0}}\right)^2 = \frac{\xi_0}{\xi_H}\frac{F_H}{F_{\bar{H}}} = |b|\left(\eta' \pm \left(\eta'^2 - 1\right)^{\frac{1}{2}}\right)^2 \frac{F_H}{F_{\bar{H}}} \tag{3.31}$$

where $\eta' = \left(b\Delta\theta sin2\theta + \frac{1}{2}\Gamma F_0(1-b)\right)/\left|P\right|\left|b\right|^{\frac{1}{2}}\Gamma\left(F_H F_{\bar{H}}\right)^{\frac{1}{2}}$ [26]. It is worth noticing that for a centrosymmetric crystal we have $F_H = F_{\bar{H}}$ so that the reflection coefficient becomes

$$\frac{\left|\mathbf{E^e_H}\right|^2}{\left|\mathbf{E^i_0}\right|^2} = \frac{\left|\mathbf{E_{Hj}}\right|^2}{\left|\mathbf{E_{0j}}\right|^2} = |b|\left|\eta' \pm \left(\eta'^2 - 1\right)^{\frac{1}{2}}\right|.^2 \tag{3.32}$$

At this stage we can discuss another relevant aspect related to the Bragg geometry: the extinction depth. In the previous section we showed that for the Laue geometry, multiple scattering events can be observed in the dynamical diffraction regime if the thickness of the crystal is larger than the Pendellösung length. In the Bragg geometry we can make similar considerations related to the extinction depth. In particular, the attenuation of the wavefield associated to the extinction effect is

related to factor $\xi_0^{''}$ as described in Eq. 3.18, which in the case of a non absorbing crystal becomes

$$\xi_0^{''} = -K_0^{''} \sin\theta, \tag{3.33}$$

given $F_0^{''} = 0$. Furthermore we can note that term ξ_0 can be written as a function of η' in the form

$$\xi_0 = \frac{1}{2} k \left|P\right| \left|b\right|^{\frac{1}{2}} \Gamma \left(F_H F_{\bar{H}}\right)^{\frac{1}{2}} \left[\eta' \pm \left(\eta'^2 + b/\left|b\right|\right)^{\frac{1}{2}}\right] \tag{3.34}$$

which becomes

$$\xi_0 = \frac{1}{2} k \left|P\right| \Gamma F_H \left[\eta' \pm \left(\eta'^2 - 1\right)^{\frac{1}{2}}\right] \tag{3.35}$$

for $b = -1$ and $F_H = F_{\bar{H}}$ [26]. Here we see that outside the total reflection range $|\eta| = 1$, ξ_0 is real, while it has real and imaginary parts for $-1 < \eta < +1$

$$\begin{array}{c} \xi_0^{'} = \frac{1}{2} k \left|P\right| \Gamma F_H \eta' \\ \xi_0 = \frac{1}{2} k \left|P\right| \Gamma F_H \left(1 - \eta'^2\right)^{\frac{1}{2}} \end{array} . \tag{3.36}$$

By combining equations 3.33 and 3.36 one can obtain the extinction factor

$$exp\left(-4\pi \mathbf{K_0^{''}} \cdot \mathbf{r}\right) = exp\left\{\left[-2\pi k \left|P\right| \Gamma F_H \left(1 - \eta^2\right)^{\frac{1}{2}} / \sin\theta\right] z\right\}, \tag{3.37}$$

where z is the crystal thickness [26]. If we now note that the average value of term $\left(1 - \eta^2\right)^{\frac{1}{2}}$ is $\frac{\pi}{4}$ in the $-1 < \eta < +1$ range, we can write the average extinction factor as

$$exp\left[-\frac{\pi^2}{2} k \left|P\right| \Gamma F_H / \sin\theta\right] z. \tag{3.38}$$

3.1.4 Dynamical diffraction and sample's thickness

After showing the main aspects of both the kinematical and dynamical theories, we can now discuss how the two relate to each other.

We started this Chapter by noting that dynamical diffraction effects become measurable when the crystal is thick enough so to allow for multiple scattering to take place. In this view, it was also stated that the kinematical theory approximation can be sufficient to describe diffraction by thin crystals.

We can now be more precise and say that the results of the dynamical theory tend asymptotically towards those of the kinematical theory when the crystal thickness is much less than a certain length, called Pendellösung distance in the Laue geometry and extinction distance in the Bragg geometry [27]. By following Authier's formulation, which is equivalent to those presented in the previous sections, we can write that this length can be written in the form

$$\Lambda_0 = \frac{\lambda\sqrt{\gamma_0\left|\gamma_H\right|}}{P\sqrt{\chi_H\chi_{\bar{H}}}} = \frac{\pi V\sqrt{\gamma_0\left|\gamma_H\right|}}{r_e\lambda P\sqrt{F_H F_{\bar{H}}}} \tag{3.39}$$

where $\gamma_0 = cos\psi_0$ and $\gamma_H = cos\psi_H$ are the cosines of the angles between the normal to the crystal surface and the incident and reflected directions, respectively [27]. This equation shows how this characteristic length is related to the wavelength and polarization of the X-ray beam as well as to the unit cell's structure factor. We can also distinguish the meaning that this distance has in the two geometries. In particular, the Bragg extinction length represents the depth inside the crystal at which the amplitude of the incoming X-ray beam is attenuated by a factor of e, while the Pendellösung oscillation period is the coordinate z in the crystal at which the incident beam is scattered, back and forth, into the diffracted one [28].

In order to define the theoretical framework in which we need to discuss the experimental results presented in this Thesis work, it is then useful to calculate the Pendellösung parameter in relation to the thickness of the samples used. In doing so it is also worth mentioning that all experiments where conducted in the Laue geometry by using $synchrotron - \sigma$ X-ray beams, thus having a polarization factor $P = 1$[7]. A summary of the calculated Pendellösung lengths is presented in Table 3.1, which shows how the thicknesses of the samples were small respect to the respective dynamical parameters. As a consequence, we could use the equations derived for the kinematical theory to define a way to obtain an approximate fitting for our experimental results, which will be discussed in Chapter 6.

In order to obtain a more detailed fitting to the experimental results, it is possible to use the equations derived in the dynamical theory, whose validity still holds in the kinematical regime. In the following Chapter we will discuss a new formulation of dynamical theory which was developed with the use of Takagi-Taupin equations [27, 29, 30], in order to illustrate the dynamical fitting which was performed by Vartanyants, Shabalin and Gorobtsov [23] for one of the Au nanocrystal dataset and

[7] As previously discussed, this is a simplified assumption which does not take intermediate polarization states into account. A more detailed definition of the polarization state would require the development of an *ad-hoc* theoretical apparatus which falls outside the scope of this Thesis work.

Sample	Thickness	Energy [KeV]	Reflection	Pendellösung length [µm]
Au	100 nm	8.7	{111}	2.07
Si	4-8 µm	7.4	{111}	17.03
InP	4 µm	9	{111}	9.34
			{220}	8.84
			{200}	13.98

Table 3.1: Table summarizing the Pendellösung lengths calculated for the samples used in the experimental work analyzed in this Thesis. The calculation was performed by following Eq. 3.39 with the use of [28].

that will be presented in Chapter 6.

3.2 Different approaches to solve the phase problem

Following Patterson's first attempt, as briefly discussed in Chapter 1, many authors successfully developed different approaches to solve the phase problem. After introducing the main concepts of kinematical and dynamical diffraction in the previous sections, we can now present a selection of these milestones which allowed to experimentally measure the structure factor and its phase.

3.2.1 Structure factors measurements through the analysis of Pendellösung fringes

In order to experimentally determine the X-ray structure factor of crystals many authors used the Pendellösung method [3, 31, 32, 33, 34, 35]. This method considers the incident X-ray beam as a spherical wave and uses the dynamical theory of diffraction in order to take into account the energy exchange between diffracted and transmitted waves [3]. In particular the theoretical formulation of the method describes how the energy is transferred back and forth between the two beams, as the the wave fields travel through the crystal. The oscillation of the wave fields of both beams is characterized by a spatial periodicity within the crystal which acts as an intensity modulation.

In Kato and Lang's experiment [3], an X-ray beam was used to illuminate a wedge-shaped crystal in the Laue geometry, so that the emerging plane waves could have different wave vectors. As a consequence interference fringes could be measured outside the crystal. A schematic representation of

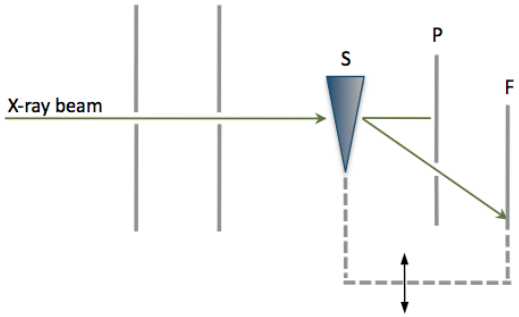

Figure 3.14: Kato and Lang's experimental setup as described in [36]. A wedge-shaped crystal (S) is illuminated by an X-ray beam, collimated through a set of slits. Downstream from the sample an additional slit placed at P only allows the diffracted beam to reach the recording film F. In this arrangement, specimen and film can be moved back and forth together (see arrow in the figure), so to record on the same film a diffraction topograph from a large area of the crystal.

the setup is provided in Fig. 3.14.

In this configuration, the sample was moved with respect to the beam so to illuminate the crystalline specimen at different thicknesses, while always recording the diffraction pattern on the same film, downstream from the sample. The result of the measurement were contrast images showing fringes which could be explained by considering the extinction phenomenon taking place when the thickness of the sample being illuminated was close to the Pendellösung length.

In order to give a theoretical description to the interference fringes, the authors defined the wave vectors of the plane waves emerging from the crystal following [36] as

$$\begin{aligned}\mathbf{K_g^{(1)}} &= \mathbf{K}_0 + 2\pi\mathbf{g} + A_0\{(y-(y^2+1)^{\frac{1}{2}})\upsilon_e/\cos\theta_g + (y+(y^2+1)^{\frac{1}{2}})\upsilon_a/\cos\phi_g\} \\ \mathbf{K_g^{(2)}} &= \mathbf{K}_0 + 2\pi\mathbf{g} + A_0\{(y+(y^2+1)^{\frac{1}{2}})\upsilon_e/\cos\theta_g + (y-(y^2+1)^{\frac{1}{2}})\upsilon_a/\cos\phi_g\}\end{aligned} \tag{3.40}$$

where A_0 is linked to the structure factor by

$$A_0 = \pi k_0 K \left|\psi_H^{'}\right| (\cos\theta_g/\cos\theta_0)^{\frac{1}{2}} \tag{3.41}$$

where $\psi_H^{'}$ is the H-th order Fourier coefficient of the polarizability, hence proportional to the structure factor [3]. Other parameters in the formula are y, which shows the angular deviation of the incident beam from the Bragg angle and angles θ_g and ϕ_g, representing the distance between the diffracted beam

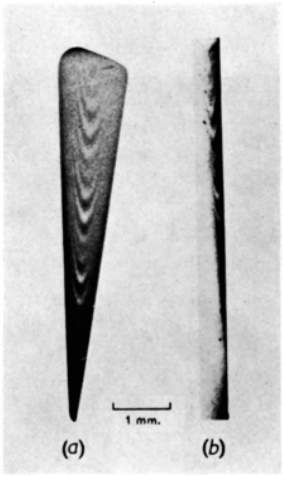

Figure 3.15: Experimental results from Kato and Lang's section experiment for the Silicon 440 reflection. Diffracted (a) and primary-beam (b) patterns. The figures show the complementarity of structure between diffracted and primary transmitted beams: the light fringes in (a) correspond to the dark fringes in (b). Figure extracted from Kato and Lang's original article [3] and reproduced with permission of the International Union of Crystallography.

and the unit vectors υ_e (normal to the incident surface) and υ_a (normal to the exit surface), respectively. Being the difference between the two vectors $\Delta\mathbf{K}$ normal to $\mathbf{K_g^{(1)}}$ and $\mathbf{K_g^{(2)}}$, the authors concluded that as they traced the interference pattern away from the sample, the fringes moved parallel to the direction of the wave vectors. In such configuration, a recording film perpendicular to the reflected beam could collect the fringes whose spacings were given by

$$\begin{aligned} \Lambda &= 2\pi/\left|\Delta\mathbf{K}\right| \\ \Lambda &= \lambda/\{K\left|\psi_H^{'}\right|((1+y^2)\cos\theta_g/\cos\theta_0)^{\frac{1}{2}}\Phi\} \end{aligned} \tag{3.42}$$

where Φ is a geometric factor and y is a parameter. In this way Kato and Lang showed how the fringe separation was related to the X-ray wavelength, to geometrical factors and to the structure of the sample through the factor $\left|\psi_H^{'}\right|$. A picture showing the experimental results obtained by Kato and Lang can be found in Fig. 3.15.

Other experiments were conducted by using this approach in the following years. In particular Hart and Milne [4] used the Pendellösung fringe method to measure the atomic scattering factor. In their formulation the authors calculated, in the Laue case, the minima of the intensity field of the Bragg reflected wave and linked those values to the positions of the fringes, for different orders.

The authors started from Kato and Lang's description, in the symmetric Laue case, of the intensity field of the Bragg reflected waves in the spherical wave case which can be written as

$$I_H = A\pi^2\Delta_0^{-2} cosec^2\theta\{J_0(\pi\varrho\Delta_0^{-1})\}^2 \tag{3.43}$$

for a section pattern, as presented in [3]. In the formula A represents a constant, θ is the Bragg angle, J_0 is the zero order Bessel function and ϱ is the distance measured inside the crystal along the net plane from the X-ray entrance surface [4]. In order to highlight the dependence of Eq. 3.43 to the structure factor, quantity Δ_0 can be written as

$$\Delta_{0=\frac{\lambda\cos\theta}{P(\chi_H\bar{\chi_H})^{\frac{1}{2}}}} \tag{3.44}$$

where P[8] is the polarization and where quantity

$$(\chi_H\bar{\chi_H})^{\frac{1}{2}} = \frac{r_e\lambda^2|F_H|}{\pi V}, \tag{3.45}$$

shows dependency on the classical electron radius r_e and on the F_H structure factor for the h-order Bragg reflection from the unit cell of volume V [4]. In order to only consider fringes not too close to the entrance surface of the crystal, the authors developed the intensity field formula further by using the asymptotic form of the Bessel function so to obtain

$$I_H = 2\pi A\Delta_0^{-1}\varrho^{-1} cosec^2\theta(\pi\varrho\Delta_0^{-1} + \frac{\pi}{4}). \tag{3.46}$$

At this stage the authors modified the intensity equation so to take into account the fact that the incident beam that they used to illuminate the sample was essentially unpolarized. In order to do so they included both principal polarization components, so that the intensity filed equation could be written as

$$I_H = A'\left\{\sin^2\pi\left(\frac{\varrho}{\Delta_0^{\sigma}} + \frac{1}{4}\right) + |\cos 2\theta|\sin^2\pi\left(\frac{\varrho}{\Delta_0^{\pi}} + \frac{1}{4}\right)\right\} \tag{3.47}$$

where Δ_0^{σ} and Δ_0^{π} are the values obtained for $P = 1$ and $P = |\cos 2\theta|$, respectively. Hart and Milne then showed that the minima of I_H occurred near the fringe orders defined as in the scheme

[8]The polarization factor was further discussed in Chapter 2, where a complete definition was provided in Eq. 2.10.

$$0 < \bar{n}_0 < \tfrac{1}{2}N \qquad minima \quad near \quad \bar{n}_0 = l - \tfrac{1}{4}$$

$$\tfrac{1}{2}(2K-1)N < \bar{n}_0 < \tfrac{1}{2}(2K+1)N \quad \begin{cases} minima & near & \bar{n}_0 = l + \tfrac{1}{4} \\ for & k & odd \\ minima & near & \bar{n}_0 = l - \tfrac{1}{4} \\ for & k & even \end{cases} , \tag{3.48}$$

where l is an integer and $\bar{n}_0$ is the fringe order which is related to the crystal thickness by

$$t = n_0^\sigma \Delta_0^\sigma = n_0^\pi \Delta_0^\pi = \bar{n}_0 \bar{\Delta}_0 \tag{3.49}$$

where $\bar{\Delta}_0$ represents the polarization-averaged value of Δ_0 [4].

Their experiment was performed by using a ribbon beam of X-rays to illuminated a wedge-shaped crystal, mounted on a slide which allowed to obtain section patterns at known positions in the specimen. Pendellösung fringes were then photographed on nuclear emulsion plates and position patterns were obtained at each observation position with Mo Kα1 and Ag Kα1 radiations. Following the X-ray experiment, the wedges were cut at the exact places where section patterns were recorded in sections parallel to the Bragg planes. At that point the crystal thickness was also directly measured with a microscope. The spacing of the fringes together with the measured crystal thickness, allowed the authors to successfully determine the atomic scattering factor with an internal consistency of better than 0.1% [4].

3.2.2 Phase problem solution with the use of X-ray standing wave fields

Another approach was presented by Bedzyk and Materlik [5], who gave evidence to the relationship between the phase of the structure factor to that of the X-ray standing wave field.

In their paper the authors started noting that in the dynamical diffraction regime, when an X-ray plane wave is diffracted by a thick single crystal, a standing-wave field is established inside the crystal itself as a result of the interference between the incident and diffracted plane waves. According to the dynamical theory of diffraction, the standing-wave pattern[9] exists inside the crystal and is characterized by nodal planes parallel to the sample's atomic planes [26]. As observed by the authors

[9]The standing-wave pattern was described at the beginning of this Chapter.

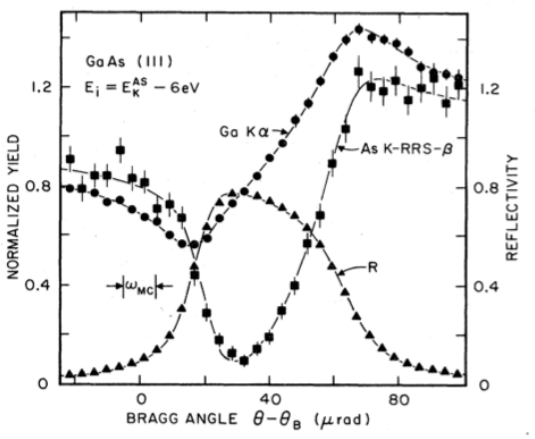

Figure 3.16: Experimental data fittings for the Ga K α fluorescence, As K-RRS-β and GaAs {111} reflectivity as function of angle θ at $E_i = E_k^{As} - 6eV$. The measured phase from the As K-RRS-β yield was $\beta_{111} = 2\pi(-0.090 \pm 0.003)$, while for the Ga K α fluorescence $\beta_{111} = 2\pi(-0.093 \pm 0.002)$, both in accordance with the predicted values. Figure extracted from [5] and reproduced with permission of the American Physical Society.

[5], in the reflection geometry there is a relationship between the phase of the diffraction planes and that of the standing wave-field; in particular they observed that the relative phase between the two could be finely tuned by adjusting the incidence angle in proximity of the Bragg condition. The authors also noted that for incident angles well below the Bragg reflection, the standing-wave field was in counter phase respect to the diffraction planes, while for angles well above the Bragg condition there was a correspondence between the field antinodes and the Bragg diffraction planes. Furthermore, the relative movement between the standing wave field and the diffraction planes could be observed by monitoring the fluorescence from atoms occupying positions within the periodicity, as also noted by Batterman in his previous work on Ge fluorescence [37]. Following the X-ray standing wave technique the authors showed that the phase of the structure factor could be measured for any thick perfect crystal by recording the fluorescence radiation emerging from the scattering element. In particular they experimentally determined the (111) and (200) structure factor phases for GaAs.

Starting from the description of the structure factor as a superposition of the coherent x-ray scattered waves emerging from the N atoms contained in the lattice unit cell

$$\begin{aligned} F_H &= |F_H|\, exp\,(i\beta_H) \\ F_H &= \sum_{n=1}^{N} \left[f_n^0(\mathbf{H}) + f_n^{'}(\mathbf{H}) + i f_n^{''}(\mathbf{H}) \right] s_n(\mathbf{H}) D_n(\mathbf{H}) \end{aligned} \quad , \tag{3.50}$$

where $s_n(\mathbf{H}) = exp(2\pi i \mathbf{H} \cdot \mathbf{r_n})$ is a geometrical phase factor and $D_n(\mathbf{H})$ is the Debye-Waller temperature factor for the n-th atoms, the authors defined the GaAs structure factors [5] as

$$\begin{aligned} (a) \qquad & \beta_{\pm(111)} = \mp \arctan\left[\frac{f^0_{As}(\mathbf{H}) + f'_{As}(\mathbf{H}) \mp f''_{Ga}(\mathbf{H})}{f^0_{Ga}(\mathbf{H}) + f'_{Ga}(\mathbf{H}) \pm f''_{As}(\mathbf{H})}\right] \\ (b) \quad & \beta_{\pm(200)} = \mp \arctan\left[\frac{f''_{Ga}(\mathbf{H}) - f''_{As}(\mathbf{H})}{f^0_{Ga}(\mathbf{H}) + f'_{Ga}(\mathbf{H}) - f^0_{As}(\mathbf{H}) - f'_{As}(\mathbf{H})}\right]. \end{aligned} \tag{3.51}$$

In the above equations $f^0_n(\mathbf{H})$ is the atomic form factor which accounts for the elastic scattering in the "free electron approximation", while $f'_n(\mathbf{H})$ and $f''_n(\mathbf{H})$ are anomalous dispersion parameters which describe the absorption processes leading to incoherent scattering [5].

The experiment was conducted by varying the incident photon energy which proved to affect the value of the structure factor phase near the absorption edges. The authors showed that changes in the $\beta_{\mathbf{H}}$ factor were determined by the atoms positions within the unit cell. By combining the phase measurement with the measured change in absorption, it was possible to determine the $f'(\mathbf{H})$ and $f''(\mathbf{H})$ parameters which allowed to solve the phase problem by determining $\beta_{\mathbf{H}}$. A figure summarizing the experimental fittings from Bedzyk and Materlik's measurements is shown in Fig. 3.16.

3.2.3 Phase shift investigation in X-ray forward diffraction

In order to solve the phase problem, Hirano and Momose [6] proposed another method which was based on the use of an X-ray Bonse-Hart interferometer, as shown in Fig. 3.17. In their experiment they investigated the structure of a diamond crystal slab by looking at the phase shift of the diffracted and forward diffracted waves and verified the consistency of their results with the dynamical theory of X-ray diffraction.

The authors described the phase shift of forward diffracted X-rays in the case of perfect crystals by following the dynamical theory. They described the effect saying that the forward scattered X-rays produced in the transmission direction acquire a phase shift while traveling inside the crystal. This can be explained by noting that this phase is related to the refractive index which is complex and can be written as

$$n = 1 - \alpha = 1 - \frac{\lambda^2 r_e}{2\pi V_c} F_0 \tag{3.52}$$

where r_e is the electron radius, V_c is the volume of the unit cell and F_0 is the crystal structure factor in the $\{000\}$ reflection [6]. When the incident beam reaches the Bragg condition, multiple scattering

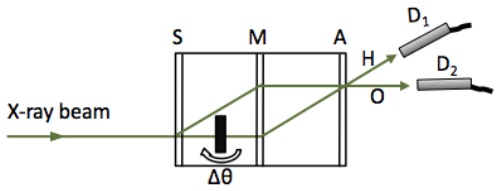

Figure 3.17: Schematic representation of Hirano and Momose's experimental setup. The incident monochromatic X-ray beam travels through a Bonse-Hart LLL-interferometer (triple-Laue case) composed by three parallel wafers which act as X-rays half mirrors and which are called beam splitter "S", mirror "M" and analyzer "A". When the X-ray beam incident upon the S mirror satisfies the Bragg condition, the splitter creates two coherent beams which travel in the interferometer and recombine at the A wafer level, producing two outgoing beams, O and H, traveling in the forward and reflected directions, respectively. Two detectors are then used to measure the resulting intensities. It is worth noting that the sample is inserted in the interferometer on a moving support which allows its rotation. Figure reproduced following [6].

takes place in the crystal and the refractive index formulation is corrected, according to the dynamical theory, as

$$\Delta n = -\frac{r_e^2 F_H F_{\overline{H}}}{4\pi^2 V_c^2} \frac{\lambda^4 P^2}{\Delta\theta \sin(2\theta_B)} \tag{3.53}$$

which shows dependency on the Bragg angle θ_B, on the offset angle from the diffraction condition $\Delta\theta$, on the polarization factor P and on the structure factors F_h and $F_{\overline{h}}$ of the hkl and $\overline{hkl}$ reflections, respectively [6]. The authors also noted that, as a consequence to Eq. 3.53, the phase shift caused by a diffraction correction could be written as

$$\begin{gathered} \delta = 2\pi Re(\Delta n) t/\lambda \\ \delta = -\frac{\pi}{2} \left[\frac{r_e^2 F_H F_{\overline{H}}}{4\pi^2 V_c^2} \frac{\lambda^3 P^2}{\Delta\theta \sin(2\theta_B)} \right] t \end{gathered} \tag{3.54}$$

where we see the dependency from the real part of the refractive index and from the thickness t of the crystal.

In the experiment, a diamond crystal slab was mounted on a rotating support and inserted in a triple Laue-case X-ray interferometer, which was placed at an angle that allowed the generation of two

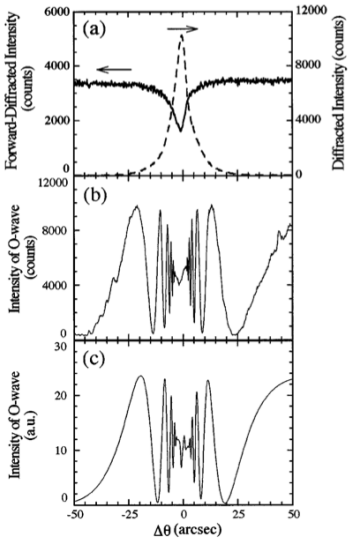

Figure 3.18: (a) Rocking curve measured on the diamond sample without the use of the LLL interferometer. (b) Measured intensity of the O-beam. (c) Theoretical curve for the O-beam plotted following Eq. 3.56. Figure extracted from [6] and reproduced with permission of the American Physical Society.

coherent internal beams. Inside the interferometer only one beam crossed the sample, while the other acted as a reference beam. When reaching the interferometer exit surface A, the two internal beams recombined to generate two outgoing beams, O and H, whose intensities where measured with the use of external detectors. The authors noted that while the reference beam passed through air ($n \approx 1$), the object beam was affected by the sample's refractive index ($n \approx 1 - \alpha + \Delta n(\Delta\theta)$) so that the phase difference between the two could be written as

$$\psi(\Delta\theta) = \frac{2\pi Re\left[-\alpha + \Delta n(\Delta\theta)\right] t}{\lambda}. \tag{3.55}$$

By neglecting the X-ray absorption by air, the O-beam intensity could be expressed in the form

$$I(\Delta\theta) = 1 + T(\Delta\theta) + 2\sqrt{T(\Delta\theta)}\cos\left[\psi(\Delta\theta)\right] \tag{3.56}$$

where $T(\Delta\theta)$ is the transmittance of X-rays at the diamond crystal and which shows that the phase dependent term $\cos\left[\psi(\Delta\theta)\right]$ can be obtained by measuring the $T(\Delta\theta)$ and $I(\Delta\theta)$ [6]. Fig. 3.18 shows the experimental results compared to the theoretical curves.

Chapter 4

Quasi-kinematical diffraction approximation

We concluded the previous Chapter with the definition of the dynamical parameter which allows to see the limit under which the dynamical theory tends asymptotically to the kinematical one [27]. This parameter, defined in Eq. 3.39, represents the Pendellösung and extinction lengths in the Laue and Bragg geometries, respectively. We then observed that the samples used to conduct the experiments discussed in this Thesis were all thin if compared with their respective Pendellösung lengths. For this reason we could argue that the experimental results could be discussed, in a first approximation, with the use of the kinematical equations developed in Chapter 2, which were written by taking the scattering by multiple crystallographic planes into account. However, the need for a rigorous theory which could be applied to this specific regime, brought us to collaborate with Vartanyants, Shabalin and Gorobtsov [23] who performed a second fitting based on the use of dynamical equations for one of our experimental datasets. The outcome of this collaboration will be discussed in Chapter 6, but here we present the theory at the basis of this result by following the steps illustrated by Gorobtsov and Vartanyants in their recently published paper [2]. In addition to that, we will further deepen this theoretical apparatus by discussing an innovative *quasi-kinematical* approximation, also presented in [2], which represents a further development respect to what discussed in this Thesis. In particular the authors decided to refine the dynamical equations that were used to fit our experimental results so to

make them fully consistent with the fact that our experiments where performed in a *quasi-kinematical* regime, where the sample's thicknesses were small respect to their respective Pendellösung lengths. At the end of this Chapter we will compare the simulated curves obtained with this new theory to those calculated in the fully dynamical limit, in order to highlight the consistency between the two techniques.

In order to define the theoretical framework at the basis of the equations used in [2], the first section of this Chapter will provide the Takagi-Taupin (TT) [29, 30] formulation of dynamical diffraction as discussed in [38]. The following section will then explore how the dynamical theory can be modified with the use TT equations, so to then define the theoretical apparatus which could be used to implement the fitting of the results obtained for the Au nanocrystals measurements, as it will be later discussed in Chapter 6. In the end, we will also discuss the recently developed *quasi-kinematical* approximation, also presented in [2].

4.1 Preliminary considerations

Before deriving the main equations which can be used to describe the diffraction theory in both the dynamical and quasi-kinematical limit, it is worth highlighting how the structure of the crystal affects the phase of the diffracted beam. In particular, in Chapter 2 we already discussed the phase shift which applies to an incident wave passing through a slab by noting how this depends on the material's refractive index n. In this section we want to be more precise and show how this phase shift changes for non periodic and periodic media and how this quantity can be related to the structure factor.

4.1.1 Phase shift in non periodic media

For materials with a non periodic structure we can write the refractive index for is X-rays as

$$n = \sqrt{1 + \chi_0} \simeq 1 + \frac{\chi_0}{2} \tag{4.1}$$

where χ_0, which represents the zeroth Fourier component of the susceptibility $\chi(\mathbf{r}, \omega)$, is assumed to be $\chi_0 \ll 1$. This quantity can be written in the form $\chi_0 = -r_e \lambda^2 \rho / \pi$ as discussed in Section 3.1.1 following [1, 2]. By considering the refractive index formulation that we just defined, we can write the

phase shift associated to a wave passing through a slab of a non periodic medium as

$$\begin{aligned} E_{out}(d) &= E_{in}(z=0)e^{i\phi(d)} \\ \phi(d) &= \frac{nkd}{\gamma} = \frac{\left(1+\frac{\chi_0}{2}\right)kd}{\gamma}, \end{aligned} \tag{4.2}$$

where d is the medium thickness and γ is the direction cosine $\gamma = cos(\mathbf{n}\cdot\mathbf{k})$, where $\mathbf{n}$ s the vector normal to the entrance surface, as shown in Fig. 4.1 [2].

4.1.2 Phase shift in periodic media

The phase shift for X-rays passing through a periodic medium is different from the above under a specific condition. In particular we note that when the X-ray beam's incident angles are close to the Bragg angle, an additional correction δ_n is applied to the refractive index [2, 27]. This factor can be written, for angles far from the Bragg condition $|\Delta\theta| \gg |\chi_H| / sin2\theta_B$, in the form

$$\delta_n = \frac{P^2\chi_H\chi_{\bar{H}}}{4\gamma_0\left(\Delta\theta - \theta_{ref}\right)sin\theta_B} \tag{4.3}$$

where θ_{ref} is the angular correction due to refraction and which shows a dependency on the rocking angle $\Delta\theta$ as well as on the structure factor, given that the susceptibility can be expressed as [2]

$$\chi_H = -\Gamma F_H, \quad \chi_{\bar{H}} = -\Gamma F_{\bar{H}} \tag{4.4}$$

where $\Gamma = r_e\lambda^2/\pi V$ as discussed in Chapter 3. It is worth highlighting the formulation of this refractive index correction factor holds in both the Bragg and Laue reflection geometries.

By noting that the phase shift for non periodic media is proportional to the medium refractive index, we can apply δ_n to Eq.4.2 and see that the dynamical phase correction given by the interaction between the transmitted and diffracted waves is proportional to the crystal thickness and to product of the structure factors $F_H F_{\bar{H}}$, while it is inversely proportional to the deviation from the Bragg angle [2]. As we noted above, Eq. 4.3 is valid for angles far from the Bragg condition, so the formulas obtained so far cannot be used to describe the experimental results presented in this Thesis, which were obtained for a range of angles close to θ_B. In order to propose a solution to this problem, Gorobtsov and Vartanyants developed a *quasi-kinematical* approximation theory, starting from the dynamical

diffraction theory formulated with the use of the Takagi-Taupin equations [2].

4.2 Takagi-Taupin equations

In defining the Takagi-Taupin equations, we can start referring to Maxwell's equation and note that one can write the wave propagation equation for the electric field $\mathbf{E}(\mathbf{r},\omega)$ inside a crystal in the form

$$\left(\Delta + k^2\right)\mathbf{E}(\mathbf{r},\omega) - grad \cdot div\mathbf{E}(\mathbf{r},\omega) = -k^2\frac{4\pi i}{\omega}\mathbf{j}\left(\mathbf{r},\omega\right) \tag{4.5}$$

where $\mathbf{j}\left(\mathbf{r},\omega\right)$ is the current density introduced by the electromagnetic field, as discussed in [38]. This quantity can be defined as a linear function of the electric field

$$\mathbf{j_i}\left(\mathbf{r},\omega\right) = \int \mathbf{dr'}\sigma_{ik}\left(\mathbf{r},\mathbf{r'},\omega\right)E_k\left(\mathbf{r'},\omega\right) \tag{4.6}$$

which is written in accordance with the linear electromagnetic wave theory, and where $\sigma_{ik}\left(\mathbf{r},\mathbf{r'},\omega\right)$ is the factor representing the non-local tensor of the conductivity of the crystal, whose main contribution derives from the elastic Thompson scattering [38]. The tensor of the conductivity can be further developed as

$$\sigma_{ik}\left(\mathbf{r},\mathbf{r'},\omega\right)E_k = \sigma\left(\mathbf{r},\omega\right)\delta_{ik}\delta\left(\mathbf{r}-\mathbf{r'}\right) \tag{4.7}$$

where δ_{ik} is the Kronecker symbol defined as

$$\delta_{ik} = \begin{cases} 0 & if \quad i \neq j \\ 1 & if \quad i = j \end{cases} \tag{4.8}$$

as also discussed in [38]. We can now use this quantity to write the crystal susceptibility as $\chi(\mathbf{r},\omega) = (4\pi i/\omega)\,\sigma\left(\mathbf{r},\omega\right)$ and use it together with Eq. 4.7 so to rewrite the right-hand side of the wave propagation equation defined in Eq. 4.5 as

$$\frac{4\pi i}{\omega}\mathbf{j}\left(\mathbf{r},\omega\right) = \chi\left(\mathbf{r},\omega\right)\mathbf{E}\left(\mathbf{r},\omega\right), \tag{4.9}$$

where we note that in the case of a perfect ideal crystal, χ is a periodic function which can be written with the use of a Fourier expansion in the form

$$\chi^{(id)}(\mathbf{r}) = \sum_h \chi_h^{(id)} e^{(i\mathbf{hr})} \tag{4.10}$$

where we are neglecting the ω dependence and where $\mathbf{h} = 2\pi\mathbf{H}$, where $\mathbf{H}$ is the reciprocal lattice vector [38].

At this stage one can consider the case of a weakly deformed crystal by introducing two functions: the deformation vector $\mathbf{u}(\mathbf{r})$, which accounts for the atomic displacement in the crystal respect to the perfect lattice structure, and the Debye-Waller correction $e^{-W(\mathbf{r})}$ which describes the X-ray attenuation consequent to the atoms thermal motion [38]. In this context, the crystal susceptibility can be written as

$$\chi(\mathbf{r}) = \chi^{(id)}(\mathbf{r} - \mathbf{u}(\mathbf{r})) \tag{4.11}$$

where we are considering the case of relatively small displacements, and its Fourier components become

$$\chi_H(\mathbf{r}) = \chi_H^{(id)} e^{-i\mathbf{Hu(r)}} e^{-W(\mathbf{r})} \tag{4.12}$$

which also include the Debye-Waller correction factor [38]. With the use of Eq. 4.12 we can now write the solution of Eq. 4.5 in the form

$$\mathbf{E}(\mathbf{r}) = \sum_h E_h(\mathbf{r}) e^{i\mathbf{k_H r}} \tag{4.13}$$

where ω is still being neglected and where $\mathbf{k_H}$ represents the diffracted wavevector, which can be related to the incident wavevector by $\mathbf{k_H} = \mathbf{k_0} + \mathbf{H}$ [38]. In order to define the amplitudes $\mathbf{E_H}(\mathbf{r})$, we can note that in case of small crystal deformations, where relative displacements $\mathbf{u^i}(\mathbf{r})$ are small respect to interatomic distances

$$\left| \frac{\partial u^i}{\partial x_k} \right| \ll 1, \tag{4.14}$$

they vary on length scales of the order of the extinction/Pendellösung distance Λ_0, which are much longer respect to the X-rays wavelengths [38]. In this configuration we can write

$$\frac{\partial}{\partial s_H} \mathbf{E_H}(\mathbf{r}) = \frac{ik}{2} \sum_{H'} \left[\chi_{HH'}(\mathbf{r}) - \alpha_{H'} \delta_{HH'} \right] \mathbf{E}_{H'}(\mathbf{r}) \tag{4.15}$$

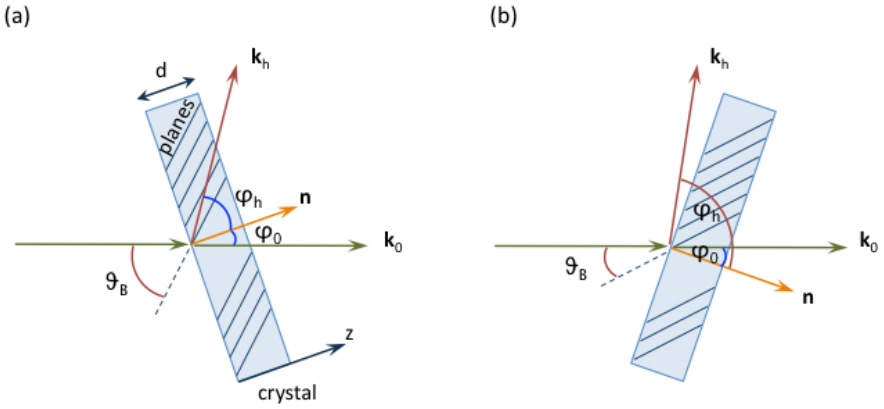

Figure 4.1: A crystal of thickness d is represented in the Laue (a) and Bragg (b) geometries, as described in [2].

which includes quantities

$$\begin{aligned} \alpha_H &= \tfrac{\mathbf{k_H^2}-\mathbf{k_0^2}}{k_0^2} \\ \tfrac{\partial}{\partial s_H} &= (s_H \bigtriangledown) \\ s_H &= \tfrac{\mathbf{k_H}}{|\mathbf{k_H}|} \\ \chi_{HH'}(\mathbf{r}) &= \chi^{(id)}_{H-H'} e^{-i(\mathbf{H}-\mathbf{H'})\mathbf{u}(\mathbf{r})} e^{-W(\mathbf{r})} \end{aligned} \tag{4.16}$$

and where the second derivatives of $\mathbf{E}_H(\mathbf{r})$ are neglected. The amplitudes defined in Eq. 4.15 represent the Takagi-Taupin equations in weakly-deformed crystals [38, 29, 30], which also define the wave field in a perfect crystal for $\mathbf{u}(\mathbf{r}) = 0$ and $e^{-W(\mathbf{r})} \equiv 1$.

We can now write the total wave field in a crystal by using the two-wave approximation as

$$\mathbf{E}(\mathbf{r}) = \sum_s \left[\epsilon_{0s}\mathbf{E}_{0s}(z)e^{i\mathbf{k}_0\mathbf{r}} + \epsilon_{Hs}\mathbf{E}_{Hs}(z)e^{i\mathbf{k}_H\mathbf{r}}\right], \tag{4.17}$$

where s is the polarization index and ϵ_{0s} and ϵ_{Hs} represent the polarization unit vectors [38].

At this stage the TT equations can be written for the incident and diffracted wave-fields as

$$\begin{array}{c} \frac{dE_{0s}(x)}{dz} = \frac{i\pi}{\lambda\gamma_0}\left[\chi_{00}E_{0s}(z) + \chi_{0H}Pe^{i\phi(z)-W(z)}E_{Hs}(z)\right] \\ \frac{dE_{Hs}(z)}{dz} = \frac{i\pi}{\lambda\gamma_H}\left[\left(\chi_{HH}-\alpha\right)E_{Hs}(z) + \chi_{H0}Pe^{i\phi(z)-W(z)}E_{0s}(z)\right] \end{array}, \tag{4.18}$$

with

$$\begin{array}{c} \phi(z) = \mathbf{H}\cdot\mathbf{u}(z) \\ \gamma_{0,h} = \cos(\mathbf{n}\cdot\mathbf{k}_{0,H}) \end{array} \tag{4.19}$$

where $\phi(z)$ is defined as also shown in [39] and where $\mathbf{n}$ is the vector normal to the crystal entrance surface, as shown in Fig. 4.1, and where we are considering a fixed polarization s [38, 2]. It is worth highlighting that because in the X-ray wavelengths regime the crystal susceptibility is small, in Eq. 4.18 we are considering that only the waves that satisfy the Bragg condition $|\alpha_H| \sim |\chi_H|$ give a valid contribution. The parameter α was used in the equation to account for the deviation from the Bragg condition $\alpha = \left(k_H^2 - k_0^2\right)/k_0^2 \approx -2\sin 2\theta_B \Delta\theta$ [2]. Furthermore, in Eq. 4.18 we are also assuming that the displacement and thermal factors only depend on the penetration spatial coordinate z inside the crystal, while dependency on the other two dimensions along the crystal are neglected [38]. In addition to that we note that the equation also includes the polarization factor P, which was previously defined in Eq. 2.10.

In the case were we are only considering the photoelectric scattering in the dipole approximation and the strongest elastic scattering, the crystal susceptibilities in Eq.4.18 are complex and can be written as $\chi_{00} = \chi_{HH} = \chi_0$, $\chi_{0H} = \chi_{-H} \equiv \chi_{\bar{H}}$ and $\chi_{H0} = \chi_H$ [38]. In terms of scattering geometries, described in Fig. 2.1, we note that the direction cosines $\gamma_{0,h}$ are different for the Laue and Bragg cases. In particular $\gamma_0 > 0$ for both geometries, while $\gamma_H > 0$ in the Laue case and $\gamma_H < 0$ for the Bragg one[2]. Also the electric wavefield boundary condition are different in the two cases, in fact we can write

$$E_{0s}(0) = E_s^{in}, \quad E_{Hs}(d) = 0 \tag{4.20}$$

for the Bragg geometry and

$$E_{0s}(0) = E_s^{in}, \quad E_{Hs}(0) = 0 \tag{4.21}$$

for the Laue case, where we assume that the amplitude of the incoming beam is $E_s^{in} = 1$ [2, 38].

In order to complete the set of general equation which define the theoretical background which we

are going to refer to in this Chapter, we also need to define the reflectivity factor in the two different scattering geometries. By following the discussion in [2] we can write

$$p_R^B(\Delta\theta) = \frac{|\gamma_H|}{\gamma_0}\left|\frac{E_H(0,\Delta\theta)}{E_0(0,\Delta\theta)}\right|^2 \tag{4.22}$$

in the Bragg case and

$$p_R^L(\Delta\theta) = \frac{\gamma_H}{\gamma_0}\left|E_H(0,\Delta\theta)\right|^2 \tag{4.23}$$

in the Laue geometry.

4.3 Kinematical & dynamical solutions

At this stage we can define the solutions to Eq. 4.18 in the kinematical and dynamical regimes.

In the kinematical approximation we can assume that the transmitted wave does not depend on the diffracted beam's amplitude $E_H(z)$ so that Eq. 4.18 can be written as

$$\frac{dE_{0s}}{dz} = i\delta_0 E_{0s}(z), \tag{4.24}$$

where $\delta_0 = k\chi_0/(2\gamma_0)$ and which has solution [2]

$$E_{0s}^{out} = e^{i\delta_0 d} = exp\left(i\phi_{ref}(d) - \mu_0 d/2\gamma_0\right), \tag{4.25}$$

where the phase shift due to refraction ϕ_{ref} can be obtained from Eq.4.2 as

$$\phi_{ref}(d) = Re\left[\gamma_0 d\right] = \frac{k\chi_0 d}{2\gamma_0}. \tag{4.26}$$

We note that the phase shift defined in Eq. 4.26 does not take multiple scattering into account and it is not related to the rocking angle of the incident beam respect to the medium surface. For this reason, in order to find a way to describe how the coupling between the transmitted and diffracted waves affect the phase shift, we need to move beyond the kinematical regime.

A solution of Eq. 4.18 can be written in the dynamical regime in the form

$$E_0^{out}(d,\Delta\theta) = exp\left(i\phi_{ref} - \mu_0 d/2\gamma_0 + i\phi_{din}(d,\Delta\theta)\right) \tag{4.27}$$

where we are adding a dynamical phase shift

$$\phi_{din}(d,\Delta\theta) = -\frac{1}{\Lambda_0} Re\left[\int_0^d dz' P_1 R(z',\Delta\theta)\right] \tag{4.28}$$

which includes term C_1 which is related to the polarization and thermal factors in the form

$$P_1 = P\left(1 + i\frac{Im\sqrt{\chi_H\chi_{\bar{H}}}}{Re\sqrt{\chi_H\chi_{\bar{H}}}}\right)e^{-W(z)}, \tag{4.29}$$

as discussed in [2]. In this additional phase factor we can recognize the extinction/Pendellösung distance Λ_0 and note the scattering amplitude $R(z,\Delta\theta)$ which was defined by [2] as

$$R(z,\Delta\theta) = \frac{1}{\sqrt{\beta}Y}\left[\frac{E_h(z,\Delta\theta)}{E_0(z,\Delta\theta)}\right]e^{i\mathbf{Hu}(z)} \tag{4.30}$$

where factor β changes in accordance to the reflection geometry. In particular we note that $\beta = \gamma_0/\gamma_H$ for the Laue geometry and $\beta = \gamma_0/|\gamma_H|$ in the Bragg case [2]. Furthermore, the structure of the crystal is represented in Eq. 4.30 with the use of parameter $Y = \sqrt{\chi_H\chi_{\bar{H}}} = |Y|\,exp(i\Phi_Y)$, which in case of a centrosymmetric crystal with a monoatomic lattice becomes $Y = 1$ [2].

At this stage we can obtain a formula for the dynamical phase shift factor in the case of thick and perfect crystals, for which we have that the scattering amplitude R does not depend anymore on the crystal thickness,

$$\phi_{din}(d,\Delta\theta) = -\frac{d}{\Lambda_0} Re\left[P_1 R_0(\Delta\theta)\right] \tag{4.31}$$

where we see a clear dependency on the rocking angle $\Delta\theta$ as discussed in [2]. This equation is an important result and was used by Gorobtsov and Vartanyants to run a number of simulations for crystals of different thicknesses. In particular the authors also helped in the fitting of one of the experimental datasets presented in this Thesis work, by using this formula in order to show how the phase of the transmitted beam varies respect to the rocking angle $\Delta\theta$, as it will be later discussed in

Chapter 6.

4.4 *Quasi-kinematical* approximation

As we already discussed in the previous Chapters, the dynamical theory of diffraction is always valid and only tends asymptotically to the kinematical one when the crystal is thin with respect to the extinction/Pendellösung distance. For this reason, by fitting our experimental data with the use of dynamical diffraction equations we are obtaining a result which is substantially correct. However, Gorobtsov and Vartanyants noted in their paper [2] that one can be more precise by defining another set of equations which are assumed to be valid in a *quasi-kinematical* regime for crystals of thicknesses under Λ_0.

They started their formulation from the result obtained in the kinematical regime, as discussed in Eq. 4.25, and added a phase term $|\delta_{dyn}(z, \Delta\theta)| \ll 1$ to obtain

$$E_0(z, \theta) \approx e^{i\delta_0 d} e^{i\delta_{dyn}(z, \Delta\theta)}. \tag{4.32}$$

In order to retrieve the function defining the additional dynamical phase term, they used Eq. 4.32 to solve the Takagi-Taupin equations written in Eq. 4.18 and obtained

$$\delta_{dyn}(d, \Delta\theta) = -\frac{P^2 \chi_H \chi_{\bar{H}} (kd)^2}{8\gamma_0 \gamma_H} \frac{1}{\Omega} \left[1 - e^{i\Omega} \left(\frac{\sin\Omega}{\Omega}\right)\right], \tag{4.33}$$

where $\Omega(\Delta\theta) = Q(\Delta\theta)\, d/2$, which includes the momentum transfer factor $Q(\Delta\theta) = (2/\Lambda_0)\,[y(\Delta\theta) + iy_0]$ [2]. It is worth highlighting that in the definition of this equation, the authors assumed that for a perfect crystal $\mathbf{u}(z) = W(0) = 0$. We also note that term $y(\Delta\theta)$ is a dimensionless parameter which defines the angular deviation from the Bragg position

$$y(\Delta\theta) = \sqrt{\beta} \frac{sin2\theta_B \cdot \Delta\theta}{Re\sqrt{\chi_H \chi_{\bar{H}}}} \pm \frac{\chi_{or}(1 \pm \beta)}{2\sqrt{\beta} Re\sqrt{\chi_H \chi_{\bar{H}}}}, \tag{4.34}$$

while factor y_0 describes the attenuation of X-rays due to photoelectric absorption

$$y_0 = \pm \frac{\chi_{0i}(1 \pm \beta)}{2\sqrt{\beta} Re\sqrt{\chi_H \chi_{\bar{H}}}} \tag{4.35}$$

as described in [2].

The dynamical phase term δ_{dyn} is a complex parameter so that only its real part gives a contribution to the phase shift due to diffraction $\delta_{\phi_{dyn}}(z, \Delta\theta) = Re\left[\delta_{dyn}(d, \Delta\theta)\right]$. With the use of Eq. 4.33, one can find that the phase of the transmitted wave can be written in the form

$$\delta_{\phi_{dyn}}(d, \Delta\theta) = -\frac{P_1^2}{2}\left(\frac{d}{\Lambda_0}\right)^2 \frac{1}{\Omega} \times \left\{\left(1-p^2\right)\left[1-\cos\Omega\left(\frac{\sin\Omega}{\Omega}\right)\right] - 2p\sin\Omega\frac{\sin\Omega}{\Omega}\right\}, \tag{4.36}$$

where $p = -\frac{Im\sqrt{\chi_H\chi_{\bar{H}}}}{Re\sqrt{\chi_H\chi_{\bar{H}}}}$ [2].

At this stage the authors defined how the dynamical correction factor changes respect to big or small angular deviations from the Bragg angle θ_B. In particular they noted that for big $\Delta\theta$ one can get

$$\delta_{dyn}(d, \Delta\theta) \approx -\frac{P^2\chi_H\chi_{\bar{H}}(kd)}{4\gamma_0\sin 2\theta_B(\Delta\theta - \theta_{ref})} \tag{4.37}$$

note starting from Eq. 4.33, where θ_{ref} is the refraction correction angular term and where the the term in the square brackets and the imaginary part of $\Omega(\Delta\theta)$ were neglected [2]. One can note that Eq. 4.37 agrees with Eq. 4.3 which described the phase shift in periodic media, under the condition of large angular deviations from the Bragg angle.

In order to retrieve the phase contribution for small $\Omega(\Delta\theta)$, the authors noted that when $\Omega(\Delta\theta) \to 0$ one can get from Eq. 4.33

$$\delta_{dyn}(d, \Delta\theta) \to -\frac{P_1^2}{2}\left(\frac{d}{\Lambda_0}\right)^2\left[\frac{2}{3}\Omega - i\right] \tag{4.38}$$

where $\frac{P_1^2}{2}\left(\frac{d}{\Lambda_0}\right)^2 = \frac{P^2\chi_H\chi_{\bar{H}}(kd)^2}{8\gamma_0\gamma_H}$. Furthermore they obtained the phase of the transmitted beam as

$$\delta_{\phi_{dyn}}(d, \Delta\theta) \to -\frac{P^2}{2}\left(\frac{d}{\Lambda_0}\right)^2\left\{\left(1-p^2\right)y(\Delta\theta) + 2p\left[y_0 - \frac{3}{2}\left(\frac{\Lambda_0}{d}\right)\right]\right\}, \tag{4.39}$$

which is the expression that was used to perform the simulations which were then compared with the results obtained in the dynamical regime, as shown in Fig. 4.2[1]. After comparing the results obtained in the *quasi-kinematical* approximation with the dynamical theory ones, the authors highlighted that

[1]The parameters used for the Au {111} solutions are: $Energy = 8.5KeV$, $\theta_B = 18.04°$, $\gamma_0 = 0$, $\gamma_H = 0.808$, $\chi_{0r} = -8.31 \times 10^{-5}$, $\chi_{0i} = 6.87 \times 10^{-6}$, $\chi_{Hr} = -6.83 \times 10^{-5}$, $\chi_{Hi} = -6.83 \times 10^{-6}$, $Re\sqrt{\chi_H\chi_{\bar{H}}} = -6.83 \times 10^{-5}$, $Im\sqrt{\chi_H\chi_{\bar{H}}} = 6.83 \times 10^{-6}$, $\Lambda_0 = 610nm$ [2].

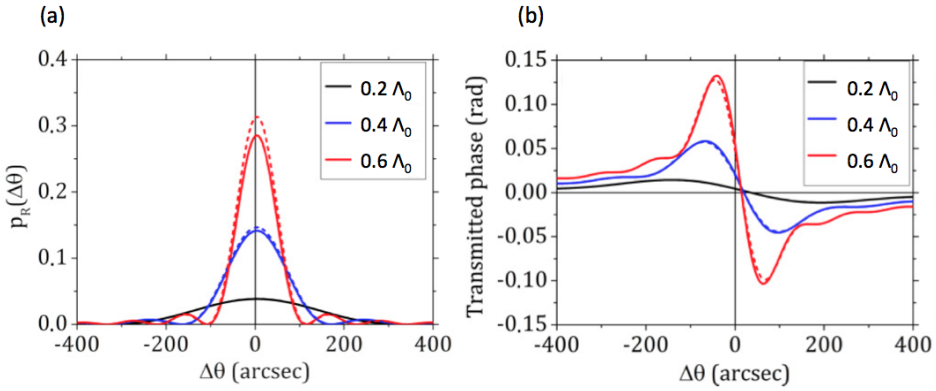

Figure 4.2: Comparison between the dynamical and *quasi-kinematical* approximation simulation for the Au {111} reflection in the Laue geometry for a set of crystal thicknesses ($d = 0.2, 0.4, 0.6\Lambda_0$). (a) Shows the simulations obtained for the reflectivity function $p_R(\Delta\theta)$, while (b) collects the results for the simulated phase of the transmitted beam. In both (a) and (b) the dynamical theory simulations are represented with full lines, while the quasi-kinematical approximation results are shown with dashed lines. In order to quantify the error between the two simulation, Gorobtsov and Vartanyants defined a function $\epsilon = \left|\frac{\delta_{\phi_{dyn}}(d,\Delta\theta) - \phi_{dyn}(d,\Delta\theta)}{\phi_{dyn}(d,\Delta\theta)}\right|$ and found that the quasi-kinematical approach can be used with an error of less than 5% up to Au crystals with thickness $d \simeq 0.8\Lambda_0$ [2]. Figure adapted from [2].

this new theoretical framework can be applied when $|\delta_{dyn}(z, \Delta\theta)| \ll 1$. This condition implies that the maximum crystal thickness allowed in this regime is defined by

$$z \ll d_{max} = \frac{\sqrt{2}}{|P_1|}\Lambda_0 \tag{4.40}$$

so that the *quasi-kinematical* approximation is only valid if the crystal thickness is below Λ_0.

In order to give a complete description of this new approximation regime, one can also define the reflectivity function by noting that the amplitude of the diffracted wave can be written as

$$E_h(d, \Delta\theta) = iE_h^0 e^{i\delta_H z} e^{-i\Omega}\left(\frac{\sin\Omega}{\Omega}\right) \tag{4.41}$$

which includes factor $\delta_H = \frac{k(\chi_0 - \alpha)}{2\gamma_H}$ and where $E_H^0 = Pkd\chi_H/(2\gamma_H)$ [2]. At this point one can substitute the diffracted field in equations 4.22-23 and obtain

$$p_R(\Delta\theta) = \frac{\gamma_H}{\gamma_0}\left|E_H^0\right|^2 \frac{\sin^2\Omega}{\Omega^2}. \tag{4.42}$$

It is worth noting that with the use of Eq.4.41 we can write the dynamical correction factor as a function of the amplitude of the diffracted beam as

$$\delta_{dyn}\left(d,\Delta\theta\right)=-\frac{P_1^2}{2}\left(\frac{d}{\Lambda_0}\right)^2\frac{1}{\Omega}\left[1+i\eta\left(\Delta\theta\right)E_H\left(d,\Delta\theta\right)\right], \tag{4.43}$$

which includes the angular parameter $\eta\left(\Delta\theta\right)=\frac{2\gamma_h}{P(kd)\chi_H}e^{-i\delta_H d}e^{i2\Omega}$ [2].

This recently developed theoretical framework already represents a "next step" respect to the work developed within this Thesis project. We however decided to include a detailed description of this innovative *quasi-kinematical* approximation to show the potential of future developments following the publication of this Thesis work. In particular the complete formulation of this theory will allow, going forward, to have more flexibility when investigating the effects of diffraction under different conditions (i.e. different samples' thicknesses in and out of the dynamical regime) without using drastic approximations which could potentially affect the precise definition of the crystal's structure factor.

Chapter 5

Ptychography

In this Chapter the main aspects of the imaging technique that was used to perform the experiments presented in this Thesis work will be discussed.

Ptychography is an imaging method which was initially proposed by Hegerl and Hoppe in 1970 [40], who also named it starting from the greek word 'ptycho', which means 'to fold', to describe that at the basis of this method there is a convolution operation between two functions (that is two functions folding together in mathematical terms). From the early stages of its development, it was clear that ptychography could have been a useful tool to solve the phase problem, but the limits in the computing power in the early 70s did not allow a real application. For this reason it was only recently that this powerful tool has been further developed and used as an imaging method. The pioneer in the field was John Rodenburg who, together with his collaborators, proved in the late 90s the effectiveness of this method and provided the first inversion algorithm [9, 10, 11, 12, 13].

The X-ray ptychography method is based on the use of a confined and coherent beam, the probe, to scan an extended object at different positions. The resulting set of diffraction patterns is then collected in the far field and used to retrieve the sample's complex-valued transmission function. The probe position is controlled so to always assure an overlap region between two contiguous positions. In contrast to what happens in traditional Coherent X-ray Diffraction Imaging (CXDI) methods [41], ptychography allows to use the additional information contained in the overlap regions to remove the support constraint in the real space, when reconstructing the sample using iterative inversion algorithms [13]. The redundancy of the collected dataset together with the knowledge of each scanning

position, enables to reconstruct the phase of the sample without being limited by its size and at the same time allows to clearly separate the two contributions of sample and illuminating probe. Ptychography can also be defined as a phase sensitive imaging technique because it measures the phase of one part of an object relative to other parts with high sensitivity. This new method has seen rapid development over the past few years and it has been used in many fields, from imaging computer chips [42] to biological samples [43, 44, 45]. Particularly, a phase sensitivity as good as 0.005 rad was also demonstrated [22]. A further development seen in recent years was to remove the requirement of perfect coherence in the beam, as discussed in [14].

5.1 Theoretical principles of ptychography

The idea at the basis of ptychography is to use an highly focused and coherent beam, the probe, to scan an extended object at different positions and to then collect the resulting diffraction patterns in the far field. The scanning probe must move onto the sample in such a way that there is always an overlap region between two contiguous illuminating positions. This causes a redundancy in the datasets which helps to retrieve the phase of the object without the requirements to oversample the diffraction patterns in the Fourier plane and to have a sample of finite extent within the coherent beam. This method has proved to be successful not only in the X-rays regime, but also at optical [46] and electron microscopy [47] wavelengths.

The phase problem is solved with the aid of iterative inversion algorithms which transform and update functions back and forth between the real and Fourier spaces. In particular, the redundancy in the collected data is used to update an object function in the real space, so that there is no requirement for a real space constraint (defined region of space where the real object exists).

A wide range of numerical algorithms was developed in order to implement the reconstruction of both amplitude and phase of an illuminated sample. In this Thesis work we will focus our attention on the PIE, ePIE and Difference Maps algorithms.

5.2 Ptychographic Iterative Engine (PIE)

The PIE algorithm was the first one to be implemented by Rodenburg and his coworkers [48] and it assumes, as well as all the following methods do, a multiplicative relationship between the object

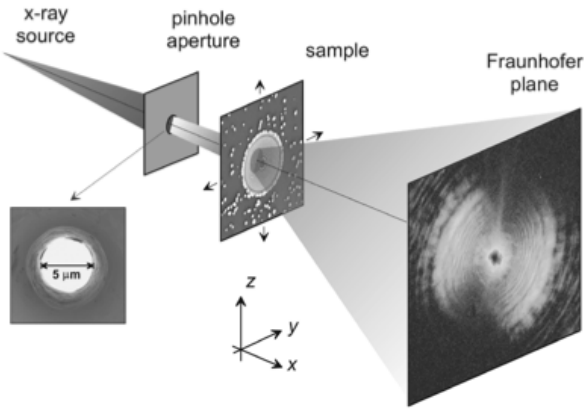

Figure 5.1: Schematic representation of the setup used by Rodenburg and coworkers in 2007, extracted from his publication [11]. In this case the beam was focused with a pinhole and the sample was mounted on a 2D piezo stage which moves on the yz plane. For each probe position a diffraction pattern was recorded by a CCD camera at the Fraunhofer plane (far field). Figure reproduced with permission of the American Physical Society.

and probe complex wave-functions to create the exit-wave

$$\psi(\mathbf{r}) = O(\mathbf{r})P(\mathbf{r}) \tag{5.1}$$

where $O(\mathbf{r})$ is the object function and $P(\mathbf{r})$ the probe or illumination function and where $\mathbf{r}$ is the spatial coordinates vector. In thier paper, Rodenburg et al. pointed out that this relation is generally accurate for thin objects. It is also assumed that $O(\mathbf{r})$ or $P(\mathbf{r})$ can be moved relative to one another by various distances $\mathbf{R}$. When using this method, the illumination function $P(\mathbf{r} - \mathbf{R})$ needs to be known. In the following description it will be considered the case of the probe moving with respect to the object, but the result would not be different if moving the object function instead. In order to use this method it is necessary to know all the illumination functions as well as all the scan positions, and of course all the diffracted intensities collected in the far field.

The whole method followed by the algorithm is graphically shown in Fig. 5.2 and it can be described by several steps.

1. The algorithm starts with a guessed (g) object function in the real space $O_{g,n}(\mathbf{r})$ at the 0th iteration.

2. It is then necessary to multiply the current guessed object function by the illumination function

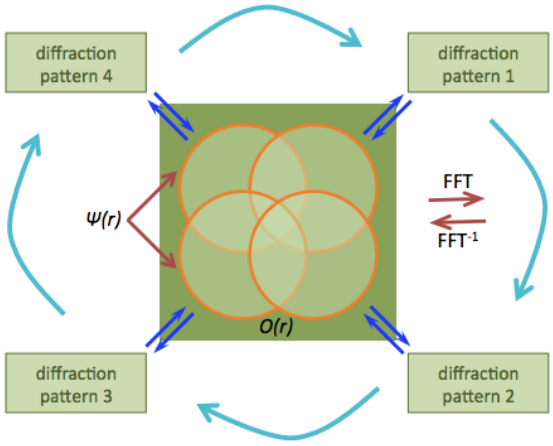

Figure 5.2: Schematic representation of how the PIE algorithm works on four overlapping probe positions (circles) illuminating a region of an extended object (central square). Figure replicated following [11].

$P(\mathbf{r}-\mathbf{R})$ at the current position $\mathbf{R}$, so to produce a new guessed exit wave function

$$\psi_{g,n}(\mathbf{R}) = O_{g,n}(\mathbf{R})P(\mathbf{r}-\mathbf{R}). \tag{5.2}$$

3. The guessed exit wave is then Fourier transformed to obtain the corresponding function in the diffraction space, indicated by the reciprocal space coordinate $\mathbf{k}$.

$$\boldsymbol{\psi}_{g,n}(\mathbf{k},\mathbf{R}) = \mathscr{F}[\psi_{g,n}(\mathbf{R})] = \left|\boldsymbol{\psi}_{g,n}(\mathbf{k},\mathbf{R})\right| e^{i\theta_{g,n}(\mathbf{k},\mathbf{R})}. \tag{5.3}$$

It is worth noticing that this function is a guessed version of the diffracted exit wave, since it is obtained starting from a guessed object function in the real space. Because the transformed exit wave is complex, it can be decomposed in both amplitude and phase.

4. Being the dataset composed by a series of diffracted intensities, it is now possible to replace the guessed amplitude of the transformed exit wave with the recorded one

$$\boldsymbol{\psi}_{c,n}(\mathbf{k},\mathbf{R}) = |\boldsymbol{\psi}(\mathbf{k},\mathbf{R})|\, e^{i\theta_{g,n}(\mathbf{k},\mathbf{R})} \tag{5.4}$$

where $|\boldsymbol{\psi}(\mathbf{k},\mathbf{R})|$ is the modulus of the diffracted intensity.

5. At this point it is possible to inverse transform the modified exit wave, so to obtain a new

improved guess in the real space

$$\psi_{c,n}(\mathbf{k},\mathbf{R}) = \mathscr{F}^{-1}\left|\boldsymbol{\psi}_{c,n}(\mathbf{k},\mathbf{R})\right|. \tag{5.5}$$

6. The guessed object function in the real space is then updated by

$$O_{g+1,n}(\mathbf{R}) = O_{g,n}(\mathbf{R}) + \frac{|P(\mathbf{r}-\mathbf{R})|}{|P_{max}(\mathbf{r}-\mathbf{R})|}\frac{P^*(\mathbf{r}-\mathbf{R})}{\left(|P(\mathbf{r}-\mathbf{R})|^2+\alpha\right)} \times \beta\left(\psi_{c,n}(\mathbf{k},\mathbf{R}) - \psi_{g,n}(\mathbf{k},\mathbf{R})\right) \tag{5.6}$$

where α and β are opportune parameters and $|P_{max}(\mathbf{r}-\mathbf{R})|$ is the maximum value of the illumination function. The value α is used to prevent a division by zero in the case that the modulus of the probe function assumes that value. The constant β controls the feedback in the algorithm and can assume values in the range between 0.5 and 1. At lower values of β the importance of the object function's newest estimate is increased, whereas the previous estimate results more relevant when this parameter assumes higher values.

7. The algorithm continues by moving to a contiguous position, for which there is an overlapping illumination region with the previous one.

8. All steps from 2 to 7 are repeated until the sum squared error (SSE) is small enough

$$SSE = \frac{\left(|\psi(\mathbf{k},\mathbf{R})|^2 - |\psi_{g,n}(\mathbf{k},\mathbf{R})|^2\right)^2}{N}, \tag{5.7}$$

where N is the number f pixels in the array representing the wave function.

The concept underneath this algorithm is similar to other iterative phase retrieval algorithms. For the case where $\beta = 1$ and $\alpha = 0$, and the function $|P(\mathbf{r}-\mathbf{R})|$ is a mask, or support function, this method has many similarities with the well known Fienup algorithm [49].

5.3 Extended Ptychographic Iterative Engine (ePIE)

As the name suggests the ePIE algorithm is an extension of the PIE algorithm where the requirement for an accurate model of the illumination function is removed [12].

For this new version of the algorithm it is necessary to have initial guesses for both the object and probe wave-functions, labelled $O_0(\mathbf{r})$ and $P_0(\mathbf{r})$ respectively. At the starting stage of this method the

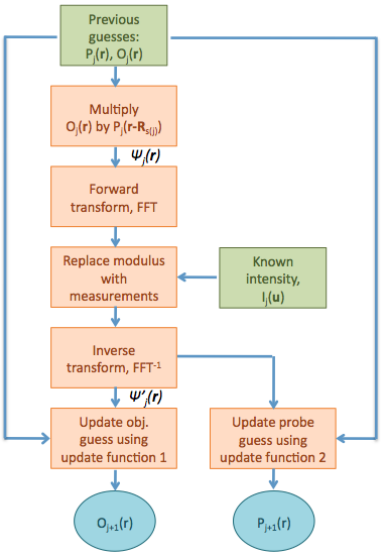

Figure 5.3: Flowchart of the ePIE method. At j=0 initial guesses at both the sample and probe waveforms are provided to the algorithm. Figure reproduced following [12].

object guess is considered as just free-space and the probe function is considered as a support function whose size is approximately given by the intense region of the probe wavefront. Each diffraction pattern then is considered with the update of both the object and probe guesses at each step. The result is a much quicker rate of convergence.

If compared with the PIE method, this new extended version consists on following the steps described above, with the exception of the sixth one, where is a significant change in the use of update function, which is modified and applied to both object and probe functions.

$$O_{g+1,n}(\mathbf{R}) = O_{g,n}(\mathbf{R}) + \frac{P^*_{g,n}(\mathbf{r}-\mathbf{R})}{|P_{g,n}(\mathbf{r}-\mathbf{R})|^2_{max}} \times \beta \left(\psi_{c,n}(\mathbf{k},\mathbf{R}) - \psi_{g,n}(\mathbf{k},\mathbf{R})\right) \tag{5.8}$$

$$P_{g+1,n}(\mathbf{R}) = P_{g,n}(\mathbf{R}) + \frac{O^*_{g,n}(\mathbf{r}-\mathbf{R})}{|O_{g,n}(\mathbf{r}-\mathbf{R})|^2_{max}} \times \alpha \left(\psi_{c,n}(\mathbf{k},\mathbf{R}) - \psi_{g,n}(\mathbf{k},\mathbf{R})\right). \tag{5.9}$$

5.4 Difference Map method

The Difference Map method was initially defined in 2003 for CDI by Elser [50] and then widely

adopted by Thibault for ptychography [51, 52]. The DM algorithm solves those problems that can be expressed as the search for the intersection point between two constraint sets. The exit waves ψ_j ("views" on the specimen) definition helps to relate the two intersecting constraints.

The Fourier constraint which relates the calculated amplitudes to the measured intensities can be written as

$$I_j = \left|\mathscr{F}\left(\psi_j\right)\right|^2, \tag{5.10}$$

while the Overlap constraint imposes that each view can be decomposed into probe and an object functions:

$$\psi_j(\mathbf{r}) = O(\mathbf{r})P(\mathbf{r}-\mathbf{r_j}). \tag{5.11}$$

As it was for the PIE and ePIE algorithm, this method is based on several steps.

1. At the beginning it is necessary to produce an initial guess for the illumination function $P(\mathbf{r})$ and construct an initial state vector , $\boldsymbol{\psi} = \{\psi_1\left(\mathbf{r}\right), \psi_2\left(\mathbf{r}\right), ..., \psi_N\left(\mathbf{r}\right)\}$, where N is the number of probe positions, formed following Eq. 5.11.

2. The method goes on with the update of both object and illumination functions

$$O_g\left(\mathbf{r}\right) = \frac{\sum_j P_g^*(\mathbf{r}-\mathbf{r_j})\psi_j\left(\mathbf{r}\right)}{\sum_j \left|P_g(\mathbf{r}-\mathbf{r_j})\right|^2} \tag{5.12}$$

$$P_g\left(\mathbf{r}\right) = \frac{\sum_j O_g^*(\mathbf{r}+\mathbf{r_j})\psi_j\left(\mathbf{r}+\mathbf{r_j}\right)}{\sum_j \left|O_g(\mathbf{r}-\mathbf{r_j})\right|^2} \tag{5.13}$$

using a small number of alternate applications of equations 5.12 and 5.13 and thresholding the guessed object function$O_g\left(\mathbf{r}\right)$ to maintain all amplitudes smaller than 1.

3. Once we have arrived at this point all views contained in state vector are also updated by using the difference map update function

$$\psi_{j,n+1} = \psi_{j,n}\left(\mathbf{r}\right) + p_F\left(2P_g\left(\mathbf{r}-\mathbf{r_j}\right)O_g\left(\mathbf{r}\right) - \psi_{j,n}(\mathbf{r})\right) - P_g\left(\mathbf{r}-\mathbf{r_j}\right)O_g\left(\mathbf{r}\right) \tag{5.14}$$

where p_F the projection of each views onto the Fourier space constraint set, obtained by replacing the calculated amplitudes with the corresponding experimental diffraction intensities, while keeping the computed phase values.

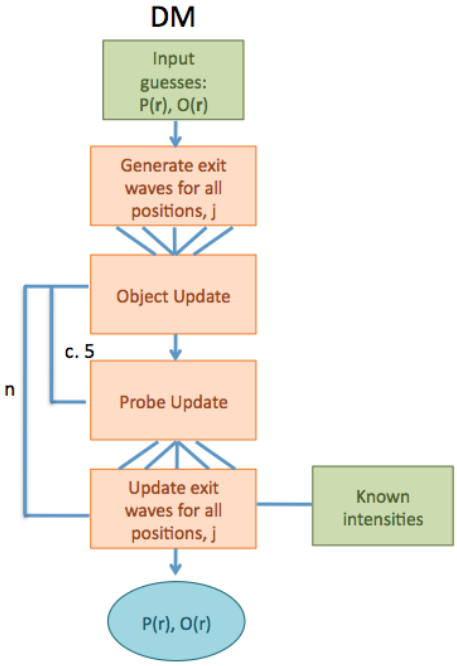

Figure 5.4: Difference Map algorithm flow-chart replicated following [53].

4. The previous 2 and 3 steps are iterated until convergency is reached

$$Error_{n+1} = \|\psi_{n+1} - \psi_n\| .^2 \tag{5.15}$$

There are few big differences between the Difference Map method and ePIE. One is that the former is a parallel method which updates the object and probe functions simultaneously for the entire set of views, so that also the Fourier projection p_F can be calculated in a parallel fashion. This does not happen in ePIE, where all updates and projections are calculated serially. Another difference is in the way the state vector is updated in the DM method.

5.5 Artifacts introduced in the reconstructed phase

In this section, artifacts introduced in the reconstructed objects will be discussed. In particular we will focus on the phase-wrapping phenomenon, which arises with the use of a any inversion algorithm, and on the introduction of phase ramps, which is particularly relevant when dealing with ptychographic reconstructions.

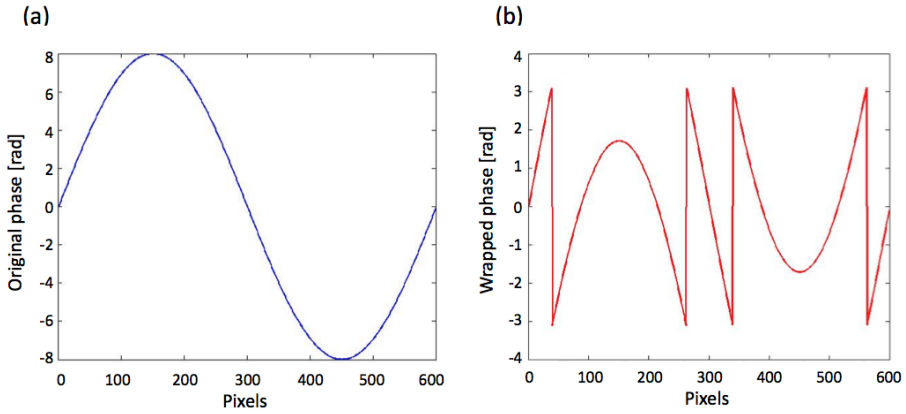

Figure 5.5: (a) A linear phase profile varies between ± 8 radians, thus exceeding the $[-\pi, \pi]$ range. (b) The reconstructed linear phase is only defined in the range $[-\pi, \pi]$, so that for phase values $|\phi| > 8$ we see resulting jumps of $\pm 2\pi$.

5.5.1 Phase wrapping

The phase wrapping is a common artifact introduced by inversion algorithms, as discussed in [54], and is related to the fact the reconstructed phase is is only defined in the range $[-\pi, \pi]$, so that the unwrapping operation is required for the interpretation of the underlying physical quantity, which in the case of our experimental results was the projected index of refraction. In particular, one can observe that reconstructed phase profiles generally show jumps of $\pm 2\pi$, as shown in Fig. 5.5, which the unwrapping process corrects.

A widely used approach for the unwrapping process is to estimate phase differences (gradients) between two neighboring pixels [54]. In this way one can define a phase gradient field that is then used to reconstruct the unwrapped phase. It is also assumed that the phase difference between two adjacent pixels satisfies Nyquist's criterion, so that the discrete gradient $|\Delta\phi| = |\phi_i - \phi_{i-1}|$ should always be less than π, or half a cycle if we make the assumption that a 2π interval corresponds to a complete phase cycle [54].

If we consider the one dimensional case, which can be described by the extraction of a line of phase values from a matrix, we can imagine to estimate the phase by integration of the phase differences from point to point while constantly adding an integer number of cycles that minimizes the phase difference [54]. In particular, we can refer to the example illustrated in Fig. 5.6.a, where a jump of amplitude 0.75 occurs between the third and fourth phase values so that it violates the condition that

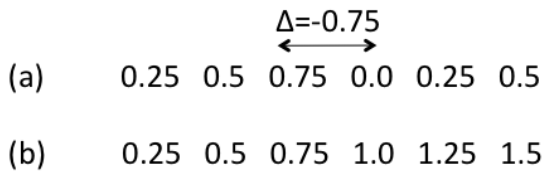

Figure 5.6: 1D phase unwrapping. (a) Wrapped phase values. The phase jump of -0.75 cycles does not respect Nyquist's criterion which demands for the maximum value allowed for a phase jump to be 0.5. (b) Unwrapped phase values obtained by adding a complete cycle to the last three values in (a). The unwrapped result is a phase ramp. It is worth noticing that adding a cycle corresponds to adding 2π to the phases. Figure based on [55].

the maximum allowed gradient has to be less than 0.5 (half a cycle). In this case it is possible to adjust the phases by adding one full cycle to the last three values as shown in Fig.5.7.b. The result is a linear phase ramp without discontinuities, since the gradient between two adjacent phase values is constant in the whole line [55].

In two dimensions the problem needs to be addressed in a slightly different way. Because we are now moving in two directions, we need to make sure that the result should not depend on the chosen integration path. In other words we need tho say that the phase field is a conservative vector field where the integration from one point to another point is path independent [54]. By referring to the irrotational property of conservative vector fields, one can calculate the curl of the vector gradient over a closed loop and have as a result zero

$$\nabla \times \nabla\phi = 0, \tag{5.16}$$

where ϕ is our phase field and ∇ is the gradient operator defined as

$$\nabla = \left(\frac{\partial}{\partial x}\mathbf{i} + \frac{\partial}{\partial y}\mathbf{j} \right),$$

as also discussed in [55]. The assumption that the field is irrotational means that if we consider four adjacent phase values, the summation of the phase gradients over a close loop is equal to zero, as illustrated in Fig. 5.7. What stated above is always true for the unwrapped phase field, so that one can say that because the result of the integration does not depend on the chosen path, the unwrapped gradients completely specify the associated field.

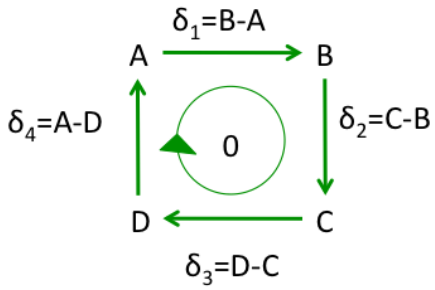

Figure 5.7: Calculation of phase gradients for a set of four adjacent points. Here we assume to move within the points in clock-wise order and to calculate the associated gradients. If $\sum_{i=1}^{4} \delta_i = 0$ the phase field is called irrotational. Figure reproduced based on [55].

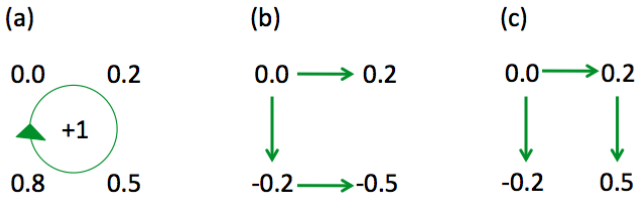

Figure 5.8: 2x2 array of wrapped phase values. (a) The loop integral calculated clockwise starting from value 0.0 gives as a result value $+1$. In this case we calculate $\delta_1 = 0.2 - 0.0 = 0.2$, and similarly we obtain $\delta_2 = 0.3$, $\delta_3 = 0.3$ and $\delta_4 = -0.8$ that violates Nyquist's criterion. In order to unwrap this set of values we should need to add one cycle to 0.0 so that it becomes 1.0 and $\delta_4 = 1 - 0.8 = 0.2$. In this way $\delta_1 + \delta_2 + \delta_3 + \delta_4 = +1$. If we now consider to start from value 0.0 and to recover the unwrapped phases by using the calculated gradients, we can get either (b) or (c), where δ_4 is considered with negative sign. This result shows that when the wrapped phase field is not irrotational, the unwrapped solution is not unique. Figure based on [54] and [55].

Unfortunately this is not the case for the wrapped field, in fact as shown in Figure 5.8, the closed loop integrals of wrapped gradients can give non-zero solutions so that these fields are not conservative [55]. In these cases the curl applied to the gradient field gives as a result a vorticity, or 'residue', whose meaning is that we do not have a unique solution because the obtained result becomes path dependent as shown in Fig 5.8.b-c. The reasons for a non-conservative phase field can for example be undersampling or noise and where the former can be controlled, while the latter is difficult to eliminate.

Because only one unwrapped solution is the true one, finding a correct unwrapping strategy is a problem of great importance. During the years many approaches have been proposed and among them, Goldstein [54] implemented the branch-cut method in 1988. It is based on calculating the gradients

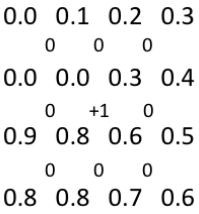

Figure 5.9: 4x4 matrix of wrapped phase values as discussed in [54]. In the central part we can extract a 2x2 array of residue +1. If this 4x4 system is part of a complete wrapped phase field, we can imagine to center a 3x3 searching box around the +1 residue and to move it around in the complete array to look for other non-zero residues. When one is found, the two are connected by a cut. Figure replicated following [54].

and their respective residues in the way we showed above and it is expected that they can only assume values ± 1 and 0. The sign associated to the calculated residues is of great importance, in fact Goldstein made a clear distinction between positively or negatively charged residues. The core of his method is to introduce branch-cuts to connect positive and negative charges in such a way that a cut is 'charge free'. These cuts serve as a barrier for the integration so that no net residue can be included in the unwrapping process and the spreading of general errors is avoided. Local errors in the immediate vicinity of residues may still occur. Those pixels that are at the opposite edges of a cut will certainly see a phase discontinuity of more than half a cycle, but the goal of the method is to minimize the total length of cuts so to minimize the total discontinuity. In this way the inconsistency of the solution is avoided and a final unique unwrapped field is achieved independent of integration path.

Let us consider the case of a two dimensional field of noisy phase measurements of which Fig. 5.9 shows a 4x4 extract. As already mentioned it is possible to calculate the residues of 2x2 pixels sub systems and in this case there is only one point where the residue is +1. If we now imagine to move in the complete phase field, we can imagine to place a box of size 3x3 around this residue and to scan the full matrix until another residue is found. When the residue is found, it is connected to the starting one with a line, or cut. If the cut is uncharged, it is considered complete so that the next residue is selected and same steps are repeated. If a residue is not found, the size of the box is increased to 5x5 and same steps are taken. In the end, all of the residues lie on cuts which are uncharged, so that no global errors are allowed. Where the residues are sparse, they are connected by cuts as shown in Fig. 5.10(b). Where they are very dense as in Fig. 5.10(c), whole areas are isolated so that the algorithm "gives up". In this case it is not possible to obtain an optimum solution, however we can get a good

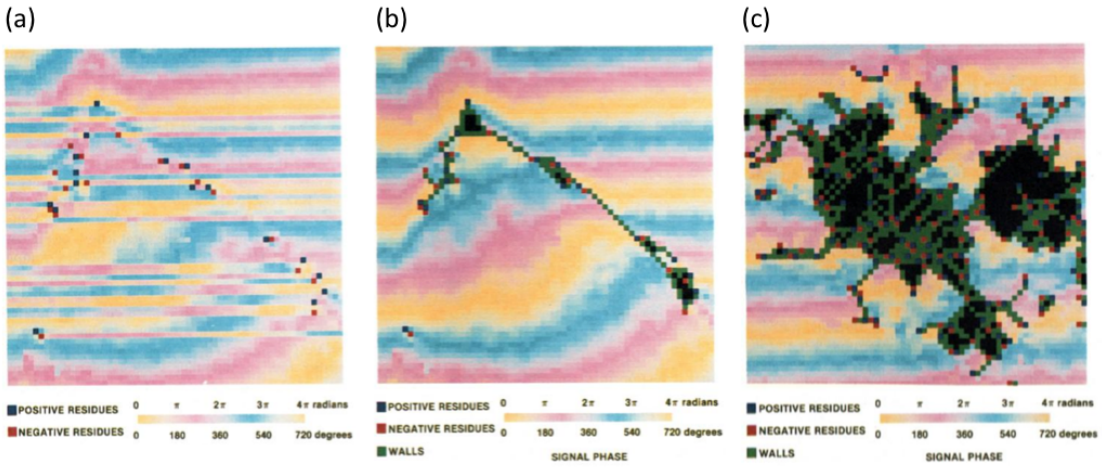

Figure 5.10: Wrapped and unwrapped phase maps. (a) Residues have been calculated by choosing the closest 2π multiple. In this map, two cycles in phase are represented by one revolution of the color bar. (b) Same region of (a) but where cuts are in place before unwrapping, so to avoid global errors. (c) A different region in the phase map showing a high density of residues. The area is entirely isolated from phase estimation because no reliable phase can be calculated in this region. Figures extracted from [54].

approximation over most of the matrix, and where it is not the user is warned by the density of the branch cuts [54].

A practical approach to use when performing the analysis of experimental data is to discard part of the reconstructed object so to only focus on the area around the sample. The definition of a region of interest is a crucial step because the total field of view of an object reconstruction also includes peripheral areas where the signal to noise ratio is very low. In terms of phase unwrapping we can expect that these areas are going to be extremely problematic and no matter how careful we can be when applying our method, they will generate errors that will propagate to other regions. This is in accordance with what showed in Fig. 5.10(c), because if there is a region where the unwrapping algorithm gives up, we can't expect that this is not going to affect the final result in the reconstructed phase. For this reason it is wise to cut the reconstruction defining a proper region of interest before unwrapping the phase, so that we can simplify the algorithm's task and we are sure to obtain a better result.

5.5.2 Phase ramps

Phase ramps are an effect that can be described by considering the Fourier transform relationship between the object and the collected diffraction pattern [56]. These artifacts represent a recurring problem when treating ptychographic reconstructions as discussed in [53, 57], but they also represent a common issue which affects other imaging techniques [58, 59].

The introduction of phase ramps can be explained by recalling the Fourier transform property which identifies a shift in the real space with an additional phase factor in the complex space. In particular one can write

$$F\left[g(x-a)\right] = G(q)e^{-i2\pi qa} \tag{5.17}$$

and apply this transformation to a 2D spatial distribution of light $u(x, y, 0)$, characterized by an angular spectrum $\tilde{u}\left(\alpha, \beta, 0\right)$, to obtain

$$F\left[u(x-x', y-y', 0)\right] = \tilde{u}\left(\alpha, \beta, 0\right) e^{-2\pi i\left(\alpha x' + \beta y'\right)} \tag{5.18}$$

which shows the generation of a linear phase ramp [60]. By recalling that the ptychographic method requires the use of multiple diffraction patterns, collected at overlapping probe positions, we can understand that the presence of phase ramps in the reconstructed object functions are particularly common when this imaging technique is used.

In order to remove the phase ramp from the experimental data presented in this Thesis, we used the method described in [59], which implied the definition of a region of interest around the reconstructed object. Within this region, we then drew masks around the reconstructed sample so to identify empty areas where the phase ramp was the most relevant contribute, as shown in Fig. 5.11.b. The phase information contained within each mask was used to correct the phase ramp affecting the object reconstruction. A result showing the sample after the phase ramp removal step is presented in Fig. 5.12.

The algorithm that we used to remove the linear phase ramps was based on the image registration method described in [61] and was completed by the phase ramp removal technique commented in [59]. In particular, in order to perform our data analysis we used a MATLAB routine developed by Manuel Guizar-Sicairos, which we applied to the reconstructed objects regions defined by appropriate masks, as discussed above.

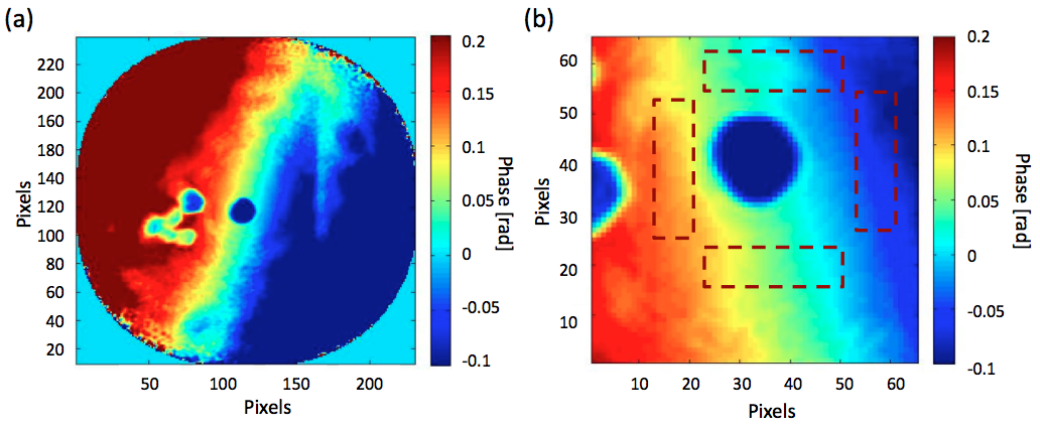

Figure 5.11: Phase ramp removal example. (a) Shows the phase ramp which affects the reconstruction of a gold nanocrystal sample obtained with the difference map method, described in [51, 52]. (b) In order to remove the phase, we drew masks around the reconstructed object so to select empty space areas where the phase was the most relevant contribute. The phase information contained in these regions was then used to correct the phase ramps following [59].

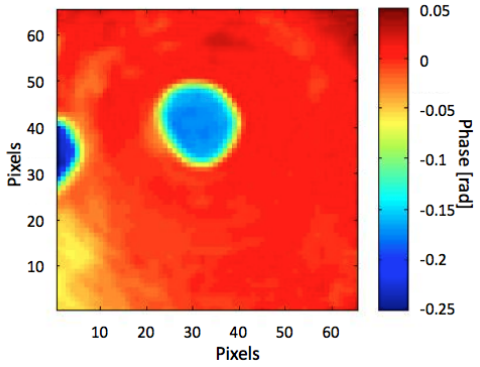

Figure 5.12: Phase of the reconstructed object after the phase ramp removal procedure [59].

The script was able to retrieve the phase correction factors by using a cross correlation function. The main steps of this approach can be described by considering the alignment of two figures, which we can define as two square matrices of complex values. In this case, one figure serves as a reference for the alignment of the other one. The correlation function was computed in the Matlab algorithm as[1]

$$CC = fftshift\left(F\left[Image_{ref}\right]\right) * conj\left(fftshift\left(F\left[Image_2\right]\right)\right), \tag{5.19}$$

where $F\left[Image_{ref,2}\right]$ is the Fourier transform of the input image and where the $fftshift$ function shifts the F-transformed matrices so to move their zero-frequency components to the centre of the array [62]. In order to retrieve the phase shift correction factors, the script computed the 2D inverse Fourier transform of the CC function

$$CC' = ifft2\left(ifftshift\left(CC\right)\right) \tag{5.20}$$

where $ifftshift$ is a function used to swap the quadrants of the CC matrix [62]. At this point the method calculated the maximum value of CC' to obtain the shift value which was needed in order to align $Image_2$ respect to the reference one $Image_{ref}$.

In the specific case of our data analysis, the reference image was given by

$$Image_{ref} = ifftshift\left[mask \times abs\left(Object\right)\right], \tag{5.21}$$

while the second image was defined as

$$Image_2 = ifftshift\left[mask \times Object\right] \tag{5.22}$$

where the $Object$ array represents the output of the ptychographic reconstruction process and the $mask$ matrix was identified by selecting areas in the reconstructed image, as discussed in Fig. 5.12. With the use of these inputs, the cross correlation function allowed to determine the phase shift factors

[1] The script also required to specify an upsamplig factor which is used to define the registration precision. In particular we used an upsampling factor of 20, which means that the images where registered within 1/20 of a pixel, as discussed in [61].

(x', y') which were able to correct the phase ramps as

$$\tilde{u}\left(\alpha, \beta, 0\right) e^{-2\pi i\left(\alpha x' + \beta y'\right)} e^{2\pi i\left(\alpha x' + \beta y'\right)} = \tilde{u}\left(\alpha, \beta, 0\right). \tag{5.23}$$

Chapter 6

First experimental results: gold nanocrystals

6.1 Ptychography on gold nanocrystals

For our first attempt to measure the phase of the forward diffracted beam at different rocking angles we decided to use gold nanocrystals, which are characterized by a relatively not complex crystalline structure. In fact, this material is composed by a regular repetition of cubic unit cells containing 4 Au atoms positioned at each corner.

In this Chapter we will present in details the experimental method, based on ptychography, which we used to measure the intensity of the forward diffracted beam. Furthermore we will also discuss the phase shift curves obtained with the aid of two fitting methodologies: an approximate kinematical fitting and a more detailed dynamical one, developed within our collaboration with Vartanyants, Shabalin and Gorobtsov [23].

6.1.1 Experimental setup

The experiment was conducted at the coherent small-angle X-ray scattering (cSAXS) beamline at the Swiss Light Source, Paul Sherrer Institute in Villigen, Switzerland. The experimental setup, shown in Fig. 6.1, was composed of several components precisely aligned with the aid of an X-ray camera. To focus the beam we used a 75 micron diameter Fresnel Zone Plate (FZP) made of Au with 100

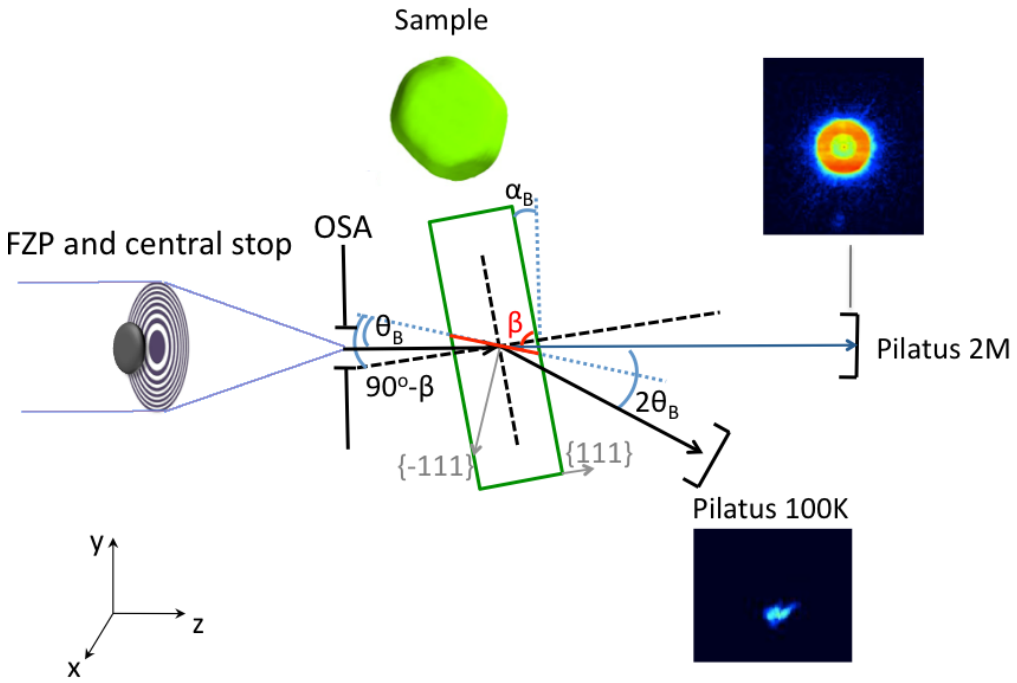

Figure 6.1: Lateral view of the experimental setup. A Fresnel zone plate is used to focus the beam. The Au nanocrystals were placed at the focus with their {111} crystal planes oriented at the angle α_B with respect to the incoming beam. A 2D detector is placed in the forward direction and another 2D detector in the direction of the Bragg reflection.

nm outermost zone width, and 1 micron thickness. A central stop of 30 micron diameter was placed upstream the FZP to block the zeroth diffraction order. Downstream of the FZP we used a 20 micron pinhole serving as order sorting aperture (OSA) to select the first diffraction order. The focal length of the zone plate was 52.66 mm at the energy of 8.7 KeV.

Our sample consisted of a random array of 250 nm gold nanocrystals with cylindrical shape, grown on a 100 nm thick Si_3N_4 membrane. The scanning electron microscope (SEM) analysis confirmed the size of the crystals and showed a mutual spacing of approximately 1 micron. The Au nanocrystals were oriented with the {111} crystallographic planes normal to the substrate. By rotating the sample membrane to an angle of $\alpha_B = 1.86$ deg, we aligned the Au {111} reflection, with Bragg angle $\theta_B = 18$ deg. The sample was mounted downstream at the focus of the FZP which was illuminated with a coherent beam, forming the ptychographic probe. The expected beam size for this experiment is equal to the FZP outermost zone width of 100 nm, but a more precise estimation can be done by analyzing

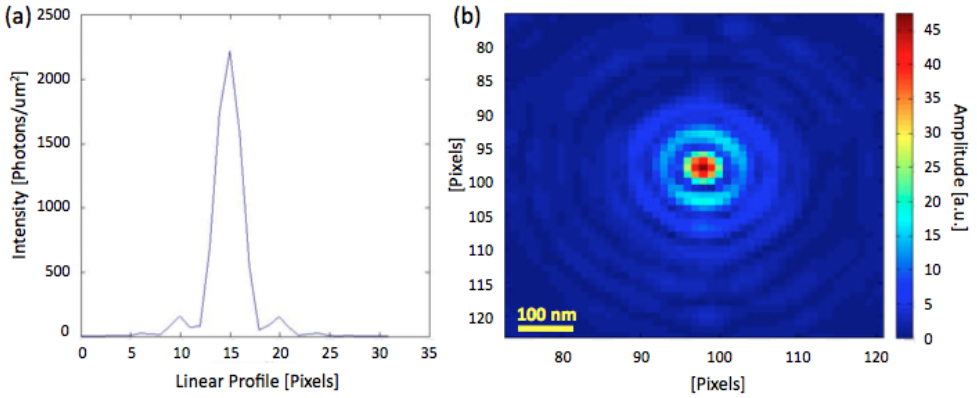

Figure 6.2: Reconstructed probe's intensity linear profile (a) and amplitude (b).

the reconstructed probe profile (Fig. 6.2). The beam size can be retrieved by measuring the FHWM in the probe linear profile and by multiplying it by the pixel size at the sample plane which for this configuration is around $31nm$.

$$pix_{sample} = \frac{\lambda z}{npix_{det}} \tag{6.1}$$

where z is the sample-detector distance, in this case $7.2m$ in the forward direction and n is the recorded data array size, 192 for us. The result is a beam size of around $110nm$ which is consistent with what expected.

In order to collect the diffracted and transmitted intensity distributions while scanning the sample across the probe, we used two Pilatus detectors. As shown in Fig. 6.1, a Pilatus 2M detector was placed at 7.2 m from the sample in the transmission direction, while a smaller Pilatus 100k was placed at the reflected Bragg direction at an angle $2\theta_B = 36$ deg and at a distance of 1.03 m.

We started our experiment by finding a crystal at the precise Bragg angle at which our reflection detector would collect the highest intensity (as shown in Fig. 6.3), then we defined a series of angles centered around the Bragg angle and we performed a ptychographic acquisition at each of them. The rocking curve showing the integrated intensities measured for a set of nine scans around the Bragg angle can be observed in Fig. 6.4. Once defined the rocking curve, we performed a series of ptychographic acquisitions by circular-scanning the sample.

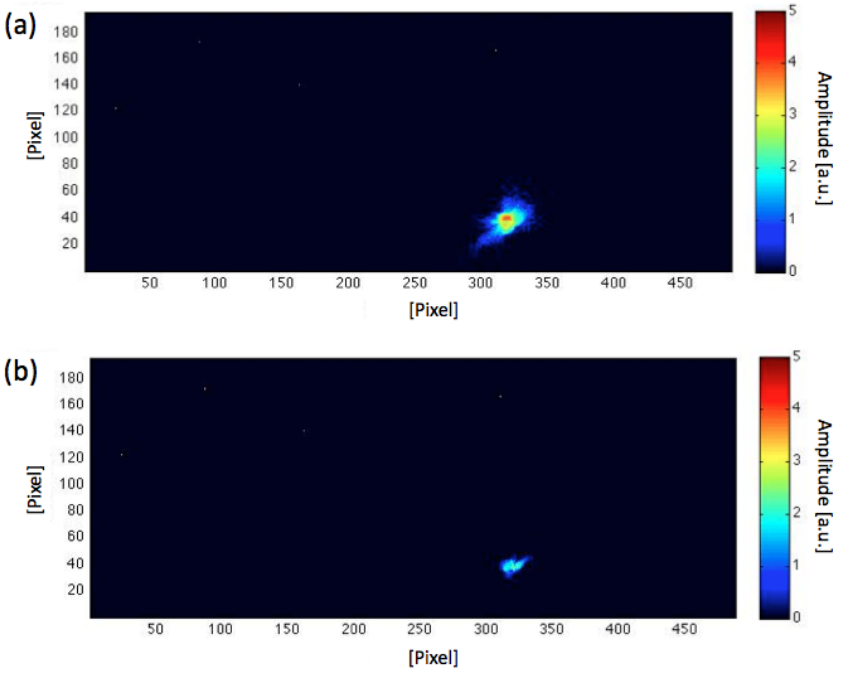

Figure 6.3: Recorded intensity on the Pilatus 100k detector. In (a) the Bragg angle is detected, while in (b) the weaker intensity confirms that we are off the Bragg condition.

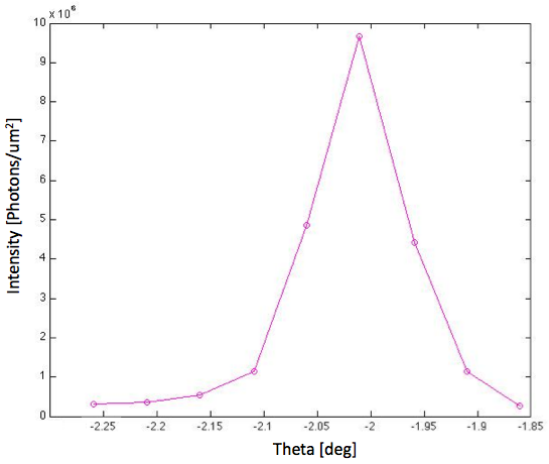

Figure 6.4: Rocking curve for a set of scans. The peak of the rocking curve is located at the Bragg angle which here is shown in lab coordinates at approximately -2.01 deg.

6.1.2 Data analysis

Each ptychographic data sets consisted of a series of 458 acquisitions of 0.5 sec in a grid of concentric circles with a radial step size of 0.05 microns covering a field of view of 1.2x1.2 microns [45]. Ptychographic reconstructions, shown in Fig. 6.5, were performed with the use of the difference map algorithm described in [51, 52]. One can notice that the obtained phase images were affected by a linear phase ramp which was corrected, in a following step, with a removal method based on the search of gradients, as described in Chapter 5 [59]. It is worth noticing that the presence of the linear phase ramp was also a consequence of the fact that the field of view of each reconstruction also included other structures as well as the edge of the sample support, as shown in Fig. 6.5. For this reason, we defined a region of interest around the crystal in order to only concentrate the data analysis on that portion of the reconstructed phase. The following step of our data analysis consisted on the comparison of the different phases obtained for each rocking angle. To this purpose, we wanted to extract a linear phase profile from each reconstruction. However, before being able to do so, an alignment step was necessary so to make sure that the phase was extracted at the same position for each reconstruction. In order to correct the drifts which affected the ptychographic reconstructions, we used a sub-pixel registration

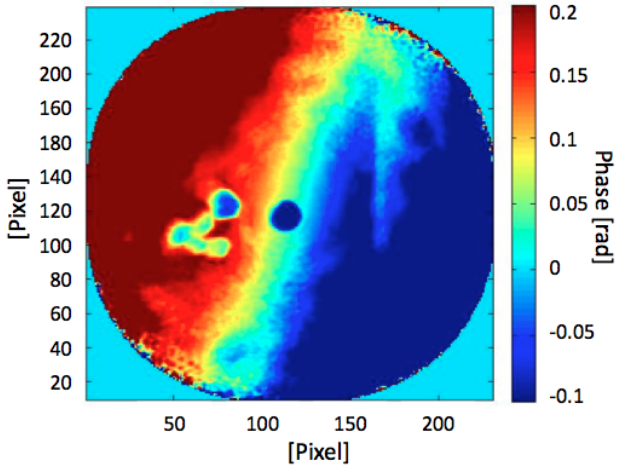

Figure 6.5: Sample's reconstructed phase. The initial phase reconstruction presented a large field of view, which included both the crystal and other structures, including the sample support (line on the right). In order to conduct our data analysis, we decided to define a region of interest around the sample as shown in Fig. 6.6. Each pixel in the reconstructed image corresponds to a size of 31.2 nm.

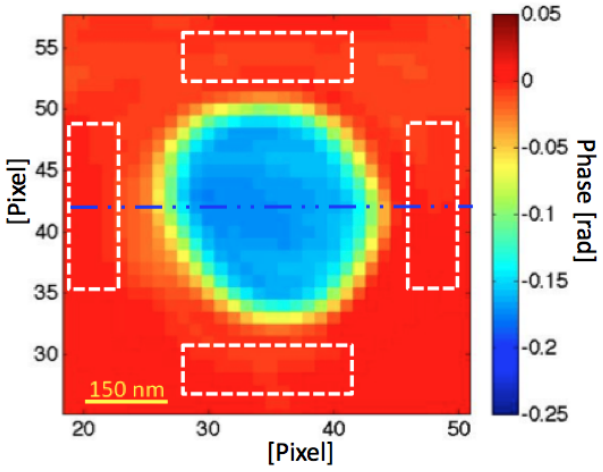

Figure 6.6: Phase ramp removal. In order to remove the phase ramp we drew masks around the crystal after defining a region of interest. The figure already shows the outcome of the data analysis where the phase ramps is removed. The next step of the data treatment was to extract the linear phase profile for each reconstruction obtained at different rocking angles. To this purpose we defined a line across the sample (here shown in blue) and used its coordinates to retrieve the phase profiles shown in Fig. 6.7.

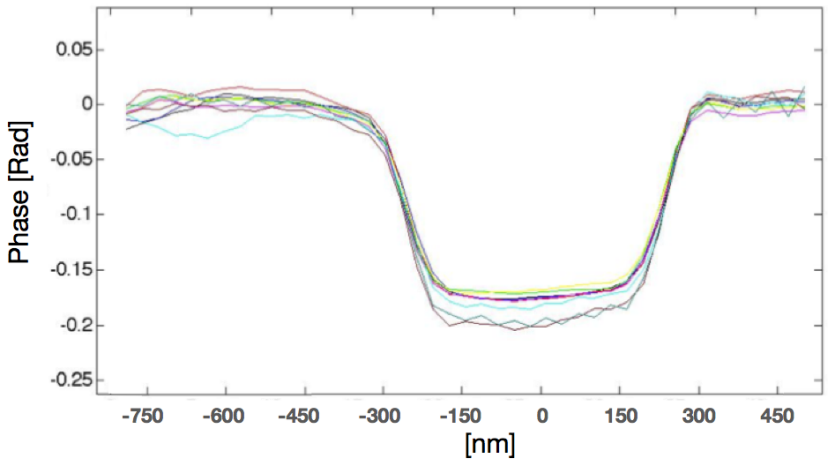

Figure 6.7: Phase profiles obtained after the phase ramp removal and alignment procedures. Each line in the graph corresponds to a different rocking angle around the Bragg condition (9 scans in total). The figure allowed to quantify the phase difference between the area inside the crystal and its surroundings, which resulted to be of approximately 0.18 rad. Furthermore here we can appreciate the elevated phase sensitivity which we could achieve with the use of ptychography. In fact we were able to differentiate the phase values obtained for different illumination angles within an interval of c. 0.03 rad.

method based on [61]. After the alignment step we were able to extract the linear phases from each reconstruction and we obtained the combined profiles shown in Fig. 6.7. Here we observed a phase shift between the Au particle and the surrounding area of about 0.18 rad, which is the expected value for a crystal thickness of 102 nm, assuming a refractive index of $\delta = 4.0 \times 10^{-5}$ for Au at 8.7 keV [63]. More importantly, we observed that this phase shift varied slightly for different rocking angles θ around the Bragg angle θ_B. In order to finely measure the resulting phase shifts inside the crystal, which appeared to be of approximately 0.03 rad as shown in Fig. 6.7, further analysis were needed. In particular we wanted to make sure that the noise outside the crystal was negligible if compared with the phase shift inside the crystal itself. For this reason we wrote a Matlab routine to draw boxes of same sizes outside and inside the crystal, as shown in Fig. 6.8. We then used the phase values in each box to estimate the mean value and the standard deviation. In this way it was possible to calculate the error which affected the reconstructions and to define error-bars which helped to establish if the phase shift inside the crystal was bigger than the noise or not. As a result we obtained a curve of

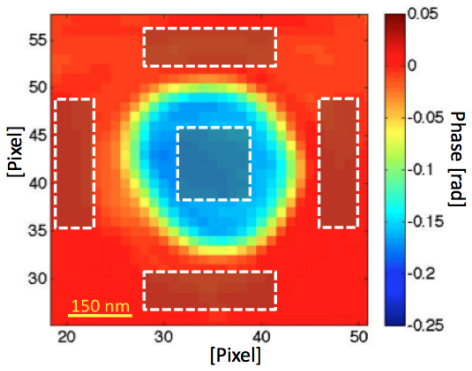

Figure 6.8: Boxes used to calculate the mean value and the standard deviation of the phase inside and outside the crystal. In order to make sure that the phases contained within each box were comparable, we used boxes of equal size both inside and outside the crystal.

the phase shift as a function of the rocking angle θ showing nine points, one for each measurement, with their relative error-bars, as shown in Fig. 6.9. The phase value for each scan (identified by the correspondent angle) was calculated as

$$phase_{av} = phase_{av,c} - \frac{phase_{av,1} + phase_{av,2} + phase_{av,3} + phase_{av,4}}{4} \tag{6.2}$$

where $\text{phase}_{\text{av,c}}$ is the average phase calculated in the box inside the crystal and $\text{phase}_{\text{av,i}}$ are the phases calculated in the four boxes outside the crystal. The error-bars were calculated for each scan by combining the standard deviation of the phase in each box following the formula

$$\varepsilon_{tot} = \sqrt{\varepsilon_c^2 + \frac{1}{16}\varepsilon_1^2 + \frac{1}{16}\varepsilon_2^2 + \frac{1}{16}\varepsilon_3^2 + \frac{1}{16}\varepsilon_4^2} \tag{6.3}$$

where $\varepsilon_{\text{i}}$are the squared standard deviation inside and outside the crystal.

A comparison between the linear phase profiles and the phase shift curve is presented in Fig. 6.10.

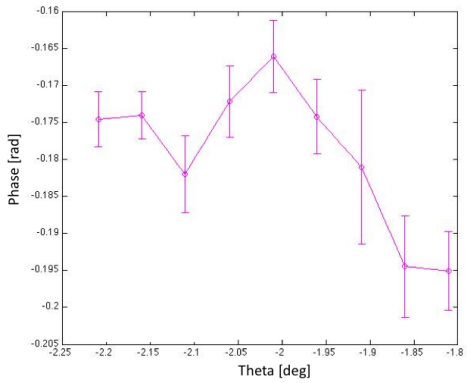

Figure 6.9: Error-bar plot showing the phase shift. The error-bars are represented for each scan with an amplitude of $\pm\varepsilon_{tot}$; the biggest error bar has an amplitude of $\pm\varepsilon_{tot} = 0.02$ rad. The plot is centered around the Bragg angle position, here corresponding to c. -2.01 deg in lab coordinates. Here we can see that the maximum phase shift between the on and off Bragg conditions is around 0.03 rad, as previously shown in Fig. 6.7. More details about the fitting procedure will be provided in the next section of this Chapter.

6.1.3 Data fitting

In order to fit our experimental results we decided to use the equations derived in Chapter 2 for the kinematical regime, where in a first approximation we decided to neglected thermal effects and deformation factors.

As we already discussed, a kinematical approximation is legitimate in this experimental environment because the sample's thickness of 100nm is much smaller respect to the correspondent Pendellösung distance, as shown in Table 3.1. However, it is worth mentioning that a pure kinematical theory neglects the interaction between the transmitted and diffracted waves, which is the dynamical effect at the basis of the phase shift that we were able to measure with our experiments. For this reason here we propose a fitting based on the equations developed in Chapter 2, in an approximate quasi-kinematical regime which would allow to relate the transmitted beam to the diffracted one.

In this approximate environment, we considered that the forward diffracted wave can be obtained by the complex sum of the incident and reflected beams

$$\psi_T(\mathbf{Q}) = \psi_I(\mathbf{Q}) + \psi_R(\mathbf{Q}) \tag{6.4}$$

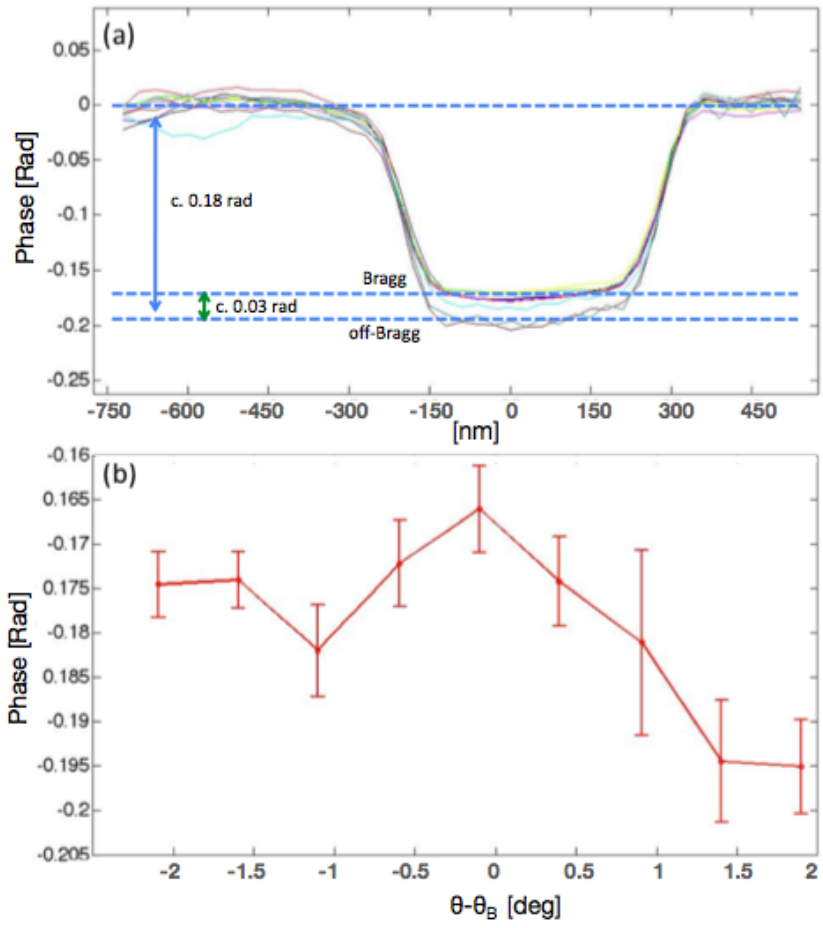

Figure 6.10: (a) Linear phase profiles for different angles around the Bragg reflection and (b) transmitted beam's phase shifts as a function of the rocking angle $\Delta\theta = \theta - \theta_B$. The two figures both confirm that the overall phase shift around the Bragg condition can be estimated as c. 0.03 rad.

where $\psi_T(\mathbf{Q}) = \psi_I(\mathbf{Q})T(\mathbf{Q})$ and where, in analogy with Eq. 2.53, we can decompose the complex amplitude of the scattered beam by only considering the phase contributions from each diffracting plane, as

$$\psi_R(\mathbf{Q}) = \psi_I(\mathbf{Q})R(\mathbf{Q}) = \psi_I(\mathbf{Q})\alpha\frac{1-e^{iqN}}{1-e^{iqd}}, \tag{6.5}$$

where N is the number of planes being considered, α is a complex parameter which can be used to adjust the fitting to experimental data and d_j are the positions of the planes in the crystal[1]. The term d is the 111 plane spacing, which is 0.235 nm for gold.

By using this set of equations, we wanted to describe how the generation of the reflected beam has a perturbative effect on the forward transmitted wave. As a result, we were able to achieve a fitting of the experimental curve by using the equation

$$T(\mathbf{Q}) = 1 + \alpha R(\mathbf{Q}) \tag{6.6}$$

where with the use of a real fitting parameter $\alpha = -0.013$, we could obtain the curve shown in Fig. 6.11 (green lines).

The result discussed so far helped us understand the mechanism at the basis of the phase effect that we were able to detect. However, our approximate fitting, while being able to track the experimental curve, fails to give a complete and detailed theoretical description of the phase shifts that we were able to observe. For this reason we started a collaboration with Vartanyants, Shabalin and Gorobtsov [23], who performed a second fitting based on the dynamical theory of X-ray diffraction [27]. In this model the complex wave field on the exit surface of the crystal was obtained with the use of Takagi-Taupin equations [29], which were solved following the approach described in [2] in analogy with the simulations presented in Chapter 4, which also referred to Au samples in the {111} reflection in the case of σ polarization. The resulting fitting curves for the rocking curve amplitude and the transmitted wave phase are presented as blue lines in Fig. 6.11, where we note the consistency with the approximate quasi-kinematical fitting previously described. It is worth mentioning that the TT formalism used by Vartanyants, Shabalin and Gorobtsov also compensates for the fact that while rocking the sample at different angle we could not consider anymore the geometry of a symmetric Laue reflection.

[1]Here we considered a polarization factor $P = 1$, corresponding to the σ polarization of the X-ray beam that was used to perform the experiment. Because this measurement was conducted while maintaining the X-ray beam always perpendicular to the gold nanocrystal's surface, the polarization factor could be considered as $P = 1$ for the entire length of the experiment.

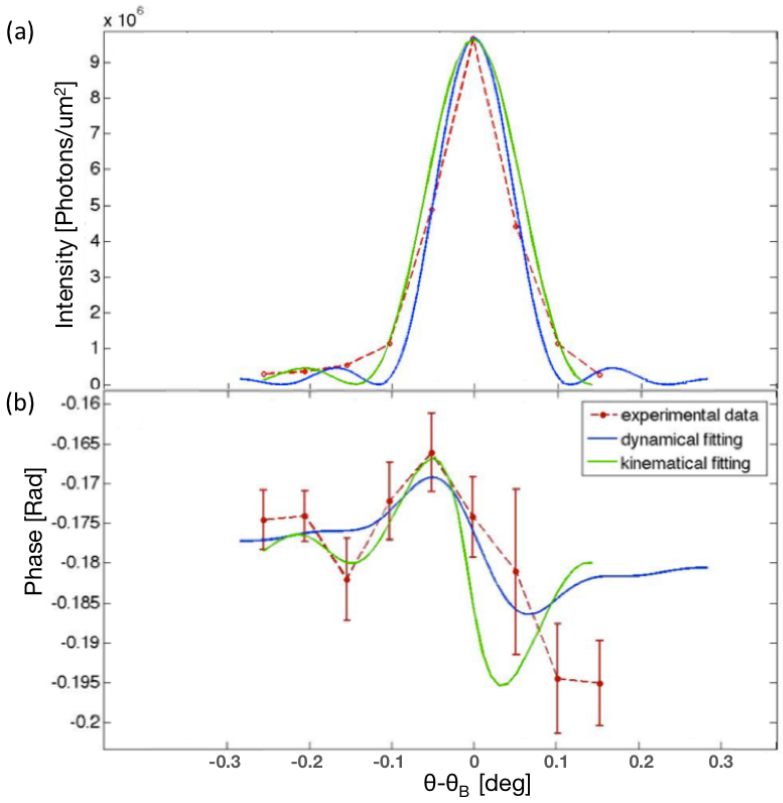

Figure 6.11: (a) Rocking curve of diffracted intensity and (b) transmitted phase shift including both the our customized quasi kinematical fitting and the dynamical fit curves obtained with the theory described in Chapter 4[2]. The parameters used for our customized fitting were $\alpha = -0.013$ and $N = t/d = 426$, where $t = 100nm$ is the sample thickness. The dynamical diffraction fitting is discussed in the text.

In their recent paper, Gorobtsov and Vartanyants [2], also discussed the validity of the Ptychographic method used to perform these measurements. In particular they investigated the nature of the object function by noting that in a typical ptychographic experiment one can write the exit wave as

$$\psi_{exit}\left(\mathbf{r}-\mathbf{r_j}\right)=\int G\left(\mathbf{r}-\mathbf{r}'\right)\psi_{in}\left(\mathbf{r}-\mathbf{r}'\right)d\mathbf{r}' \tag{6.7}$$

where $\psi_{in}\left(\mathbf{r}\right)=P\left(\mathbf{r}\right)$ is the incident wave, or probe, $\mathbf{r_j}$ is the position of the beam on the sample and G is the Green function [27] describing the propagation of X-rays in a crystal [64, 2]. By recalling the equations developed in Chapter 5, we can note that the exit wave can also be written as $\psi_{exit}(\mathbf{r}-\mathbf{r_j})=O(\mathbf{r})P(\mathbf{r}-\mathbf{r_j})$ so that we can obtain

$$O\left(\mathbf{r}\right)=\int G\left(\mathbf{r}-\mathbf{r}'\right)d\mathbf{r}' \tag{6.8}$$

which shows that the object function is defined by the Green function of the crystal. This equation highlights several aspects related to the validity of our experimental method [2]. In particular, the relationship between the exit wave and the Green function tells us that the phase of the transmitted beam is completely defined by the sample structure and it is not affected by the incoming beam shape. Furthermore, the possibility to extend the results obtained with the ptychographic method can be extended to all beam shapes if the variations of the incident wave are smaller if compared to those of the Green function [2]. In particular, Gorobtsov and Vartanyants highlighted that the Green's function variations reach at most the size of the Borrmann fan [27]

$$d_{Borrmann}=d\frac{\sin 2\theta_B}{\gamma_0\gamma_h}, \tag{6.9}$$

which for our Au nanocrystal of thickness $d=100$ nm is $d_{Borrmann}=70$ nm [2]. In order to asses if our experimental results were affected by the incoming beam's shape, we then need to verify that the crystal lateral size was bigger than this quantity. Given that the gold nanocrystals used in our experiments had a lateral size of 250 nm, well above the Borrmann fan, we are able to confirm that our reconstructions were not sensitive to the shape of the incident wave.

For the sake of clarity, we highlight how the reduced size of the samples used in our experiments implies a system which does not have a fully translational theory, for this reason the analysis showed

above would require the use of a two-argument Green function, so that Eq. 6.7-8 should be function of $G(r, r')$.

Further considerations can be made regarding the divergence of the beam. As discussed in [2], in order to establish if this factor is going to affect the experimental results, we should verify that the following conditions are satisfied

$$\begin{aligned} \delta\theta &\ll \tfrac{4\gamma_h}{2d\sin(2\theta_B)} \\ \delta\lambda/\lambda &\ll \tfrac{4\gamma_h}{4d\sin^2\theta_B}, \end{aligned} \tag{6.10}$$

where $\delta\theta$ is angular divergence of the incoming beam and $\delta\lambda/\lambda$ represents the wavelength spread. Following the results obtained, Gorobtsov and Vartanyants confirmed that for experiment conducted on Au {111} crystals at 8.5KeV, the two conditions are comfortably met at third-generation synchrotron facilities[2]. In addition to that, we however acknowledge that the results presented so far are not based on a complete boundary conditions analysis, which would be required in order to fully present the theory around the Borrman fan and the beam's divergence. At this stage, we can understand that the development of a complete boundary condition analysis would be necessary in order to refine the theoretical apparatus presented so far and that this certainly can be seen as a next step to this Thesis project.

It is worth highlighting that the dynamical fitting obtained for the experimental dataset discussed in this Chapter is also consistent with the recently developed *quasi-kinematical* approximation described in Chapter 4. In fact, as previously discussed, the simulations which compared the dynamical and *quasi-kinematical* fittings showed an overall agreement, with an error of less that 5%, for crystals with a thickness up to $d \simeq 0.8\Lambda_0$ [2]. We can confirm that this condition is fully satisfied for the experimental results presented in this section, so that we can confidently assume that the curve that we presented also describes, with a good approximation, the *quasi-kinematical* regime as defined by Gorobtsov and Vartanyants.

[2]The experiments conducted on gold nanocrystals were performed at the energy of 8.7KeV. From calculations we found that the impact of this change in energy does not impact on the validity of this statement.

Chapter 7

Design and preparation of new samples

After being encouraged by our results on gold nanocrystals, we decided to test our experimental technique on other samples characterized by a different crystalline structure. In particular, it is worth highlighting that the FCC crystalline structure of gold nanocrystals is composed by conventional unit cells which only contain 4 atoms, disposed at the corners of the cubic unit cell volume. For this reason one could argue that the detection of the transmitted wave phase shift could have been facilitated by the use of a crystal with a rather elementary structure. In order to test the validity of our method we then decided to prepare new samples with a higher number of atoms in the unit cell and, in one case, by the presence of different elements. As a consequence we decided to use Si and InP, having both a FCC crystalline structure with 8 atoms in their unit cells. A schematic representation of the different unit cells is discussed in Fig. 7.1. In addition to that, we also wanted to avoid the problems that we encountered when performing the Au nanocrystal experiment. In particular, the fact that the crystals where deposited on a thin membrane, made the sample extremely easy to break. For this reason, in order to have more robust samples, we produced structures by etching crystalline wafers. Finally, given that we already knew the geometry of the experimental setup to be used, we designed our samples so to arrange for the beam to be perpendicular to the block at the chosen Bragg conditions. In this way, also the distance travelled by the incident beam was well-defined.

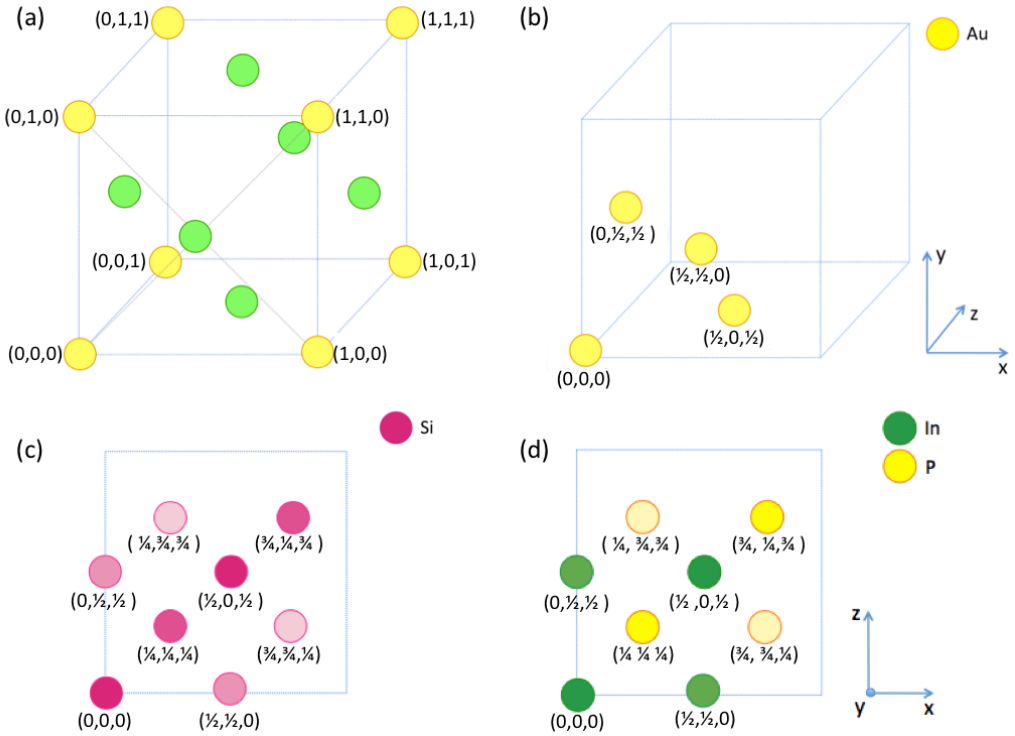

Figure 7.1: (a) 3D view of the conventional unit cell for the FCC lattice. In this structure there are 8 atoms distributed as shown: the yellow dots represent atoms at the vertices of the cube, while the green ones are at the centre of each facet. (b) 3D view of the Au conventional unit cell. Here we consider 4 atoms whose spatial coordinates are shown in the figure. (c) Top view of the Si unit cell. The coordinates are shown by each atom and the various shades refer to a different y-level. (d) Top view of the InP unit cell, where the two components are shown in green and yellow, respectively. The choice of placing the In at (0,0,0) is arbitrary and it might affect the results of the structure factor calculation as it will be later discussed in the text.

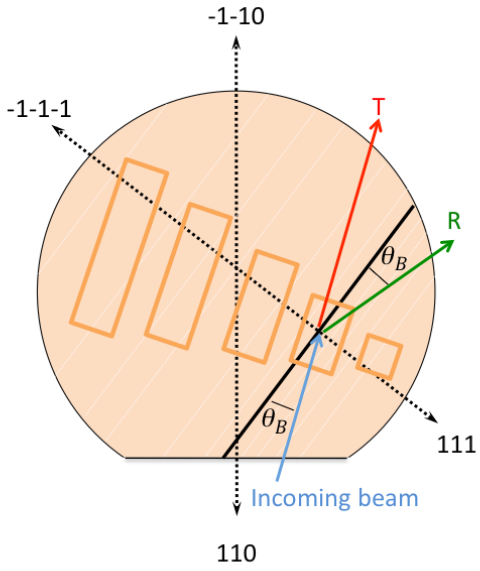

Figure 7.2: Schematic representation of our design. After identifying the [111] crystallographic direction, we considered its perpendicular set of planes (black bold line and white lines). In order to simplify the experimental setup, we cut a series of pillars (orange rectangles-top view) in such a way that the incoming beam at the Bragg angle (blue arrow) would already be perpendicular to the pillars' facets. Θ_B represents the Bragg angle.

7.1 Sample's design

The first samples that we worked on were the Si ones and we started from a {110} monocrystalline wafer. The starting idea for our samples was to obtain crystalline pillars by etching the wafer. Furthermore, because we wanted to observe the Bragg condition relative to the (111) plane of Si, we prepared our pillars in such a way that a beam almost perpendicular to the pillars' facets would have been able to easily reach the requested angle. It is worth noticing that for the {110} wafer, both transmitted and {111} Bragg reflected beams lie in the same plane as the wafer itself. A graphic representation of this design is shown in Fig. 7.2. In order to define the orientation angle of our pillars we calculated the position of the (111) plane respect to the [110] direction using the geometrical formula[1]

$$cos\phi = \mathbf{V}_1 \cdot \mathbf{V}_2$$
$$\phi = cos^{-1}\left(\frac{\mathbf{V}_1 \cdot \mathbf{V}_2}{|\mathbf{V_1}| \cdot |\mathbf{V_2}|}\right) \tag{7.1}$$

[1]Eq. 7.1 only applies to unit-lenght vectors.

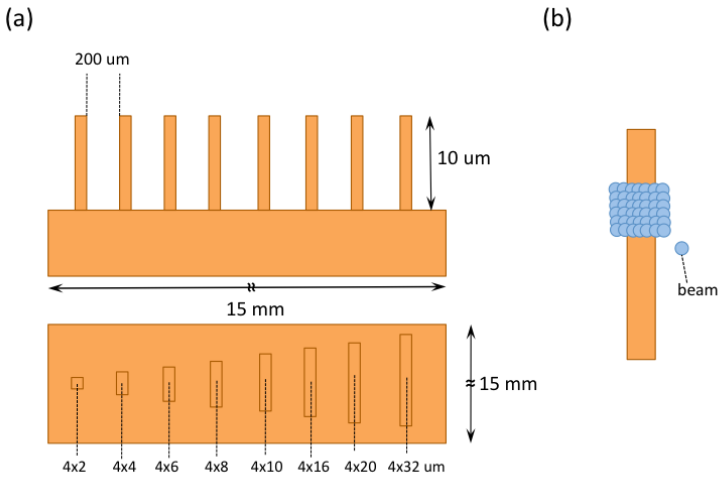

Figure 7.3: Lateral and top views of our samples. (a) We designed a set of Si pillars with same height (10 microns) and lateral profile (4 microns) but different thickness (from 2 up to 32 microns). The 15×15 mm dimensions refer to the size of the mask that we used to draw the pillars. On each sample we replicated the pillars series several times in order to have a backup from production defects or eventual damages during the experiment. (b) Here is an example of how to perform a ptychographic acquisition of a single pillar.

where $\mathbf{V_1} = 1\mathbf{x} + 1\mathbf{y} + 0\mathbf{z}$ and $\mathbf{V_2} = 1\mathbf{x} + 1\mathbf{y} + 1\mathbf{z}$ so that the resulting angle between the two directions was of 35.26 degrees. At this point it was necessary to determine the Bragg angle for the {111} reflection and in order to do so we needed to also take into account the energy that we were planning to use during our experiments. We estimated that the resulting {111} Bragg angle at the energy of 8.7 KeV was of around 13 degrees. By combining these two angles, we determined the inclination for our pillars which resulted in 12 degrees respect to the [110] normal direction.

The single sample consisted on a silicon support with a set of equally spaced Si pillars at the top, all with different thicknesses (from 2 up to 32 microns) but same width (4 microns) chosen to match the piezo scan range. The reason for including a series of differently sized pillars was to observe how the phase shift changed with the sample's thickness. Because the pillars were of much smaller dimensions respect to the size of the whole wafer, we cut the wafer into equally sized squares and replicated the design several times. Also, within the same piece of wafer, we replicated the series of pillars in order to have a backup in case of damages. The whole concept of our design is shown in Fig. 7.3. The resulting design can be described as a comb whose teeth are of same width but of different thicknesses. The idea

that we wanted to implement was to have a sample which, mounted perpendicular to the X-ray beam, would have allowed us to easily find the Bragg reflection and to change the position on the sample by moving from one pillar to another by simply shifting in one direction. The ptychographic acquisitions was to be performed on a single pillar at once, by illuminating its facet and collecting the resulting diffraction pattern in the far field.

A similar design was also used for the InP samples with the difference that in this case we used a 100 wafer with the idea of performing the experiment by collecting diffraction patterns from three distinct reflections coming from the (111), (220) and (222) planes. In this case we decided to incline the pillars by 17 degrees respect to the [100] direction, but bearing in mind that the execution of this experiment would have requested a change in the setup for each reflection.

7.2 Clean room production

The first step in preparing the sample was to cut the wafer into squares of equal sizes. The reason for doing so was to have a number of backup samples, mostly justified by the fact that the etching process that we wanted to use to cut our pillars is difficult to control. On one side we were not totally sure about how to set the etching time and having a number of spare samples would have allowed us to make few tries. What we wanted to achieve was to etch pillars 10 microns tall out of the substrate and the risk was of either etching too much, thus destroying the sample, or not enough having too short pillars. Having an height of around 10 microns was important for us because our idea was to perform ptychographic acquisitions close to the top of the pillars, staying far from the support so to avoid reflections that would have affected the diffraction patterns. Another reason for having more samples was that, even after setting the correct etching time, it usually happens that different samples put together inside the etching chamber will be etched in a different way because the flux of the etching gas is not perfectly homogeneous.

In order to produce our samples we used the clean room facilities available at the London Centre for Nanotechnology (LCN) which were easily accessible for us. The machine used to cut the wafer consisted in a vacuum chamber where the sample had to be mounted on a magnetic support. The magnets and the vacuum were used to secure the sample so to avoid movements that could have affected

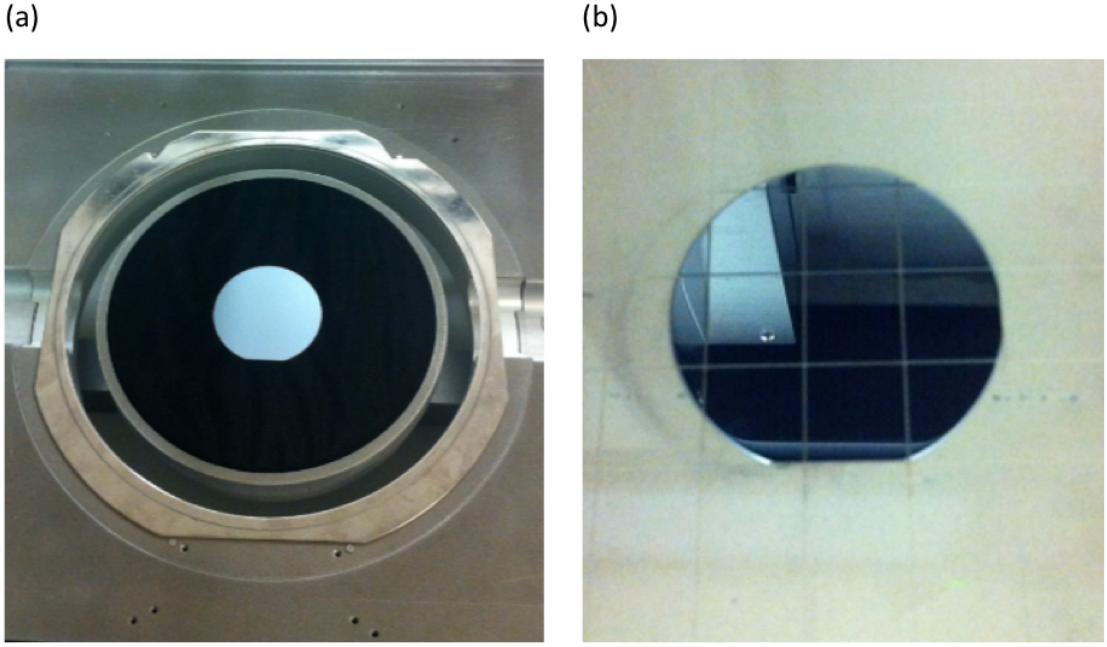

Figure 7.4: Starting point of the sample's preparation. (a) The 110 Si wafer is mounted on a support and inserted in a vacuum chamber where a compressed air saw will cut it into squares. (b) The resulting squares of 1×1 cm.

the precision of the cut. The whole system was software assisted so that we could easily decide the size of our squares, which in the end were of around 1×1 centimeters, as shown in Fig. 7.4.b. After cutting the wafer, another very important thing was to remember the orientation of the wafer for each square. As shown in Fig. 7.4, the orientation of the wafer was identified by a cut on one side of the wafer itself, so before disassembling the original wafer we marked each square to remember were the [110] direction was.

The following step in our production process was to prepare the squares for the electron-beam lithography, which would have allowed us to draw the masks that we wanted to use for our pillars. After removing the marked squares from the support we washed them with acetone and then we let them dry on a hot plate. At this point we were ready to put the e-beam resist on each square. In order to make sure that is was uniformly distributed on the samples' surface, we used a machine called spin coater, where the samples were processed once at a time. Spin coating is a commonly used practice to achieve high-precision lithography. It consists on rotating the sample so that the interaction

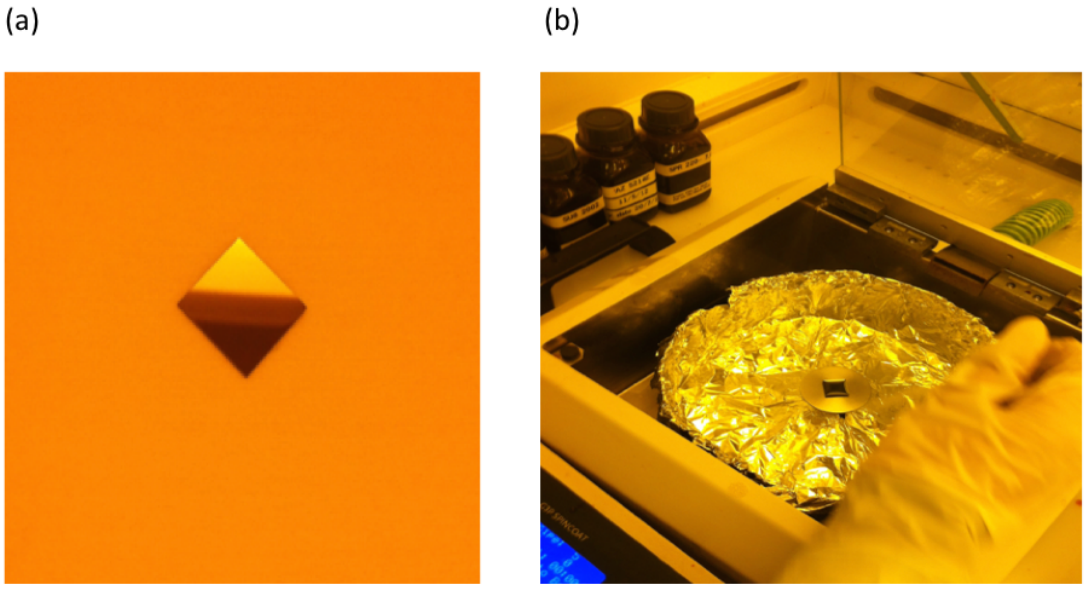

Figure 7.5: Photoresist deposition. (a) A single square obtained from the Si wafer. (b) E-beam resist deposition with the use of a spin coater.

between the viscous and centrifugal forces permit to obtain a uniform photoresist film of controllable and reproducible thickness. By using the spinner for the same amount of time for each square, we were sure to have the same photoresist coating on all samples.

After this stage we were finally ready to implement our design by using the e-beam lithography. This system operates by using a focused electrons beam which scans the sample and allows to draw custom shapes by interacting with the electron sensitive resist. Again, it is a software assisted procedure where the user interface allows to navigate the various samples mounted on the support in order to decide where, on each sample, to draw the masks pattern. In order to better visualize the pillars, we also decided to include a cross shaped mark of around 150 microns. Next to this cross we drew on a line the series of equally spaced pillars as shown in Fig. 7.3.a. After processing the samples with the e-beam we had to develop the resist with a solvent whose purpose was to keep the masks exposed to the electrons beam, while dissolving the rest of the coating. This step was done separately for each Si square by washing the pieces in the hot solvent at a temperature of around 80 degrees for approximately 40 seconds. After developing the samples we dried them out with a hot plate and then we checked on the optical microscope the presence of the masks. These steps are illustrated in Fig.

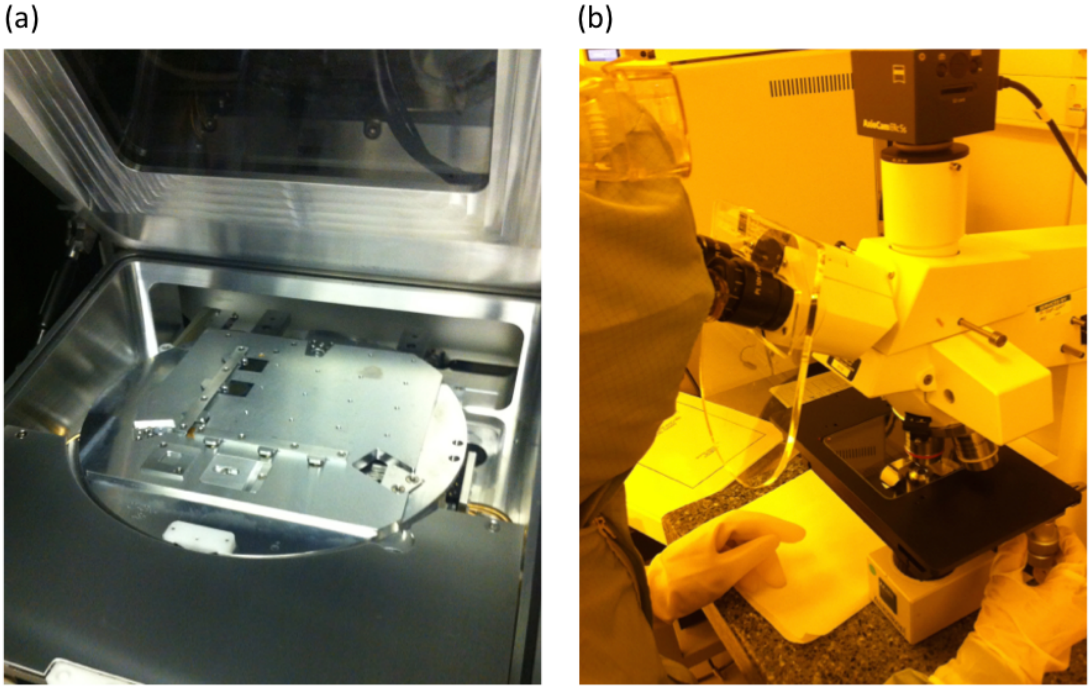

Figure 7.6: (a) Samples mounted in the e-beam system support. (b) After developing the processed photoresist, we checked the masks with an optical microscope.

7.6.

At this point we were finally ready for the last step: the plasma etching. In this part of the production process we used a machine which used a high speed flow of appropriate gas to attack the exposed silicon substrate in order to obtain our pillars. The masks impressed on the surface allowed to preserve the shape of our pillars but the choice of the appropriate etching recipe, to be used for the correct amount of etching time, was of primary importance. As illustrated in Fig. 7.7.a, the etching process itself is too aggressive and by only using it to process our samples we would have ended up with pyramid shaped pillars, this meaning that the masks would not have been able to endure for the whole etching period. Instead, in order to protect the masks and obtain the block-shaped pillars, we combined the deposition of C_4F_8 with SF_6 etching cycles.

In developing the InP samples we had to modify the etching recipe and this proved to be a not so easy step since we did not have any previous experience in etching this material. We chose to process the samples by having steps of O_2 deposition followed by CH_4 /H_2 etching cycles, also trying different

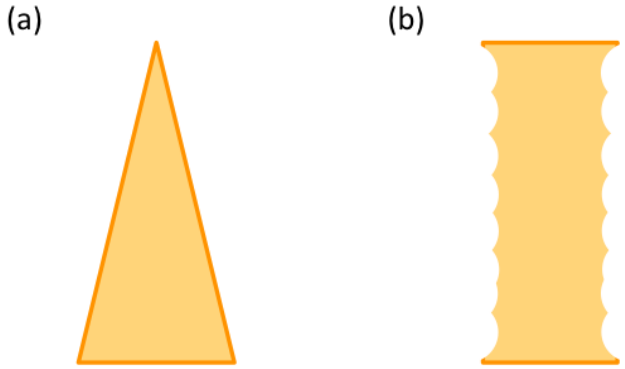

Figure 7.7: Etching process. (a) Etching itself is extremely aggressive so that the masks would not be able to persist. (b) If we combine deposition and etching, we can control the shape of the sample. Each etching cycle is visible on the pillar's edges and for our recipe of SF_6we estimated a 0.1-0.5 microns etch per cycle.

etching times, starting from 30 minutes up to 2 hours. The result gave us pillars 11 microns tall after etching for 30 minutes. As shown in Fig. 7.8.c the InP etching was more difficult and as a result we had a massive presence of debris all over the sample when the processing time was too long. We compared samples obtained at different etching times, from 30 minutes up to 2 hours and we could see that after 30 minutes we had debris covering the surface of our samples, while after 1 hour we started losing the shape of our structures.

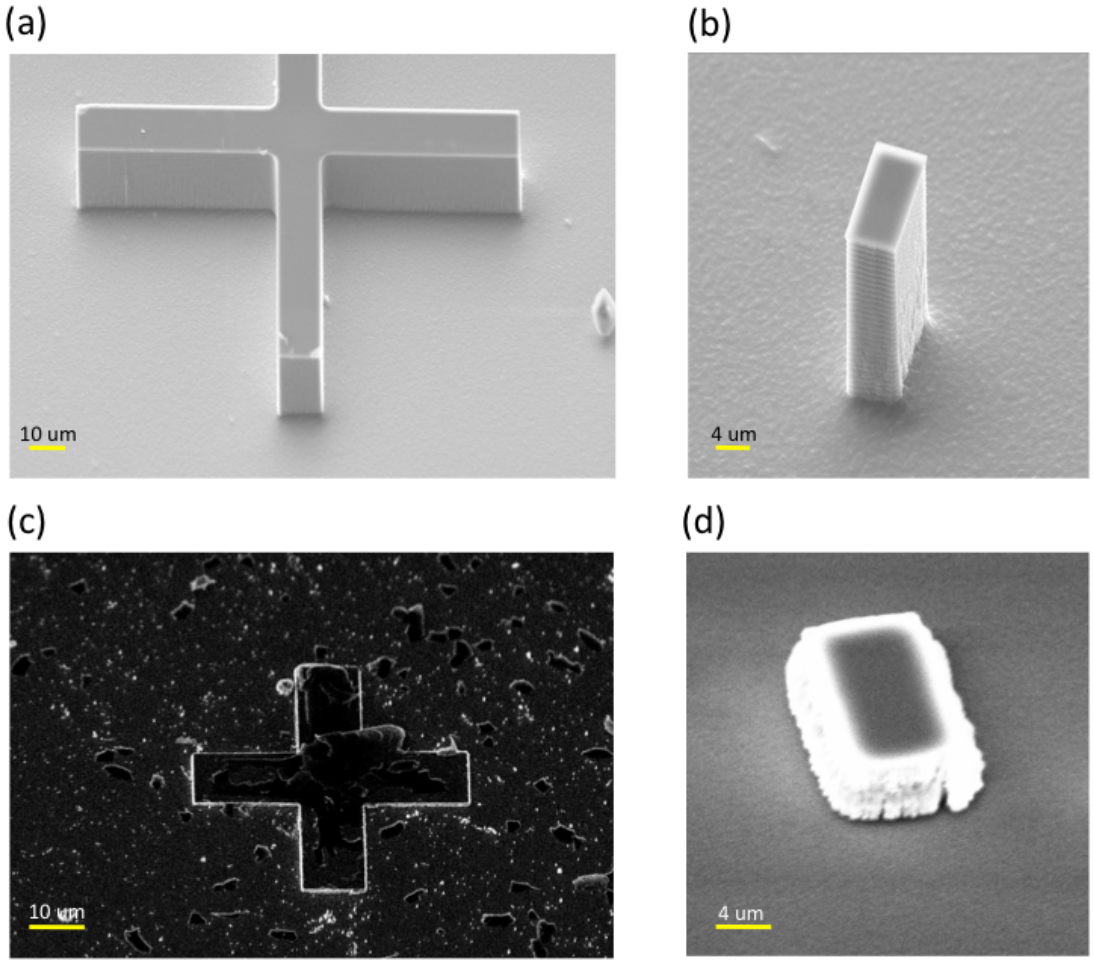

Figure 7.8: Etching results. a) and b) refer to the Si sample, while c) and d) show the result for the InP samples. c) For etching times longer than 30 minutes, the samples were full of debris. We saw that after one hour we completely lost the shape of our samples as a consequence of a too aggressive etching. d) InP pillar obtained after 30 minutes. By comparing it with b) we can see how the InP etching process was more difficult to control, as the shape of the pillar is less precise.

Chapter 8

Si and InP: experimental results

In order to test the robustness of the experimental technique described in the previous Chapters, we decided to perform similar measurements with the use of crystals characterized by more elaborated unit cell structures. For this reason, we designed new Si and InP samples as described in Chapter 7. However we decided that more meaningful results would have been obtained when measuring crystals of different thicknesses and for different crystallographic reflections. The outcome of these new measurements will be discussed in this Chapter where, to the contrary of what presented for the Au nanocrystals dataset, we will only adopt the fitting that we developed with the use of kinematical equations, in what we defined as an "approximate quasi-kinematical regime".

The experiments on the new samples were conducted at the 34ID-C beamline of the Advanced Photon Source (APS) facility at the Argonne National Labs in Illinois, USA. In order to adapt our experiment to a beamline different from the one used for gold nanocrystals, we had to change the setup. In particular we did not use Fresnel Zone Plates to focus our beam, but KB mirrors which are a more common setup for that beamline. At APS the white beam horizontal slit was located 27.5m away from the hutch, acting as a secondary source set to 150um to define the coherence as explained in [65]. Inside the experimental chamber we had the coherence-defining JJ slits whose aperture was adjusted several times during the experiments in accordance with the samples' thicknesses. Fig. 8.1 shows the part of the setup which controls the beam size. The focus size for a coherent beam is diffraction-limited by the JJ entrance slits width d as $f_{size} = \lambda D/d$ where D is the distance between the JJ slits and the focusing point. Further geometric considerations can be used to define the focal angle angle ψ, which

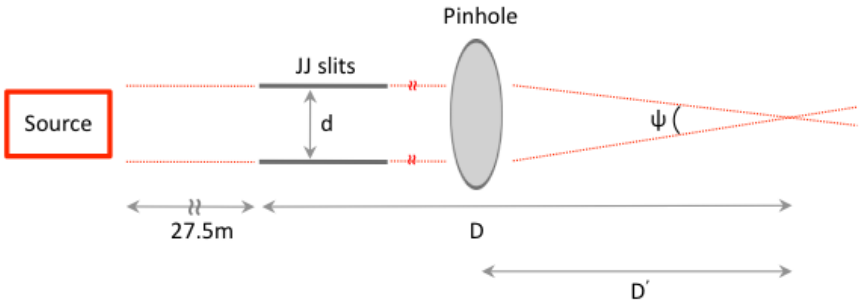

Figure 8.1: Experimental setup: lateral view of the setup that was used to control the beam size. The source was 27.5m away from the sample and the associated optics, where the longitudinal coherence was set through another set of slits of 150 microns aperture. The JJ slits were used to modify the aperture d, so that the angle ψ changed accordingly.

is obtained by combining the JJ slits aperture d and the distance D' between the pinhole and the focal point as $\psi = d/D'$.

The JJ slits size was used to control the rocking curve obtained when performing scans at different angles, in total similarity with what we did in our previous experiment. In this case, as it will be described in later sections, the rocking curves were measured using a scintillator detector which collected the beam reflected from the sample. In order to finely tune our setup, before performing the complete set of ptychographic scans we paid attention to the the rocking curve symmetry. In particular we adjusted the JJ slits size in the horizontal direction so that the angular spread of the rocking curve would have been bigger than ψ. It is worth noticing that, as shown below in Fig. 8.2, the width of the rocking curve is related to the sample's thickness, so for this reason we measured different curves for different samples.

8.1 Si samples

A complete schematic representation of the experimental setup which was used to perform the new set of measurements is shown in Fig. 8.3. In this case we used KB mirrors which were followed by a 40 microns pinhole positioned 2.8cm downstream. The sample was mounted on a 3D piezo stage,

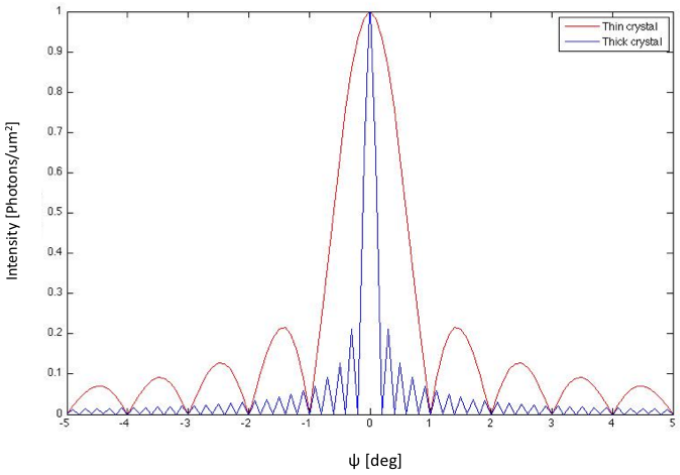

Figure 8.2: Rocking curves simulations. Theoretical rocking curves are represented for different sample's thicknesses. It is worth noticing that the intensity peak corresponds to the Bragg angle.

positioned 3.5cm away from the pinhole, where the silicon structures were attached flat to the support. In assembling the setup, we wanted to have the beam parallel to the sample's support, so that it could hit the pillars facets perpendicularly. We were able to perform our measurements in this geometric configuration and we obtained a resulting beam size of approximately 1 micron at the energy of 7.4 KeV. Behind the sample's stage we positioned a scintillator inclined by approximately 30 degrees in the horizontal plane, as represented in Fig. 8.3. This device was used in a similar way to the Pilatus 100K detector which was part of our setup during the gold nanocrystals experiment. In fact, in order to get the correct Bragg angle position we defined a range of angles and then rotated the sample accordingly. We then illuminated the sample moving at all angles and we measured the reflected beam intensity collected by the scintillator. The result of this acquisition showed the rocking curve, where the correct position of the Bragg angle corresponded to the highest intensity.

Downstream of the sample we used a 1.7m flight tube to reduce air scattering and then a 1x1mm^2 beam stop which partially blocked the direct beam that had not been diffracted by the sample, so to protect the detector from damages. The diffraction patterns were then collected using a Medipix detector with a single module of 256x256 pixels of 55 microns size.

Before using our Si samples, we performed several ptychographic acquisitions on a test pattern in order to retrieve the probe. Once obtained a good illumination function, we mounted the Si sample

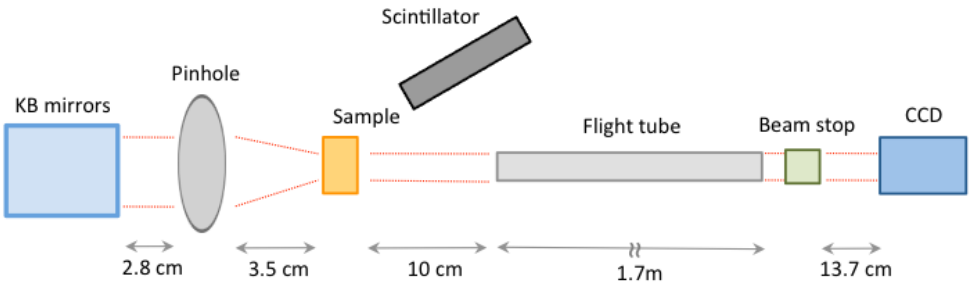

Figure 8.3: Top view schematic representation of the experimental setup. The scintillator was coplanar with the sample stage and was positioned at an angle of around 30 degrees. In order to attenuate the scintillator's photons counts, so to prevent damages, we used aluminum foils which we had to add or remove manually. In this schematic representation the beam direction is assumed from left to right.

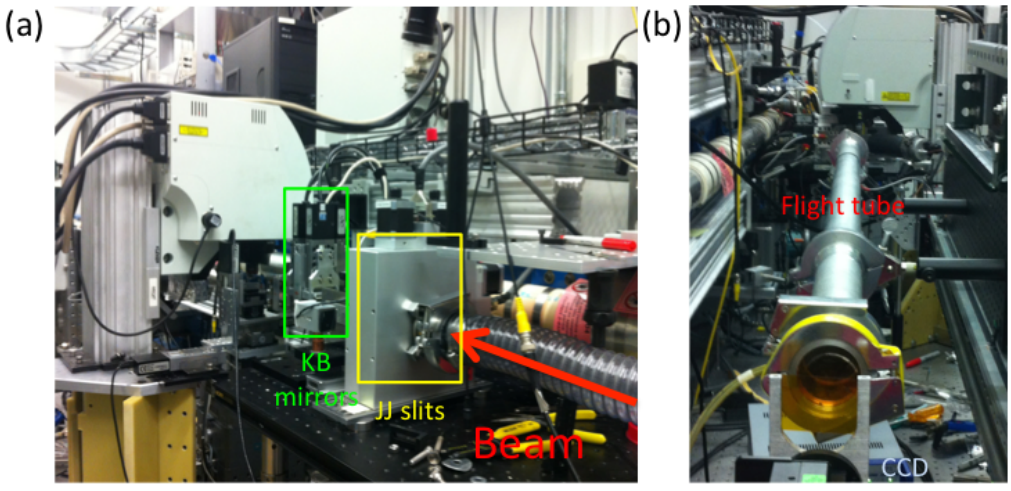

Figure 8.4: Photos from the beamline. (a) shows the portion of the setup upstream the sample while (b) is the downstream section.

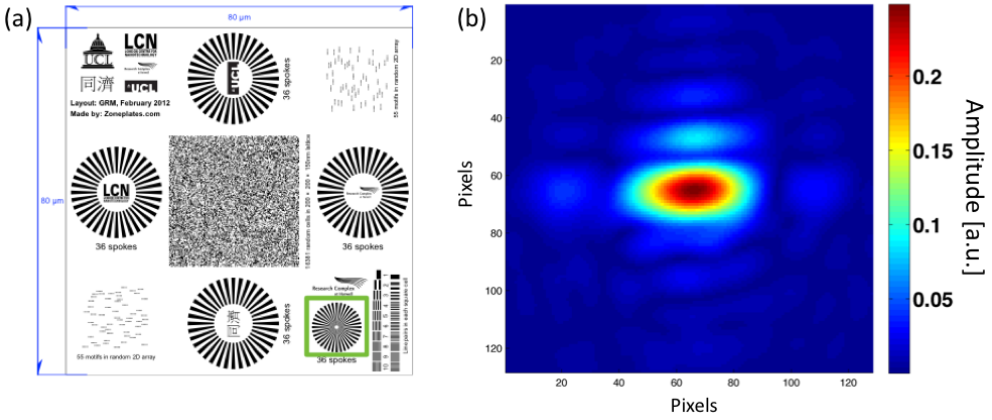

Figure 8.5: (a) Test sample layout, where the green square shows the 36 spokes siemens star that we used as test pattern. (b) Amplitude of the reconstructed probe obtained from the test pattern.

and performed a set of measurements. During the data analysis step, we used the probe retrieved with the test pattern as an initial probe guess for our reconstructions. It is worth noticing that the beam could not be considered stable during the whole beamtime. For this reason we had to move back to the test pattern and measure again the probe few times during the whole experiment. This step was necessary in order to use the correct probe for the reconstruction of data acquired at different times during the experiment.

By following the same approach used in Chapter 6, we could obtain a precise estimate of the beam size starting from the amplitude of the reconstructed probe. In particular we derived the linear profile of the probe's intensity and measure its FWHM which in this case corresponds to 50 pixels, as shown in Fig. 8.6. At this point, by applying the equation $pix_{sample} = (\lambda z)/(npix_{det})$ we observed that the pixels size at the sample's stage was of around 22nm[1]. By multiplying the pixel size by the FWHM we obtained a beam size of 1.1 micron, which is consistent with what expected in this configuration.

It is worth highlighting that the shape of the probe obtained in this configuration is different from what we showed in Chapter 6 for the gold nanocrystals experiment. In fact, in that case the probe was round shaped while in this case we had a square probe. The explanation for this difference can be given by observing that we used different focusing devices for the two experiments: the use of FZP implies a round probe, while the JJ slits-KB mirrors cascade results in a square one. Furthermore, we noticed that by adjusting the JJ slits aperture we could also modify the probe size, as shown in Fig.

[1]The values used in this formula are: n = 256 pixels, pix_{det} = 55microns, z = 1.93m and λ = 1.675Å.

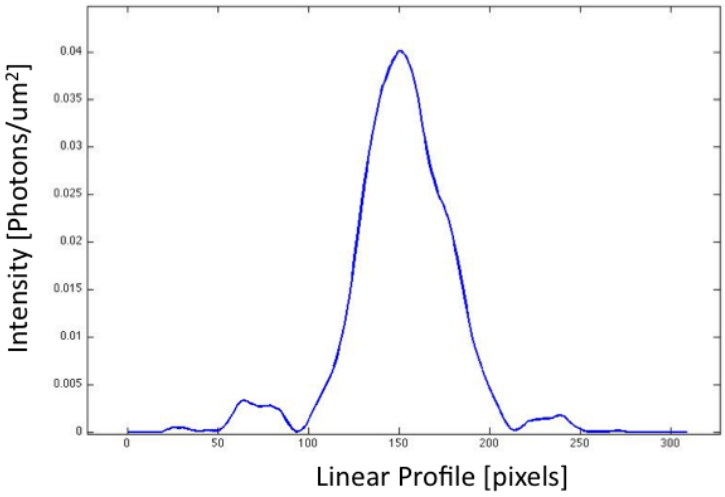

Figure 8.6: Probe intensity: linear profile.

8.7.

8.1.1 Si pillar: 4x4 microns

In this section we will discuss the experimental results obtained for the 4x4x10 microns^3 Si pillar. Later in the Chapter we will also discuss similar results obtained for the 4x8x10 microns^3 Si pillar. It is worth mentioning that both measurements were performed under the same condition, in particular for both acquisitions we set our JJ slits apertures to 10x60microns^2 (HxV).

In performing this experiment we wanted to improve our fitting results and for this reason we performed a larger set of scans on and off the Bragg angle. In complete analogy to what we did for the gold nanocrystals experiment, we made sure to center our scans around the Bragg angle which for this sample was the one correspondent to the {111} crystallographic reflection. By following Bragg's law, we calculated the theoretical Bragg angle for this configuration at the energy of 7.4 KeV, which resulted in 15.49 degrees. As discussed in the previous section, we used a scintillator in order to set the correct angular position of our acquisitions, which for this series corresponded to 7.987 degrees in lab coordinates, as it will be later shown in the fitting curves presented at the end of this section.

As previously discussed in Chapter 6, the reconstructed pillars were affected by phase ramps, as shown in Fig 8.8, and due to the large number of ptychographic scans that we performed for each

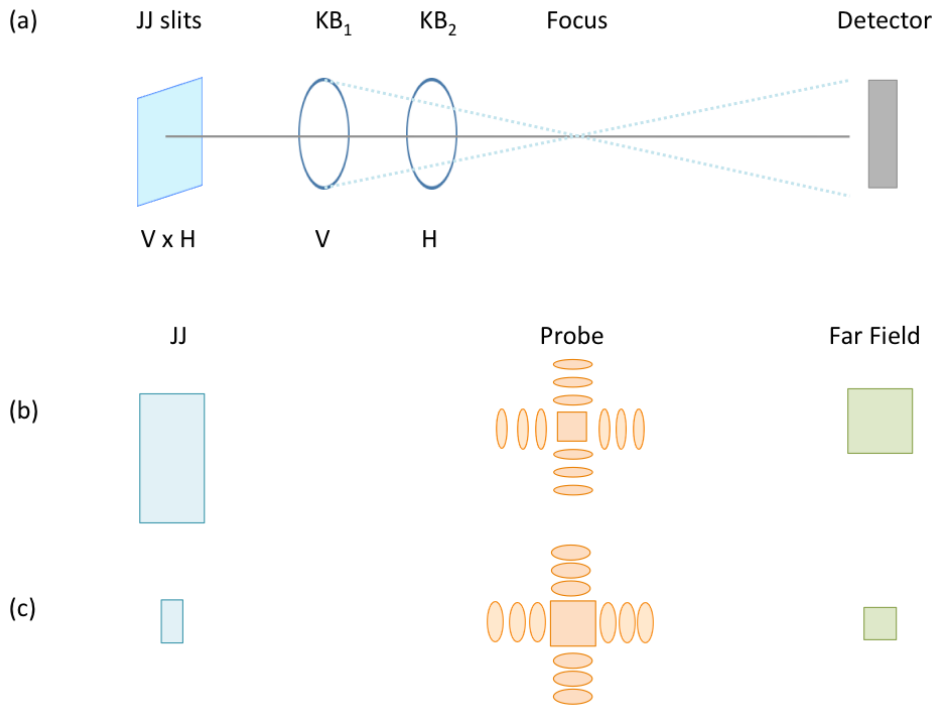

Figure 8.7: The JJ slits - KB mirrors cascade. (a) This schematic representation shows that the JJ slits aperture is set with a couple of values for the horizontal and vertical dimensions. Typical values are 30x60microns^2 (HxV) so to have a rectangular aperture. The KB mirrors cascade is represented with two lenses of different focal lengths, where the first lens KB_1defines the vertical dimension while KB_2 defines the horizontal one. The typical focal lengths are 220mm for KB_1 and 110mm for KB_2. This 2:1 ratio has the effect of modifying the shape of the probe which results squared. (b) Starting from a 30x60microns^2 (HxV) JJ slits aperture we obtain a square probe and then a square pattern in the far field. (c) Starting from a 20x10microns^{2}JJ slits aperture we have once again square probe and diffraction patterns in the far field, but the size will change respect to case (b) as shown in the scheme.

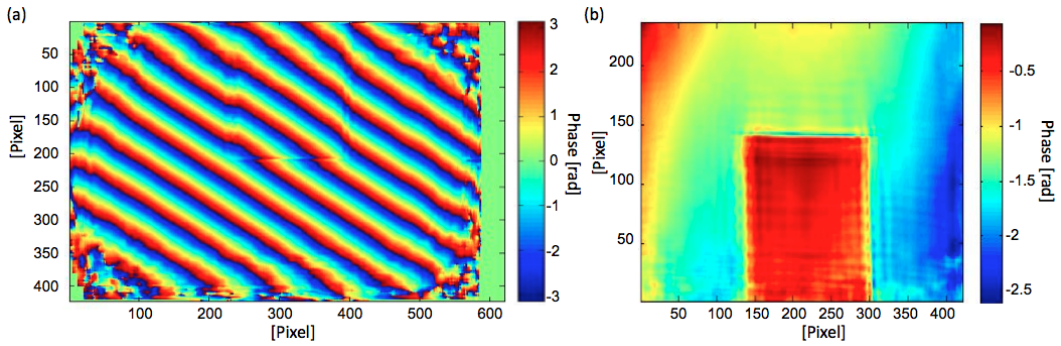

Figure 8.8: Phase of the reconstructed object showing (a) linear phase ramps and (b) after the phase ramp removal process.

series, we also had considerable drifts. As shown in figures 8.8.b and 8.9.a, even after a first phase ramp removal step, the reconstructions were still affected by a residual ramp. In order to correct it we had to align the reconstructions and then run a second step of phase ramp removal by drawing custom masks around each pillar, as already discussed in Chapter 6.

It is worth highlighting that we found the phase ramp removal process particularly difficult for pillar samples. In fact, on the contrary to the Au nanocrystals case, where we had the sample at the center of a large field of view which allowed to draw masks completely surrounding the object, here we could only use a portion of the space. In particular with only three masks, one at each side of the pillar, we found it difficult to completely remove the phase ramp. Once obtained the best phase profiles that we could get, here shown in Fig. 8.9.b, we followed the same steps described in Chapter 6 and extracted the phase shift values by defining blocks inside and outside the pillar where we calculated the average phases. In this case we only had 4 boxes so that, for each angle, we could estimate the phase as

$$phase_{av} = phase_{av,c} - \frac{phase_{av,1} + phase_{av,2} + phase_{av,3}}{3}, \tag{8.1}$$

where $\text{phase}_{\text{av,c}}$ is the phase calculated in the box inside the pillar. At this point we could also extract the error-bars by taking into account the standard deviations ε_i of the phases calculated in each box,

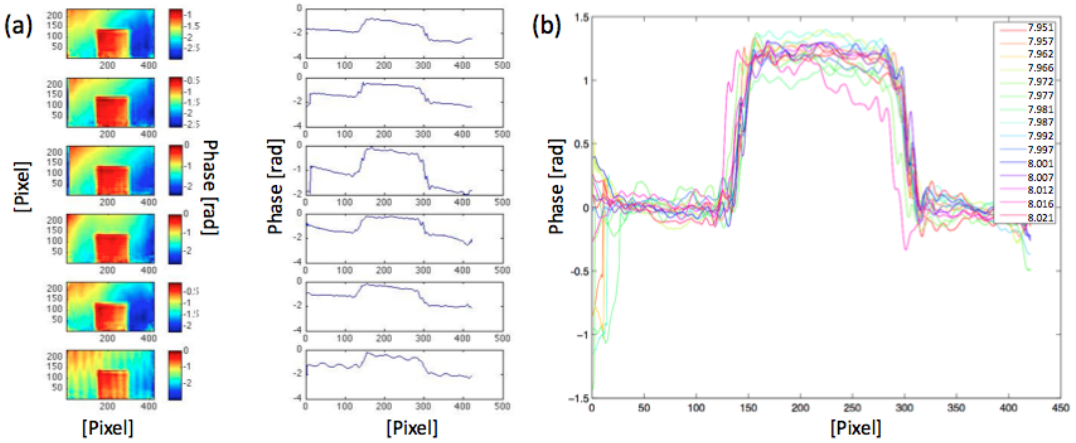

Figure 8.9: (a) Shows a set of phase reconstructions obtained for the Si pillar; each element of the series corresponds to a different illuminating angle. Here we also show the corresponding linear phase profiles. As one can notice despite showing an improvement respect to the phase shown in Fig. 8.8, the reconstructions here presented still present a residual phase ramp. For this reason, a second step of phase ramp removal was necessary in order to obtain the profiles shown in (b) which combines the linear phases of the entire set of 15 acquisitions (the legend shows the angular lab coordinates of each scan). It is worth noticing that the phase ramp removal procedure was much more complex respect to what we observed for the gold nanocrystals experiment. This can be explained by noticing that in this case we could only have phase removal masks drawn on three sides of the sample (left, right and top of the pillar) instead of using the whole space surrounding it. This, in our opinion, affected the overall quality of the data analysis.

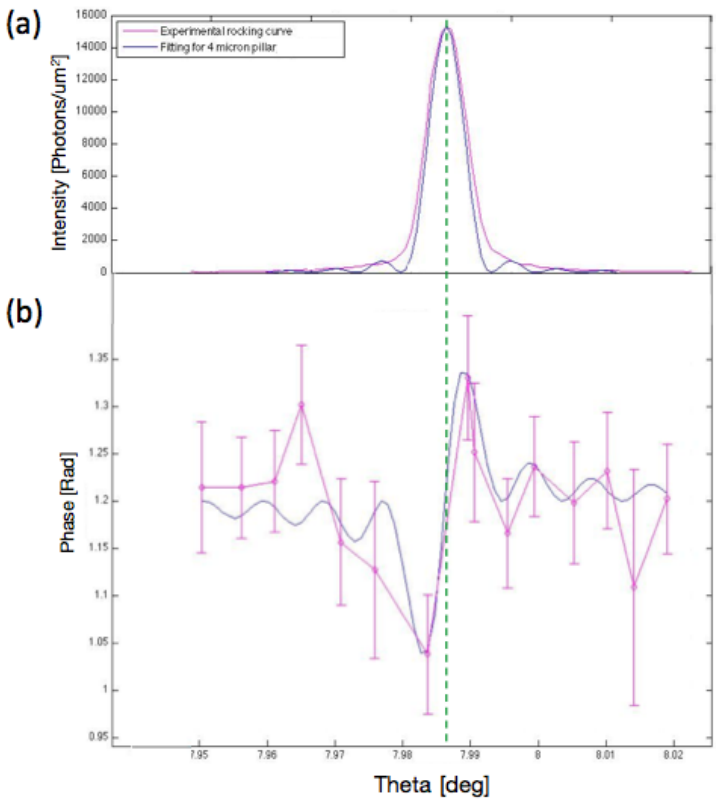

Figure 8.10: Fitting curves for the Si {111} sample with a thickness $d = 4\mu m$. (a) Rocking curve and (b) phase shift fittings obtained for $\alpha = -0.01e^{i\pi}$ and $N = 12.77 \cdot 10^3$, where the lattice parameter for Si is $a = 543.09pm$. The angles are presented in the lab coordinates, where $\theta_B = 7.987°$, here highlighted by the green dashed line. The error-bars are represented for each scan with an amplitude of $\pm\varepsilon_{tot}$; the largest errorbar shown here as an amplitude of $\pm\varepsilon_{tot} \simeq 0.25$ rad.

following the formula

$$\varepsilon_{tot} = \sqrt{\varepsilon_c^2 + \frac{1}{9}\varepsilon_1^2 + \frac{1}{9}\varepsilon_2^2 + \frac{1}{9}\varepsilon_3^2}. \tag{8.2}$$

The fitting curves were in the end calculated by only following the quasi-kinematical approach that we intuitively derived from the kinematical equations discussed in Chapters 2 ad 6. Relating to this, it is worth remembering that the thicknesses of all samples discussed in this Chapter were still well below the correspondent Pendellösung lengths[2]. The fitting result for the complete set of scans is shown in Fig. 8.10. The result shows a good fitting of the theoretical phase on the right side, while the initial scans on the left don't seem to follow the theoretical curve. As previously anticipated, the 6th scan in the series was affected by artifacts which could not be corrected, thus resulting in a large deviation from the theoretical curve. Overall, this measurement allowed to detect a total phase shift of approximately 0.3 rad.

It worth highlighting that the phase profile obtained for this sample presents a π phase shift if compared with the previous curves obtained for the Au nanocrystal experiment. For this reason we needed to use a complex fitting parameter

$$\alpha = \alpha_0 e^{i\phi} \tag{8.3}$$

where $\phi = \pi$. A simulation showing how the additional phase factor affects the phase shift profiles is shown in Fig. 8.11. We believe that this additional phase term was due to the geometry of the experimental setup, which was different respect to the one used for the Au nanocrystal experiment, as shown in Fig. 8.12. It is worth highlighting that the use of a complex fitting parameter requires a theoretical justification that the simplified approach used to fit our experimental data does not allow to define. During the data analysis conducted to retrieve the forward transmitted beam's phase profiles, the fitting parameter was tuned so to obtain curves which would come close to the profiles predicted by our approximate fitting theory. We acknowledge that at this stage we are not able to provide a detailed explanation for the nature of α, which certainly represents a limit to our approximate quasi-kinematical

[2]Here we neglected thermal and deformation factors and considered a factor $P = 1$, consistent with the σ polarization of the X-ray beam used at APS. It is worth noticing that these considerations will also apply to all the data fittings presented in this Chapter and that in doing so we used a simplified approach which did not take into account the intermediate polarization states corresponding to the measurements conducted when collecting data under different rotation geometries. In fact, when the scintillator position was moved out of the horizontal plane, as it will be later discussed for the InP {220} and {200} reflections, the resulting intermediate polarization state would have implied a correction to the polarization factor, whose complete determination would have required the development of a theoretical apparatus which is outside the scope of this Thesis work.

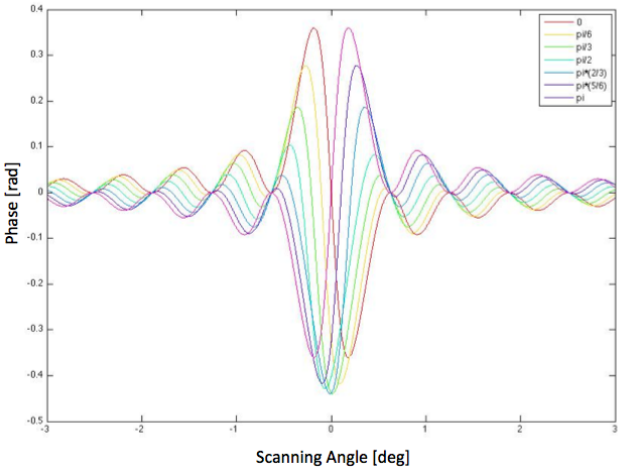

Figure 8.11: An additional phase component affects the transmitted wave's phase by shifting its profile in different ways. It is worth noticing that this effect is different in the Bragg's angle region where the zero-crossing point moves every time. On the other hand, off the Bragg condition the zero-crossings remain always the same.

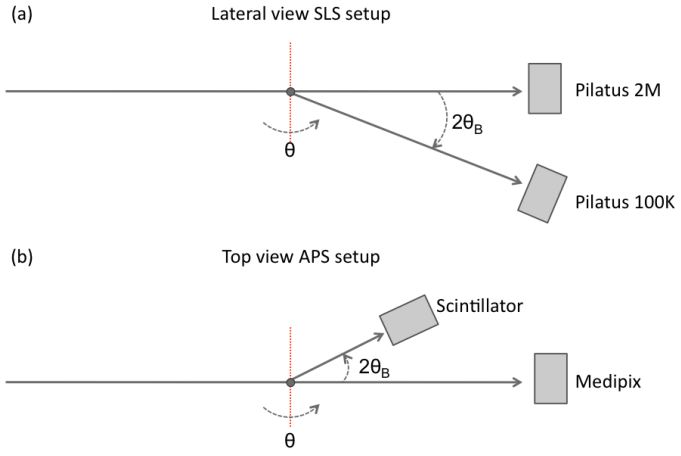

Figure 8.12: (a) Lateral view of the cSAXS setup. (b) Top view of the 34-IDC setup.

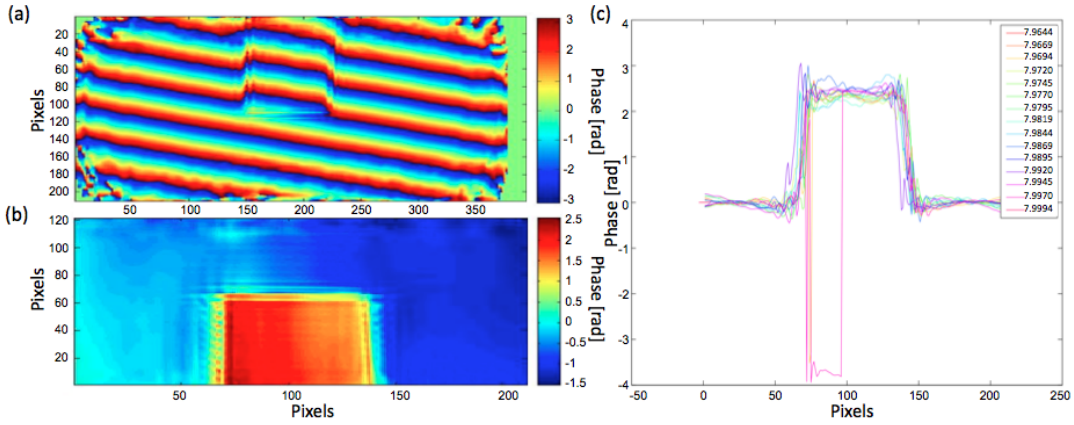

Figure 8.13: (a) Silicon pillar phase reconstruction before the phase ramp removal procedure and (b) after. (c) Phase linear profiles. The values in the legend are the angular lab coordinates of each scan.

fitting approach.

8.1.2 Si pillar 4x8 micron

Our experiment continued with a set of ptychographic scans performed on a nearby Si pillar of same width (4 microns) but a larger thickness of 8 microns. We did not change the setup because we were still interested in the {111} reflection and also the probe and the beam size were, with a good approximation, the same. In conducting the data analysis we followed the same steps as above with similar intermediate results. As one can notice from Fig. 8.13.c, few reconstructions could not be corrected as they presented phase jumps and still residual ramps. In order to work on the theoretical fittings, we had to remove the faulty reconstructions and concentrate on the best ones. In this way we obtained the final fittings using 10 scans instead of 15. The final fitted results for both rocking curve and phase shift are shown in Fig. 8.14.

In this case, while the rocking curve fitting is still a good approximation of the theoretical one, the experimental phase shift results seem to follow the theoretical phase shift only around the Bragg angle. Off the Bragg condition we still have a good fitting on the right side because the experimental results follow the theoretical curve, despite having values higher than expected, while the left side is still not as good. Overall, we were able to measure a total phase shift of 0.34 rad.

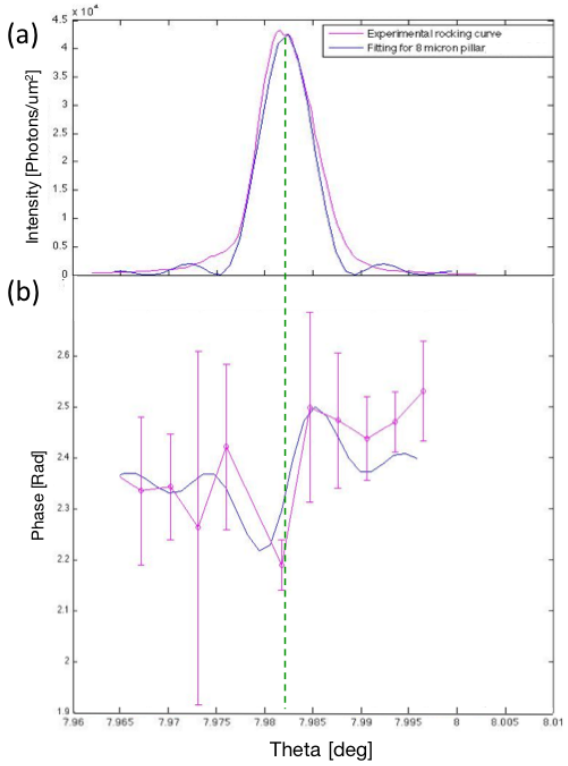

Figure 8.14: Fitting curves for the Si {111} sample with a thickness $d = 8\mu m$. (a) Rocking curve and (b) phase shift fittings obtained for $\alpha = -0.01e^{i\pi}$ and $N = 25.55 \cdot 10^3$, where the lattice parameter for Si is $a = 543.09pm$. The angles are presented in the lab coordinates, where $\theta_B = 7.9819°$, corresponding to the green dashed line. The error-bars are represented for each scan with an amplitude of $\pm\varepsilon_{tot}$; the biggest error bar had a size of $\pm\varepsilon_{tot} \simeq 0.69$ rad.

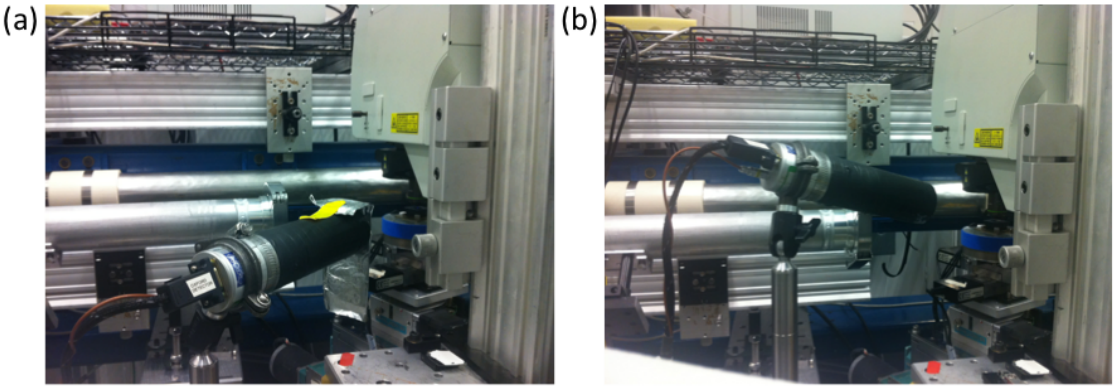

Figure 8.15: (a) Scintillator position for the {111} reflection. In this case we can see that the scintillator (black tube) lays on the sample's plane. (b) For the {200} reflection the scintillator is inclined respect to the sample's plane.

8.2 InP samples

We continued our investigation performing a similar experiment on InP pillars. As previously discussed in Chapter 7 the sample's layout is similar to the one used for the silicon wafer. We etched a 100 InP wafer and we modified the angular position of the pillars to 17 degrees with respect to the 100 normal. The main difference with the Si sample was that, while always having a set of different thicknesses for each pillar series, this time we also had 2 different lateral sizes: one of 4 microns and another of 6. In this section we will only present results for the 6 microns InP pillar of 4 microns thickness, but this time we will also refer to different Bragg reflections.

This experiment was once again performed at the 34ID-C beamline at APS, so for this reason the setup was the same that we used for the Si case, as shown in Fig. 8.3. The only difference with the previous setup was that we had to change the scintillator position in order to capture the different reflections, as shown in Fig. 8.15.

Before performing acquisitions on the InP sample we used again the test pattern in order to obtain an appropriate probe to use in our reconstructions. Because we also tried to used different JJ slits apertures, we performed acquisitions on the test pattern for each one of them. Once again we expected a beam size of around 1 micron but a more precise estimate could be obtained by analyzing the reconstructed probe, whose intensity is shown in Fig. 8.16.

For this experiments we used an energy of 9 KeV and by following the same procedure described in

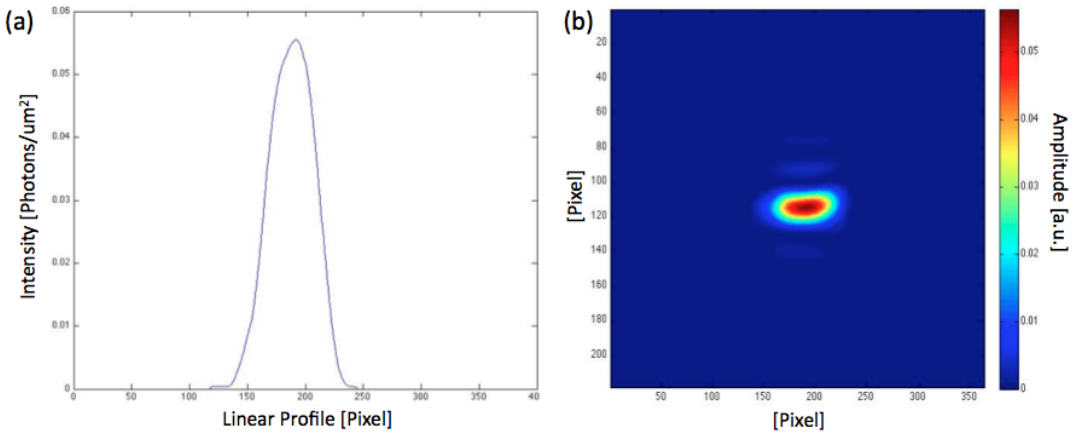

Figure 8.16: (a) Reconstructed probe's intensity linear profile and amplitude (b). The FWHM is of 50 pixels.

the previous section we measured a beam size of around 939 nm, which agreed with our expectations.

8.2.1 InP: {111} reflection

The first reflection that we wanted to analyze was the {111} because in that case the scintillator was laying on the sample's plane. The Bragg angle for this reflection was of around 11.66 degrees and the scintillator was placed at around twice this angle respect to the sample. In analogy with the previous set of measurements, we used the scintillator in order to derive the precise position of the Bragg reflection and to define a set of angles around it. For this new acquisition series, we set the JJ slits to 10x50 microns^2 (HxV). It is worth noticing that because our pillar was larger than the one analyzed in the Si case (6 microns versus 4 microns for the Si), we had to perform much longer scans. This affected our reconstructions because as the scans took much longer to perform, we had considerable drifts which we then needed to correct during the data analysis process. Fig. 8.17 presents the phase reconstructions before and after the phase ramp removal steps.

In order to be consistent with the data analysis and to be able to compare the results obtained for different angles, it was necessary to define the same region of interest for each scan. Because the sample drifted downwards during the set of scans, we concentrated the analysis on the edge of the pillar. In total analogy with what we did for the Si samples, we corrected the phase ramps and we

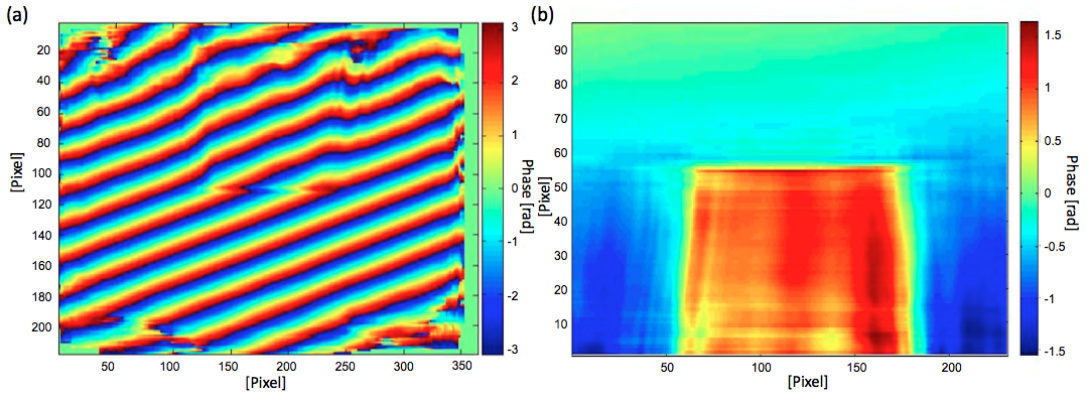

Figure 8.17: InP pillar reconstructions for the before (a) and after (b) the phase ramp removal.

aligned the reconstructions in order to correct all drifts. The complete set of 9 scans is shown in Fig. 8.18. A larger plot summarizing the linear phase profiles is presented in Fig. 8.19.

Contrary to what happened in the Si case, the phase profiles were not flat inside the crystal and also their width was different in few cases. This can be explained by the fact that the beam was fluctuating during the extremely long time of our acquisitions. We went on with the data analysis in total analogy with what we did for the Si case by drawing boxes of equal size, inside and outside the pillar, and by calculating the average phase and the error for each angle. The experimental results were then compared to the theoretical profiles obtained in the quasi-kinematical approximation defined in Chapter 6, as shown in Fig. 8.20.

The phase fitting shows very large errorbars which are consisting with the noise already showed in the linear phase profiles. However it is worth noticing that the phase shift profile is symmetric respect to the Bragg angle and that the experimental phase values are close to the theoretical curve around θ_B. Overall we were able to measure a total phase shift of 0.64 rad.

8.2.2 InP: {220} reflection

In order to perform acquisitions of the {220} reflection we had to slightly modify our experimental setup by changing the scintillator inclination with respect to the samples's horizontal plane. As shown in Fig. 8.21, the sample was designed in such a way that for the {111} reflection the beam (red arrow in the figure) only had to hit the pillar's surface perpendicularly.

In order to collect the {220} reflection, we had to change the ϑ angle from zero to the appropriate

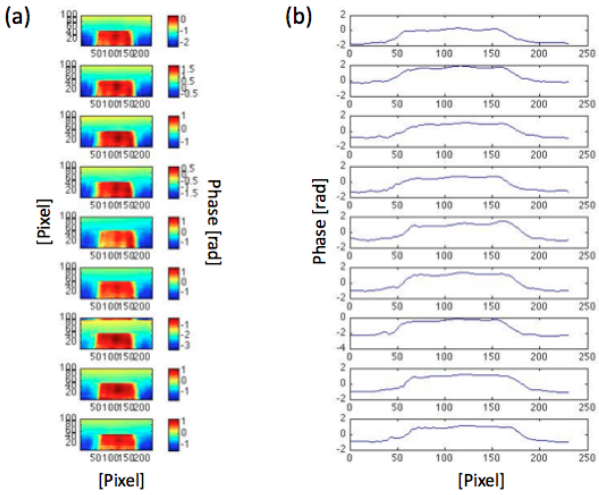

Figure 8.18: (a) Series of phase reconstructions, each one corresponding to different illuminating angles, after correcting for phase ramps and shifts. One can notice that the region of interest has been considerably reduced respect to the complete field of view shown in Figure 8.17. (b) Linear phase profiles extracted for each phase reconstruction.

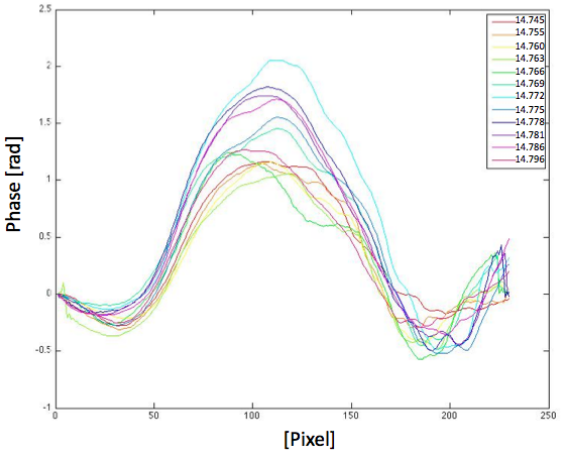

Figure 8.19: Phase profiles for different angles.

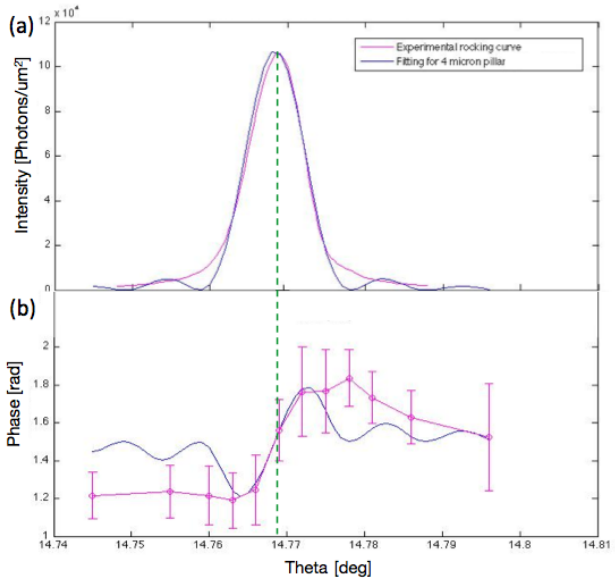

Figure 8.20: Fitting curves for the InP {111} sample with a thickness $d = 4\mu m$. (a) Rocking curve and (b) phase shift fittings obtained for $\alpha = -0.027e^{i\pi}$ and $N = 11.8 \cdot 10^3$, where the lattice parameter for InP is $a = 5.8687\mathring{A}$. The angles are presented in the lab coordinates, where $\theta_B = 14.769°$, here shown with the green dashed line. The error-bars are represented for each scan with an amplitude of $\pm\varepsilon_{tot}$; the biggest error bar has a size of $\pm\varepsilon_{tot} \simeq 0.56$ rad.

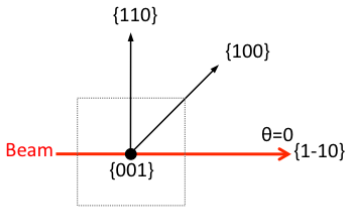

Figure 8.21: Top view of the sample layout. The pillars are designed in a way that the {111} reflection could be found by just hitting the pillar perpendicularly. For this reason, in this configuration, the scintillator lays on the sample's plane. When we wanted to collect other reflections we had to incline the scintillator at the appropriate ϑ angle. It is worth noticing that the [100] in plane direction is at 45 degrees.

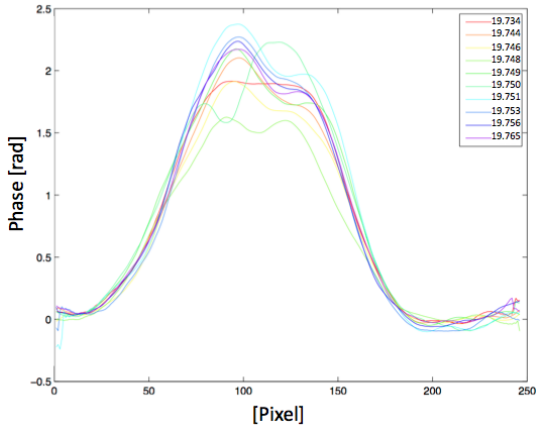

Figure 8.22: InP phase profiles for the {220} reflection. The values in the legend refer to the angular lab coordinates of each scan.

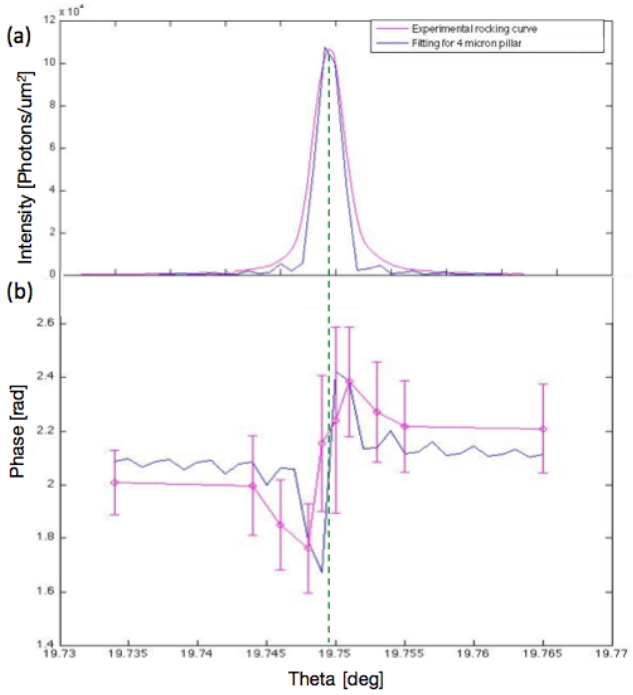

Figure 8.23: Fitting curves for the InP {220} sample with a thickness $d = 4\mu m$. (a) Rocking curve and (b) phase shift fittings obtained for $\alpha = -0.017e^{i\pi}$ and $N = 19.32 \cdot 10^3$, where the lattice parameter for InP is $a = 5.8687\mathring{A}$. The angles are presented in the lab coordinates, where $\theta_B = 19.749$ here shown on the green dashed line. The error-bars are represented for each scan with an amplitude of $\pm\varepsilon_{tot}$; the biggest error bar has a size of $\pm\varepsilon_{tot} \simeq 0.69$ rad.

angle. The way we found it, was to first set the scintillator at twice the {220} Bragg angle, which at the energy of 9KeV is 19.27 degrees. Then we also changed the ϑ angle to the correspondent Bragg angle as well. At this point we started tilting the sample's stage in both the χ and φ angular direction. At this point we launched theta scans and used the scintillator to record the reflected intensity so to obtain the correct position of the Bragg reflection in lab coordinates.

In performing this set of acquisitions we kept the JJ slits aperture to 10x50 microns^2 and launched a set of 10 scans around the Bragg angle. After performing the usual steps of phase ramp removal, alignment and average phase calculation, we were able to obtain better reconstructions and in fact the phase profiles, shown in Fig. 8.22, are less noisy.

It is worth highlighting that we can still see that the phase profiles are not flat inside the pillar. This is an important result because it demonstrates that what we found for the {111} reflection was not an artifact due to bad reconstructions but a real structure.

We went on conducting our data analysis by performing the quasi-kinematical fitting of our experimental results, as shown in Fig. 8.23.

Again the resulting rocking curve fitting was accurate, while the phase shift one was almost symmetrical with larger deviations from the theoretical curve happening off the Bragg, at both sides. Overall we were able to measure a total phase shift of c. 0.62 rad.

8.2.3 InP: {200} reflection

In performing this last set of acquisitions we modified the JJ slits aperture by opening the horizontal slits to 15 microns. Moreover, we also changed the scintillator inclination to $\theta = 45 + \theta_B$, where the Bragg angle is 13.49 degrees. After performing the set of procedures explained in the previous section, we found that the position of the Bragg peak.

We performed a set of 12 ptychographic scans around the Bragg angle and after correcting for phase ramps and lateral shifts of the sample, we obtained the linear phase profiles shown in Fig. 8.24.

In this case we can see that there is some noise that could not be corrected because in this case the reconstructions were not as good as before, maybe again due to the long scans and the implied difficulty in considering the beam stable for such a long time. However, despite a small phase ramp still persistent, we can still see that there is a phase structure inside the pillar and in particular it

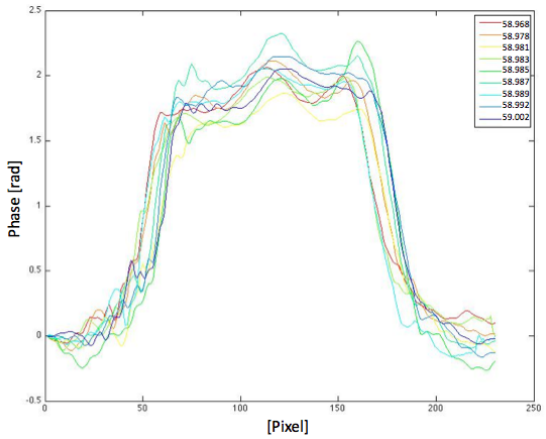

Figure 8.24: Linear phase profiles for the {200} reflection. The legend shows the complete set of angular positions.

looks like this structure is more evident around the Bragg condition and tends to fade off Bragg.

At this point we went on with our analysis by drawing once again our boxes inside and outside the pillar in order to retrieve the average phase and the errorbars measures for each angular scan. The result is presented in Fig. 8.25.

In this last case the phase shift profile fitting presents once again considerably big error bars, but the shape of the experimental curve is symmetrical and seems to mimic the shape of the theoretical one. Overall the total experimental phase shift that we measured was of about 0.29 rad.

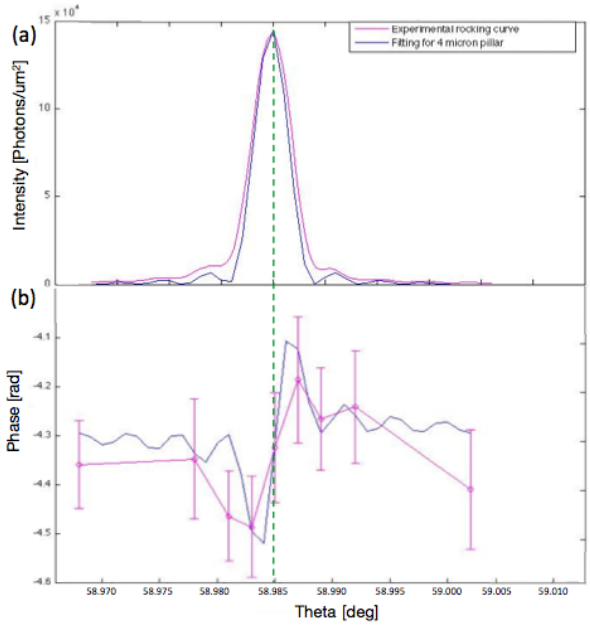

Figure 8.25: Fitting curves for the InP {200} sample with a thickness $d = 4\mu m$. (a) Rocking curve and (b) phase shift fittings obtained for $\alpha = -0.028$ and $N = 13.63 \cdot 10^3$, where the lattice parameter for InP is $a = 5.8687\mathring{A}$. The angles are presented in the lab coordinates, where $\theta_B = 58.985°$, corresponding to the dashed green line. The error-bars are represented for each scan with an amplitude of $\pm\varepsilon_{tot}$; the biggest error bar has a size of $\pm\varepsilon_{tot} \simeq 0.25$ rad.

Chapter 9

Conclusions

With the use of the Ptychographic imaging technique [13] we measured how the phase of an X-ray beam transmitted through a thin crystal changes when a diffracted beam is generated inside the sample for different rocking angles. A first experiment conducted on Au nanocrystals allowed to observe a phase change which was found to agree with both a quasi-kinematical approximate model and the fully dynamical theory of diffraction, evaluated numerically for the specific sample thickness, as discussed in Chapter 6. Given the rather elementary unit cell structure of gold crystals, we decided to test the robustness of our experimental technique by performing a second experiment on more complex crystalline structures. In particular we wanted to see if the outcome of our measurements would have been negatively affected by an increasing number of atoms within the unit cell and by the presence of different elements. For this reason we designed and produced new Si and InP samples, by following the steps described in Chapter 7. In order to perform a second series of experiments we re-designed our experimental setup, in order to adapt it to a different synchrotron facility[1], by also using different geometries which allowed to measure Bragg diffraction from different crystallographic planes. As a result we were able to measure the phase shift of the transmitted beam as a function of the rocking angle in full analogy with what we achieved for the Au experiment. A table summarizing the measured phase shift amplitudes, together with the relative errors is presented in Tab. 9.1. This summary allows to see that in all cases we were able to measure the phase shift of the forward diffracted beam and, by referring to the profiles discussed in Chapters 6 and 8, we can also note that bigger errors were

[1]The Au nanocrystal experiment was conducted at the cSAXS beamline at the SLS facility, while the Si and InP measurements were performed at the 34ID-C beamline at the APS synchrotron.

Sample	Thickness	Reflection	Δϕ [rad]	ε_{max} [rad]	ε_{min} [rad]	Average ε [rad]	Av ε/Δϕ
Au	100 nm	{111}	0.0290	0.0140	0.0032	0.0055	18.97%
Si	4 μm	{111}	0.2983	0.1270	0.0539	0.0694	23.27%
	8 μm	{111}	0.3422	0.3477	0.0490	0.1311	38.31%
InP	4 μm	{111}	0.6479	0.2823	0.1251	0.1740	26.86%
		{220}	0.6219	0.3482	0.1216	0.1974	67.17%
		{200}	0.2939	0.1257	0.0876	0.1075	17.29%

Table 9.1: Here we present a summary of the phase shift values measured during our experiments. $\Delta\Phi$ is the maximum amplitude of the phase shift, while $\varepsilon_{max.min}$ represent the maximum and minimum sizes of the error bars calculated for each phase point. Furthermore here we also show the average error-bar value obtained across the entire set of angular positions defining the rocking scan for each phase shift profile. By comparing this value with $\Delta\Phi$ we can have a measure of the errors in the measured phases.

commonly associated to scans at angular positions well off the Bragg condition. An explanation for this effect can be given by considering that the lower intensity of the scattered beam off the Bragg angle implies a lower signal-to-noise (SNR) ratio which does not allow to correctly retrieve the phase.

A different aspect of the work illustrated in this Thesis is relative to the fitting of the experimental curves. As already discussed, thanks to the collaboration with Vartanyants, Shabalin and Gorobtsov [23], we were able to show a rigorous fitting obtained with the use of dynamical diffraction [38, 2], as discussed in Chapter 4. However, we also proposed an approximate fitting based on quasi-kinematical considerations, which proved to substantially agree with the more accurate dynamical theoretical apparatus. Encouraged by this result, we decided to apply this same fitting to the other experiments conducted on Si and InP, as discussed in Chapter 8. In order to establish the accuracy of our fitting methodology, we decided to add an additional phase contribute ψ defined as

$$T(\mathbf{q}) = 1 + \alpha R(\mathbf{q})\, e^{i\psi} \tag{9.1}$$

as shown in Fig. 9.1. This empirical method allowed to determine that the fittings could be considered correct within a phase interval of $\psi = 0 \pm 0.4$ rad[2].

In conclusion, through this Thesis work we could demonstrate the high accuracy of the phase that can be measured using the ptychography approach. We believe that this quality arises directly from

[2]Similar results were obtained for the InP {220} and {200} reflections.

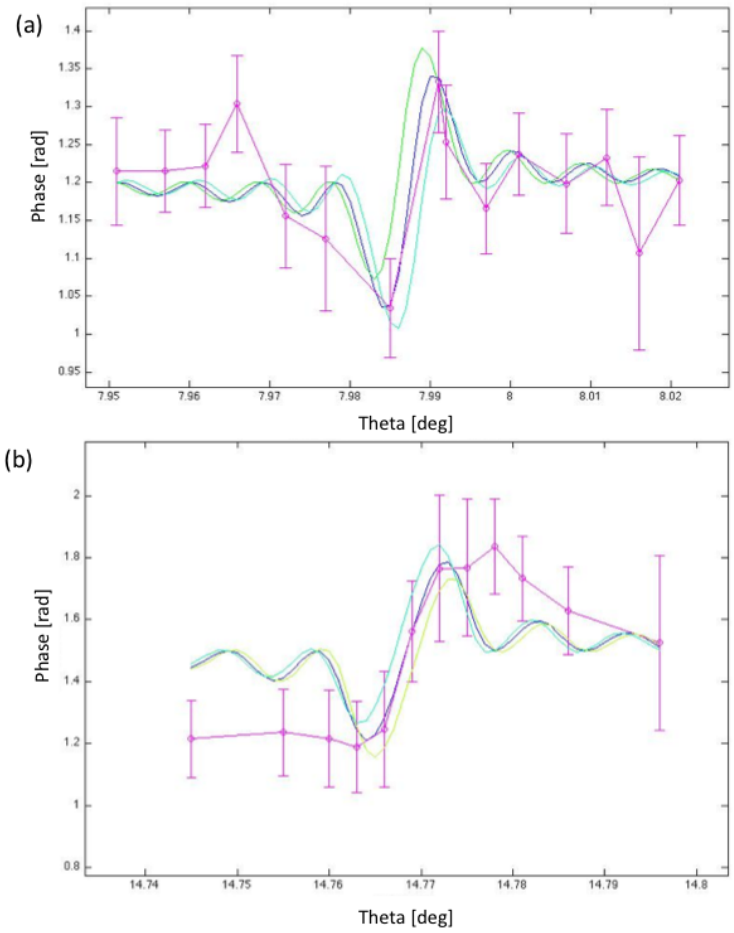

Figure 9.1: Si (a) and InP (b) phase shift fittings for the {111} reflection. The green lines refers to additional phase contributes of ±0.4 rad.

the high coherence of the X-ray beam used. In fact, the beam traversing the crystal is coherently mixed with the beam that passes around it, resulting in a deviation of the diffracted beam. The pattern of these deviations is reconstructed as a phase image self-consistent for all positions of the sample probed by scanning and the resulting phase is very accurate.

We believe that this experimental technique can find numerous applications if supported by an accurate theoretical apparatus. To this purpose, in this Thesis we dedicated a section to discuss a recently formulated *quasi-kinematical* approximation, developed by Gorobtsov and Vartanyants [2]. This theory allows to relate the phase shift of the forward diffracted beam to the phase of the unit cell structure factor, so we can expect that the use of our experimental method, supported by the *quasi-kinematical* equations would allow to directly solve the phase problem. In fact, as also discussed in Chapter 6, the successful dynamical fitting performed on our experimental curves would also be consistent with the results obtained in the *quasi-kinematical* regime. For this reason we believe that our experimental technique is already accurate enough to provide meaningful results. Going forward, the potential for this experimental and theoretical combination would allow to finely investigate the structure of strained crystals, as well as to detect the structure factor of complex and multi component materials.

Acknowledgements

The completion of this research project would have not been possible without the contribution of many people who supported me during these past few years.

The first person that I would like to thank is my supervisor, Prof. Ian Robinson, who has always believed in this project and whose passion for the research activity has inspired me throughout all these years. His understanding and patience have helped me many times and his humanity and generosity gave me an example that I will try to follow for the rest of my life.

The revision of this Thesis would have not been possible without the help and support of Prof. Gerd Materlik who guided me towards the fascinating world of dynamical diffraction. I will always treasure his advices and have a good memory of the time we spent together.

I would also like to thank Dr. Graeme Morrison, who has always been there for me with good advices and smart suggestions. I really had the best time with him and Dr. Malcolm Howells at the TwinMic beamline, where we went several times to perform experiments on structured illumination.

My deepest gratitude goes to Dr. Ana Diaz, beamline scientist at the cSAXS beamline at the Swiss Light Source synchrotron, whose dedication was extremely important in achieving our first experimental results.

I would also like to thank Dr. Ross Harder, beamline scientist at the APS 34-IDC beamline, for his support during the many experiments that we conducted with him.

Last but not least, I would like to thank my family. My husband Guido who has always been there for me with his love and support, giving me the strength to overcome the many difficulties that I encountered during these years. My mother Luigia who has always put her needs aside so that I could pursue my dreams. Grazie mamma per essere la persona piú forte del mondo!

List of Figures

List of Tables

Bibliography

[1] J. Nielsen and D. McMorrow. *Elements of Modern X-ray Physics*. Wiley, 2000.

[2] O. Y. Gorobtsov and I. A. Vartanyants. Phase of transmitted wave in dynamical theory and quasi-kinematical approximation. *Phys. Rev. B*, 93:184107–1–11, 2016.

[3] N. Kato and A. R. Lang. A study of pendellosung fringes in x-ray diffraction. *Acta Crystallographica*, 12:787, 1959.

[4] M. Hart and A. D. Milne. An accurate absolute scattering factor for silicon. *Acta Crystallographica*, A 25:134–137, 1969.

[5] M. J. Bedzyk and G. Materlik. Two-beam dynamical diffraction solution of the phase problem: a determination with x-ray sanding-wave fields. *Phys. Rev. B*, 32-10:6456–6463, 1985.

[6] K. Hirano and A. Momose. Investigation of the phase shift in x-ray forward diffraction using an x-ray interferometer. *Phys. Rev. Lett.*, 76-20:3735–3737, 1996.

[7] E. Wolf. Solution of the phase problem in the theory of structure determination of crystals from x-ray diffraction experiments. *PRL*, 103:075501–3, 2009.

[8] E. Wolf. Determination of phase of diffracted x-ray beams in investigations of structure cystals. *Physics Letters A*, 374:491–495, 2010.

[9] P. D. Nellist and J. M. Rodenburg. Electron ptychography. i. experimental demonstration beyond the conventional resolution limits. *Acta Crystallographica*, 54:49–60, 1998.

[10] T. Plamann and J. M. Rodenburg. Electron ptychography. ii. theory of three-dimensional propagation effects. *Acta Crystallographica*, 54(1):61–73, 1998.

[11] J. M. Rodenburg, A. C. Hurst, A. G. Cullis, B. R. Dobson, F. Pfeiffer, O. Bunk, C David, K. Jefimovs, and I. Johnson. Hard-x-ray lensless imaging of extended objects. *Phys. Rev. Lett.*, 98:034801, 2007.

[12] A. M. Maiden and J. M. Rodenburg. An improved ptychographical phase retrieval algorithm for diffractive imaging. *Ultramicroscopy*, 109(10):1256–1262, 2009.

[13] J. M. Rodenburg. Ptychography and related diffractive imaging methods. *Advances in Imaging and Electron Physics*, 150:87–184, 2008.

[14] P. Thibault and A. Menzel. Reconstructing state mixtures from diffraction measurements. *Nature*, 494:68–71, 2013.

[15] W. Friedrich, P. Knipping, and M. Laue. Interferenz-erscheinungen bei rontgenstrahlen. *Sitzungsberichte der Kgl. Bayer. Akad. der Wiss*, pages 303–322, 1912.

[16] H. A. Hauptman. The phase problem of x-ray crystallography. *Rep. Prog. Phys.*, pages 1427–1454, 1991.

[17] H. Hauptman and J. Karle. The probability distribution of the magnitude of a structure factor. *Acta Crystallographica*, 6:136–141, 1953.

[18] G. Bricogne. Maximum-entropy and the foundations of direct methods. *Acta Crystallographica*, A 40:410–445, 1984.

[19] A.L. Patterson. A fourier series method for the determination of the components of interatomic distances in crystals. *Pys. Rev.*, 46:372–376, 1934.

[20] E. Wolf. *Introduction to the theory of Coherence and Polarization of Light*. Cambridge University Press, 2007.

[21] L. Mandel and E. Wolf. *Optical coherence and Quantum Optics*. Cambridge University Press, 1995.

[22] E Lima, A. Diaz, M. Guizar-Sicairos, S. Gorelick, P. Pernot, T. Schleier, and A. Menzel. Cryo-scanning x-ray diffraction microscopy of frozen-hydrated yeast. *Journal of Microscopy*, 249:1–7, 2013.

[23] M. Civita, A. Diaz, R. Bean, O. Shabalin, O. Y. Gorobtsov, I. A. Vartanyants, and I. K. Robinson. unpublished.

[24] D. H. Templeton. X-ray dispersion effects in crystal-structure determinations. *Acta Crystallographica*, 8:842, 1955.

[25] D. Ewald. *Ann. Phys. Lpz.*, 54:519, 1917.

[26] B. W. Batterman and H. Cole. Dynamical diffraction of x-rays by perfect crystals. *Reviews of Modern Physics*, 36-3:681–717, 1964.

[27] A. Authier. *Dynamical theory of X-ray diffraction*. Oxford science publications, 2001.

[28] S. Stepanov. X-ray server: an online resource for simulations of x-ray diffraction and scattering. *Proceedings SPIE*, 5536:16–26, 2004.

[29] S. Takagi. *J. Phy*, 26:1239, 1969.

[30] D. Taupin. *Acta Crystallographica*, 23:25, 1967.

[31] H. Hattori, H. Kuriyama, T. Katagawa, and N. Kato. *J. P*, 20:988, 1965.

[32] H. Hattori and N. Kato. *J. Phys. Soc. Japan*, 21:1772, 1966.

[33] N. Kato and S. Tanemura. *Phys. Rev. Let.*, 19:22, 1967.

[34] K. Yamamoto and N. Kato. *Acta Crystallographica*, A 24:230, 1968.

[35] B.W. Batterman and J.R. Patel. *J. Applied Physics*, 39:1882, 1968.

[36] N. Kato. *Proc. Jap. Acad. Soc.*, 25:41, 1949.

[37] B. W. Batterman. *Phys. Rev.*, 133:A759, 1964.

[38] I. A. Vartanyants and M. V. Kovalchuk. Theory and applications of x-ray standing waves in real crystals. *Rep. Prog. Phys.*, 64:1009–1084, 2001.

[39] I. K. Robinson and R. Harder. Coherent x-ray diffraction imaging of strain at the nanoscale. *Nature Materials*, 8(4):291–8, 2009.

[40] R. Hegerl and W. Hoppe. *Ber. Bunsenges. Phys. Chem.*, 74:1148–1154, 1970.

[41] J. Miao, P. Charalambous, J. Kirz, and D. Sayre. Extending the methodology of x-ray crystallography to allow imaging of micrometre-sized non-crystalline specimens. *Nature*, 400:342–344, 1999.

[42] A. Schropp, P. Boye, A. Goldschmidt, S. Honig, R. Hoppe, J. Patommel, C. Rakete, D. Samberg, S. Stephan, S. Schoder, M. Burghammer, and C. G. Schroer. Non-destructive and quantitative imaging of a nano-structured microchip by ptychographic hard x-ray scanning microscopy. *Journal of Microscopy*, 241:9–12, 2010.

[43] K. Giewekemeyer, P. Thibault, S. Kalbfleisch, A. Beerlink, Kewish C. M., M. Dierolf, and F. Pfeiffer. Quantitative biological imaging by ptychographic x-ray diffraction microscopy. *Proceedings of the National Academy of Sciences of the United States of America*, 107:529–534, 2009.

[44] M. Dierolf, A. Menzel, P. Thibault, P. Schneider, Kewish C. M., R. Wepf, O. Bunk, and F. Pfeiffer. Ptychographic x-ray computed tomography at the nanoscale. *Nature*, 467:436–439, 2010.

[45] M. Dierolf, P. Thibault, A. Menzel, and F. Pfeiffer. Ptychographic coherent diffractive imaging of weakly scattering specimens. *New Journal of Physics*, 12(3):035017, 2010.

[46] J. M. Rodenburg, A. C. Hurst, and A. G. Cullis. Transmission microscopy without lenses for objects of unlimited size. *Ultramicroscopy*, 107:227–231, 2007.

[47] F. Hue, J. M. Rodenburg, A. M. Maiden, F. Sweeney, and P. A. Midgley. Wave-front phase retrieval in transmission electron microscopy via ptychography. *Phys. Rev. B*, 82:121415, 2010.

[48] J. M. Rodenburg and H. M. L. Faulkner. A phase retrieval algorithm for shifting illumination. *Appl. Phys. Lett.*, 85:4795, 2004.

[49] J. R. Fineup. Phase retrieval algorithms: a comparison. *Applied Optics*, 21(15):2758–2769, 1982.

[50] V. Elser. Phase retrieval by iterated projections. *Journal of the Physical Society of America*, 20(1):40–55, 2003.

[51] P. Thibault, M. Dierolf, A. Menzel, O. Bunk, C David, and F. Pfeiffer. High-resolution scanning x-ray diffraction microscopy. *Science*, 321(5887):379–382, 2008.

[52] P. Thibault, M. Dierolf, O. Bunk, A. Menzel, and F. Pfeiffer. Probe retrieval in ptychographic coherent diffractive imaging. *Ultramicroscopy*, 109(4):338–343, 2009.

[53] R. Bean. *Domain structure imaging with Bragg geometry X-ray Ptychography.* PhD thesis, London Centre for Nanotechnology, University College London, 2012.

[54] R. M. Goldstein, H. A. Zebker, and C. L. Werner. Satellite radar interferometry: Two-dimensional phase unwrapping. *Radio*, 23(4):713–720, 1988.

[55] N. Soni. Phase unwrapping algorithm using edge detection and statistical cost functions. Master's thesis, Delft University of Technology, 2012.

[56] J. W. Goodman. *Introduction to Fourier Optics, 3rd edition.* Robert and Company Publishers, 2005.

[57] N. Burdet, G. R. Morrison, X. Huang, X. Shi, J. N. Clark, F. Zhang, M. Civita, R. Harder, and I. K. Robinson. Observations of artefacts in the x-ray ptychography method. *Optics Express*, 22(9):10294–10303, 2014.

[58] F. Berenguer, R. Bean, L. Bozec, J. Vila-Comamala, F. Zhang, Kewish C. M., O. Bunk, J. M. Rodenburg, and I. K. Robinson. Coherent x-ray imaging of collagen fibril distributions within intact tendons. *Biophysical Journal*, 106(2):459–466, 2014.

[59] M. Guizar-Sicairos, A. Diaz, M. Holler, M. S. Lucas, A. Menzel, R. Wepf, and O. Bunk. Phase tomography from x-ray coherent diffractive imaging projections. *Optics Express*, 19(12):21345–21357, 2011.

[60] A. Parson. *Coherent Diffraction Imaging using a High Harmonic Source at 40 eV.* PhD thesis, University of Southampton, 2014.

[61] M. Guizar-Sicairos, S. T. Thurman, and J. R. Fineup. Efficient subpixel image registration algorithms. *Opt. Lett.*, 33:156–158, 2008.

[62] Mathworks website. www.mathworks.co.uk.

[63] Gullikson E.M. Davis J.C. Henke, B.L. Atomic data and nuclear data tables. 54:181–342, 1993.

[64] A. Afanasev and V. Kohn. *Acta Crystallographica Sect. A*, 27:421, 1971.

[65] I. K. Robinson. Optimisation of coherent x-ray diffraction imaging at ultrabright synchrotron sources. *Z. Kristallogr. Suppl.*, 27:27–35, 2008.